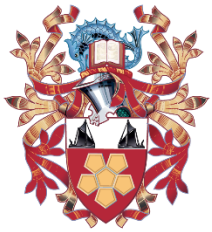

MULTI-ANTENNA FIXED POSITION SYSTEM FOR LESION DETECTION WITHIN PHANTOMS

ALISTAIR IAIN PICKERING

This report is submitted in partial fulfilment of the requirements of London South Bank University for the degree of Master of Research in General Engineering

September 2022

London South Bank University
EST 1892

School of Engineering

MRes Project in General Engineering

TITLE: Multi-antenna fixed position system for lesion detection within phantoms

Author: Alistair Pickering
Student Number: 3527705
Academic Session: 2020-2022

Supervisor: Professor Sandra Dudley-McEvoy
Course Title: MRes General Engineering
Mode of Study: Part-Time

This report has been submitted for assessment towards a Master of Research in General Engineering in the Department of Engineering and Design, London South Bank University. I declare that the text contained in this report unless it has been properly cited is the original work of the author and has not been previously submitted.

Date: 30/09/2022
Author's name: Alistair Iain Pickering
Author's signature:

ACKNOWLEDGEMENTS

This project would not have been possible without the incredible support from my supervisors, family, friends and work colleagues. My most sincere thanks go to the two fantastic supervisors, Professor Sandra Dudley-McEvoy and Dr. Gianluigi Tiberi, for their patient support, and for teaching me more than I expected.

I would also like to give thanks to my parents, brother and fiancé, who have given me endless mental and emotional support and encouragement.

TABLE OF CONTENTS

TABLE OF FIGURES

TABLE OF TABLES

Abstract

This project advances the current capability of using Ultra High Frequency (UHF) antennas to detect dielectric differences within a phantom, as a prerequisite for bone fracture analysis. The following research was conducted to investigate whether the scatter parameter measurements from multiple fixed position antennas could successfully reconstruct images of a phantom with a lesion.

An Ultra-WideBand (UWB) Antipodal Vivaldi Antenna (AVA) was designed to transmit frequencies between 1800MHz and 2500MHz with an end fire beam between $\phi = \pm 4°$ (confirming the main beam is directed towards the phantom). Simulations and measurements were performed using four antennas, eight antennas and sixteens antennas spaced equally within the system. For each system, three contrasting phantom scenarios were taken, a homogenous phantom, a phantom with the lesion placed at 0°, and then with the lesion placed at 90°. The reconstructed images were analysed, comparing the three tests, and showed that using a sixteen-element system, the lesion position but not size was clearly detectable.

These findings confirm that a fixed position system can be used as an alternative to the current process, which then drastically reduces testing times.

TABLE OF ABBREVIATIONS

Table 1-1 – Table of abbreviations

Abbreviation	Definition
µW	Micro-Watt
3D	3-Dimensional
ABS	Acrylonitrile Butadiene Styrene
AC	Alternating Current
AVA	Antipodal Vivaldi Antenna
BALUN	Balanced-Unbalanced
BAVA	Balanced AVA
CT	Computed Tomography
CVA	Coplanar Vivaldi Antenna
dB	deciBel
EMF	ElectroMagnetic Field
FR4	Flame Retardant-4
FSPL	Free Space Path Loss
GHz	Giga Hertz
H	Hertz
HF	High Frequency
LSBU	London South Bank University
MHz	MegaHertz
MRI	Magnetic Resonance Imaging
mW	Milli-Watt
nW	Nano-Watt
PCB	Printed Circuit Boards
RAM	Radiation Absorbent Mat
RF	Radio Frequency
SHF	Super High Frequency
SMA	Sub Miniature type A
THz	TeraHertz
UHF	Ultra-High Frequency
US	UltraSound
UWB	Ultra-wideband
VHF	Very High Frequency
VNA	Vector Network Analyser
VSWR	Voltage Standing Wave Ratio
W	Watt

CHAPTER 1. INTRODUCTION

In recent years, there has been an increasing interest in the development of medical imaging techniques utilising Radio Frequency (RF) signals. Several studies have established that a wide range of frequencies within the RF spectrum, ranging from Ultra High Frequency (UHF) at 30MHz to 3GHz [1], up to Super High Frequency (SHF) at 3GHz to 30GHz [2]. This type of medical imaging technique paves the way for a non-ionising, non-invasive and low-cost solution to produce cross-sectional internal images of patients. Recent studies have utilised this technology by developing solutions for breast lesion detection [3]–[5], bone fracture detection [1], [6], [7] and bone density [8] measurements, utilising this technology. All of the studies relating to RF medical imaging research used either a single or dual antenna system that mechanically rotated around the Phantom.

1.1. PROBLEM STATEMENT AND OBJECTIVES

After researching into the current capabilities of RF medical imaging, the following question was proposed. Will increasing the number of antennas, while remaining in fixed positions, provide adequate measurements and increase speed to identify the presence of an inclusion within a phantom? To achieve an answer to this, seven clear objectives were set out.

- Understand CST by simulating existing antenna designs
- Design and characterise an antenna that meets the frequency and performance requirements
- Perform simulations on various system sizes using four phantom configurations
- Observe the impact on antenna performance with respect to inclusion placement
- Assemble and measure the performance of an antenna to compare with the simulated characteristics

- Perform measurements on various system sizes and phantom configurations
- Perform reconstruction imaging on the simulated and measured results to determine if the setup can detect if a lesion was present

There were a number of known limitations with the project, which impacted what was capable of being achieved. With limited experience, a large portion of the project focussed on understanding and developing the single antenna performance. Due to funding limitations, an electronic RF switch was unavailable and resulted in manual switching between antennas.

1.2. **METHODOLOGY OF WORK**

The project was split into four sections, research, simulation, measurement and reconstruction. Each of these required an understanding of the appropriate methodology. The quantitative data from a number of studies were analysed with respect to their resolution of inclusion detection. Repeatable antenna and system simulations were then developed with singular variable changes between cases, in order to determine their impact. A robust experiment using identical system set-ups to simulations were constructed, which can be verified using further phantom configurations. The common variable within the reconstruction software was standardised for each system size, with only the input simulation and measurement files being variable. This ensured a robust experiment from research to completion.

1.3. **OVERVIEW OF WORK CONDUCTED**

The purpose of this study was to investigate whether a multi-port, fixed position, time switched system was a suitable alternative to a common two-port rotating system. The systems researched within this report have used either single or dual elements rotating around the object under test to generate enough measurements for image reconstruction of internal injuries. This was currently seen

as very time-consuming with the equipment mechanically moving around the phantom to allow for further measurements, which prompted the investigation of using fixed position antennas.

Initial designs were performed in simulation using CST Microwave Studios 2019 to calculate reflection, insertion loss and beam pattern for a single port antenna, two-port rotational system and a fixed position system. Equivalent positions and measurements were performed between the dual-port and fixed position systems to determine if the interaction between multiple antennas degraded the overall performance of the system.

A practical investigation was then performed by machining several antennas from double-sided copper, Flame Retardant-4 (FR4) sheets. Identical testing to the simulation was performed using a two-port Vector Network Analyser (VNA) within an anechoic chamber to measure reflection loss and beam patterns of a single port antenna. Three system sizes of four, eight and sixteen ports were tested surrounding a phantom without an inclusion to be used as a reference point. Further testing was performed on a phantom with an inclusion set closest to position-1 and then repeated with the phantom rotated 90° to position-5 and provide a clear differential.

The complex reflection loss, $S_{x\text{-}x}$, and insertion loss, $S_{x\text{-}y,}$ results from each test was recorded, where *x* denotes the primary antenna and *y* denotes the secondary antenna position. Previously written MATLAB code was adapted for use on this project to produce cross-sectional images of the phantom on each test, to determine the optimum quantity for the indication that inclusion was present [9].

CHAPTER 2. LITERATURE REVIEW

The following chapter investigates earlier relevant studies of medical imaging techniques and summarises their effectiveness. This was split into common techniques i.e. X-Rays, Computed Tomography (CT), Ultrasound (US), Magnetic Resonance Imaging (MRI) and Radio Frequency

(RF) systems. The research then focuses on the recent studies using RF signals within the UHF and SHF bands, which have been shown to produce adequate cross-sectional images for a range of applications. Various antenna designs used within these studies were investigated to determine general system requirements relating to a frequency band, gain, beam direction and size.

2.1. CURRENT COMMON MEDICAL IMAGING TECHNOLOGIES

Medical imaging is the process of generating internal images of the patient for clinical analysis without the need for surgical intervention [10]. This project aimed to provide additional research on the antenna systems used in bone fracture analysis performed at the Bioengineering research Centre at LSBU. Many medical imaging techniques have been discounted as they provide poor performance for bone fracture analysis, such as thermal imaging and medical photography.

Radiography systems produce uniform beams within the X-Ray band at approximately 3,000,000 THz ($3x10^{18}$ Hz) to permeate through the body, being attenuated to varying degrees by different biological materials such as fat, bone, and muscle. The resulting beam is then received by an X-Ray sensitive detector to be generated into a two-dimensional projection image [11]. This technique was then developed into CT scanners, where the X-Ray transmitter, and multiple receivers, rotate around the patient to produce cross-sectional images of the body [12]. Both of these techniques produce an excellent spatial resolution, caused by the extremely high frequencies used, which allow for hairline fracture detection. Ionising radiation is a risk with these techniques and has shown to been cause mutations within cell genes and lead to cancerous growths [13].

MRI systems have been developed as an alternative to CT scanners to produce high-resolution patient images without the use of ionizing radiation [14]. The system generates a high-powered magnetic field around the area of interest to polarise all protons. A radio wave within the High Frequency (HF), 3MHz to 30MHz, and Very High Frequency (VHF), 30MHz to 300MHz band then deflects

the magnetic axis of specific atoms so that when the waves are removed, they produce an EMF wave correlating to the material density [15]. Super-resolution algorithms have been developed to increase the spatial resolution of CT scanners, allowing for improved imaging techniques and clinical diagnosis [14]. MRI systems are capable of detecting fractures within bones as the bone contains few hydrogen protons, resulting in a dark image, while the blood within the fracture is shown as bright [16]. There are no known hazards from the use of MRI itself, however, due to the intense magnetic field, any metallic objects within or around the patient pose a physical risk [15]. The systems are also incredibly costly, require special housing, are time-consuming, require significant staff training and may cause stress to the patient due to being in an enclosed noisy environment for an extended period [17], [18].

UltraSound (US) scanners have been produced to typically transmit between 2MHz and 18MHz with the higher end being utilised for detecting smaller details [19]. Based on the frequency range used, it is difficult to produce a high spatial resolution using a US system as the wavelength, even at 18MHz is approximately 16m in air. This causes the system to rely heavily on signal processing techniques to construct a more usable image. Ultrasound techniques are typically used for soft tissue imaging such as muscle and organs, as the frequencies used are unable to penetrate denser materials such as bone [19]. Duck's work has analysed possible risks with the use of ultrasound imaging, focussing on heating, acoustic cavitation, gas-body effects, and radiation pressure. It was concluded that many of these provide either low or very low risk to the user, confirming it is generally a safe form of imaging [20]. A further drawback with US imaging is that it requires coupling jelly and physical contact with the user for the wave to effectively couple with the area of interest. This in turn poses a potential risk to the user as physical contact with a fractured bone may cause discomfort.

Recent studies have shown that RF systems, transmitting within the UHF, 300MHz to 3GHz, and SHF bands, 3GHz to 30GHz, combined with various image reconstruction techniques can successfully detect lesions within biological materials [1], [21], [7], [2]. The designs can either utilise reflection loss, S_{1-1}, in a monostatic system or insertion loss, S_{2-1}, in a bistatic system where a separate receive antenna measures the transmitted signal. The transmitted signal interacts with the object under test to varying degrees based on its material composition, which in turn has an impact on S_{1-1} and S_{2-1} measurements [22]. The antenna is then moved to a new position, with the object under test remaining stationary, and the measurement is performed again. The resulting measurements are then collected into a matrix, from which a cross-sectional image can be reconstructed. Due to the relatively low-frequency range used, when compared to X-Rays, the system produces non-ionising radiation which reduces the risk to the patient. Recent studies have also shown that an effective system can be produced using two antennas and a Vector Network Analyser (VNA), which substantially reduces the space requirement compared to MRI. The drawback seen with this approach is the reduced spatial resolution of the images that are reconstructed, based on the frequency range.

In summary, medical imaging technologies have been used for many years for clinical study and diagnosis. Each approach has its advantages and disadvantages, as listed in Table 2-1, as well as its specific use cases.

Table 2-1 – Summary of medical imaging techniques

Criteria	**X-Ray**	**CT**	**MRI**	**US**	**RF**
Ionising radiation	Yes	Yes	No	No	No
Bone imaging	Yes	Yes	Yes	No	Yes
System cost	High	High	High	Moderate	Low
System size	Large	Large	Large	Small	Small
Power consumption	High	High	High	Low	Low
Speed of measurement	Fast	Slow	Slow	Fast	Fast
Contact with patient	No	No	No	Yes	No

2.2. CURRENT RF IMAGING SYSTEMS AND RESULTS

2.2.1. Breast Lesion Detection Using RF Imaging

Substantial research has been conducted on the detection of breast lesions, using UHF radio signals. Each material of soft tissue based on whether it is fat, water or protein has unique dielectric properties concerning an RF signal. This gives an increase or decrease of impedance, distorting the signal wave as it passes through the barrier in an $S_{2\text{-}1}$ system or coupling to the transmit antenna in an $S_{1\text{-}1}$ system.

Jafari et al. designed a UWB rectangular patch antenna, with a coplanar waveguide and a curved feed edge to maximise the potential bandwidth. This resulted in a system functioning between 3.4GHz and 9.9GHz, with all frequencies under -10dB for $S_{1\text{-}1}$ [5]. The purpose of having an upper limit of -10dB reflection loss is to keep the Voltage Standing Wave Ratio (VSWR) below 2:1, which is considered an acceptable response for an antenna [23]. Two identical antennas were produced and placed on opposing sides of a phantom container, filled with pork fat to simulate human tissue. This research has confirmed that the design can successfully couple energy into the human body when placed close to the interface.

Hailu and Safavi-Naeini successfully designed a UWB antenna for breast cancer detection, functioning between 4.6GHz and 10.6GHz with a very narrow beamwidth of 10.3° [24]. The antenna was designed to work within a coupling medium to effectively transmit a beam.

Tiberi et al., researched the different dielectric properties of human tissues at various frequencies, allowing for the development of a phantom containing a comparable material [25]. Tiberi et al., utilised a discone antenna between the frequency ranges of 3.5GHz and 8.0GHz to perform these tests and produce a highly stable frequency response. A recent development in breast cancer detection systems is the “MammoWave”, which utilises a rotating antenna around a patient’s breast. By

analysing the Real/Imaginary complex measurements for both S_{1-1} and S_{2-1} at each position, an image can be created to show where there is a lesion or area of concern.

Research performed by Ghavami et al. detecting inclusions within both cylindrical and spherical objects has produced power density readings with high accuracy [4]. This utilised two omnidirectional wideband bowtie antennas, with one fixed and the other rotating around the phantom, each functioning between 6.0GHz and 10.0GHz. By doing so, the position relative to the primary port can be accurately controlled through computer software.

Bahramiabarghouei et al, have designed a flexible 16-way system for detecting breast cancer, confirming that a low cost, comfortable design can be produced [3]. The designs use both a spiral monopole antenna and a stepped rectangular antenna to produce the desired resonant frequencies. These antennas each have a length and width of 20mm, reducing the size of the antenna and increasing the number of elements. The results of this research have successfully shown that over a frequency range of 2.0GHz to 4.0GHz, a low powered antenna system can create a microwave scattering map to calculate the location of a lesion.

Afifi and Abdel-Rahman designed a ring resonator antenna, tuned to approximately 8.9GHz, and successfully produced a 2D image of a breast phantom, through the use of S_{2-1} phase delay [26]. It was noted that with the tumour substance having approximately 5x permittivity and 10x conductivity to breast tissue, the received signal was measured with a substantial phase delay when in the presence of a tumour.

2.2.2. Bone Lesion Detection

Similar research for bone lesion detection has been conducted using UHF antennas in both a single-port (Monostatic) and two-port (Bistatic) system. Ruvio et al. developed a system containing two

antipodal Vivaldi antennas to scan a phantom comprised of a bovine tibia, fibula, muscle, pork fat and turkey skin [1]. This simulates the same materials found within the human body so the theory of operation can be transferred. Each antenna scans the phantom with an $S_{1\text{-}1}$ measurement between the frequencies of 500MHz and 4.0GHZ in steps of 4.375MHz at 18 positions.

The purpose of this is to utilise the effect that dielectric materials have on the transmission and reflection losses of antennas. As an object interacts with the electromagnetic field of an antenna, the transmitting signal can more easily couple to the object than the surrounding material. This in turn changes the losses within each antenna position based on the proximity to the object.

The setup requires submersion in fluid with a similar dielectric constant to muscle to reduce the difference in properties between air and the phantom. This is of course unfeasible when used within a real-world scenario. Another disadvantage for real-world application is that while able to provide a large frequency range and accurately direct the beam to the phantom, the profile causes the setup to be much larger than desired.

Ramalingam et al. produced a singular antenna comprising of two isolated ports, which couple to a central resonator ring at 2.4GHz [21]. It was seen that as the antenna encountered a human limb with fracture, at each measurement point the resonant frequency changed. Ramalingam et al. were then able to use a range of signal processing techniques to increase the resolution of the reconstructed image.

A study conducted by Augustine et al. to analyse bone mineral density was performed as an alternative to using X-Rays [8]. This research was focused on measuring reflection loss changes within an antenna when exposed to reducing thicknesses of the target material, from 8mm to 1mm. Augustine et al. utilised a Coplanar Vivaldi Antenna (CVA), transmitting between 1.0GHz and

8.0GHz, and successfully showed substantial fluctuations in S_{1-1} measurements, which could then be used to calculate the thickness of the target material.

There has been substantial research performed on the capability of RF systems to reconstruct cross-sectional images of the human body. This research is predominantly limited to a single or two-port, rotational system which may possess potential further harm to the user. Many of the studies about bone fracture analysis have shown an appropriate frequency range of between 500MHz and 8GHz. The study performed by Khalesi et al. suggested a preferred frequency range is between 2.0GHz and 2.5GHz, with minor improvement when extended down to 1.5GHz [7]. For the remainder of this study, the antenna specification has been focused on this frequency range.

2.3. ANTENNA DESIGN CHARACTERISTICS

A critical characteristic of an antenna is its radiation pattern, being either broadside, intermediate or end-fire [27], illustrated in Figure 2-1. Based upon the studies shown in section 2.2, both broadside and end-fire antennas successfully reconstructed images of the object under test with Table 2-2 describing antenna characteristics. *Beam direction* refers to the angle at which the main beam is transmitted, *Ultra-WideBand* refers to the frequency range the antenna as a proportion of the central frequency and *Contact with the patient* indicates if the antenna needs to be physically touching.

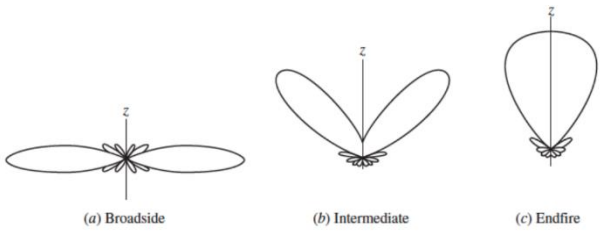

Figure 2-1 – Radiation patterns of broadside, intermediate and end-fire antenna [27]

Table 2-2 – Summary of antenna design characteristics

Criteria	**Patch [3], [5]**	**Bowtie [4], [7]**	**Spiral [3]**	**Resonator Ring [21], [26]**	**Vivaldi [1], [8]**
Beam Direction	Broadside	Broadside	Broadside	Broadside	End-fire
Ultra-WideBand	No	Yes	Yes	No	Yes
Contact with patient	Yes	No	Yes	Yes	No

The bandwidth of a UWB antenna is standardised by the Federal Communications Commission (FCC) for the emission of a UWB antenna occupying more than 500MHz or having a fractional bandwidth of at least 20%. Using $S_{1\text{-}1}$ measurements, the centre frequency can be calculated using equation (1) or can calculate fractional bandwidth in equation (2). The upper frequency, *fH*, is defined as the highest frequency of the -10dB emission point while the lower frequency, *fL*, is defined as the lowest frequency of the -10dB emission point.

$$\left[f_C = \frac{f_H + f_L}{2}\right] \quad (1)$$

$$\left[BW_F = 2 * \left(\frac{(f_H - f_L)}{f_H + f_L}\right)\right] \quad (2)$$

Due to the project initially requiring an unknown quantity of antennas, an end-fire configuration was selected to limit any mechanical interference between neighbouring antennas. This in turn limited the design to Yagi-Uda, Log-periodic and CVA and Antipodal Vivaldi Antenna (AVA) designs, as they were producible on Printed Circuit Boards (PCB). The CVA and AVA designs were then selected due to their ability to transmit across a wider frequency range, as well as having established designs shown in section 2.2. The AVA design was chosen over the CVA, as it was arguably a simpler design for an initial prototype, which could then be developed into a Balanced AVA (BAVA) utilising either a three-layer board or two boards sandwiched together.

Dixit and Kumar wrote a survey describing the different alterations to a standard AVA design, improving the frequency response [28]. This includes different shaped radiating curves, various

materials and if any patches can be added to the design. Various characteristics were investigated during the design process, while others are ignored due to being unnecessarily complex for this study.

2.3.1. Nearfield vs Farfield Distances

It was critical to understand how an antenna interacts with neighbouring objects within its near-field and far-field ranges and therefore where the phantom should be placed. The far-field region is described as where the radiation pattern is unaffected by the distance from the antenna.

The performance of an antenna can degrade if an object or additional antenna is in the reactive near-field range [29]. This increases the complexity of reconstruction calculations as the relationship between the E and H fields is difficult to measure.

The three field ranges for antenna emissions are described as reactive near-field in (3), radiating near-field or Fresnel region lesser than in (4), and the far-field or Fraunhofer region greater than (4) [29]–[31]. Calculations use *D* as the largest antenna dimension and then use λ as the frequency wavelength.

$$\left[Reactive\ Near\ Field \leq 0.62 * \left(\sqrt{\frac{D^3}{\lambda}}\right)\right] \quad (3)$$

$$\left[Fraunhofer\ Distance = \left(\frac{2 * D^2}{\lambda}\right)\right] \quad (4)$$

Within the reactive near-field region, the E-field and H-fields are out of phase by 90°, thus being reactive. Within the radiative near-field region, the radiating fields are more regular than the reactive fields, however, can still vary more than in the far-field region.

Yaghjian describes the behaviour of far-field regions as where the radiation pattern is unaffected by the distance from the antenna. Both electric and magnetic fields continue to decrease linearly, while the power density decreases exponentially as the distance from the antenna increases [29].

2.3.2. Further Vivaldi Designs

This section describes the research carried out on further AVA designs that transmit within the UHF band. A range of designs was selected to better understand the capability and design improvements of the antenna.

Nurhayati et al. provided a basic shaped AVA with the appropriate dimensions to function between 2GHz and 4GHz [32]. The calculations required for the flair seemed unnecessarily complex for this type of antenna.

Schneider et al. designed their antenna to be capable of transmitting between 810MHz and 12GHz, confirming the extensive wideband capability of this design [33]. The antenna BALUN incorporates an extended ground curve, at the connector end, which gradually changes the 50Ω reference impedance to that of the antenna to reduce mismatching.

Dvorsky et al. designed their antenna by utilising blended radiuses on square panels rather than an exponential curve. This version of the flair curve tends to shorten the antenna length while keeping an even radius when compared to using an exponential curve [34]. Dvorsky et al. also incorporated Vivaldi shaped slots within the conductive region of the antenna, to provide additional edges for higher frequency signals to radiate.

Nassar et al. and Bang et al. focused on improving an AVA with the inclusion of an elliptical parasitic patch and elongated hexagon parasitic patch, [35], [36]. Both studies used identical AVA designs to confirm the impact on beam direction when a patch is included. Along with a curved ground plane, a Balanced-Unbalanced (BALUN) feedline was included, reduced from 3mm to 1mm.

Carro goes into further detail on the purpose of the tapered parallel feed line. The microstrip line is based on having a wider width strip over a large ground plane [37]. This then tapers into a parallel

strip line where the antenna and the ground plane have identical dimensions on either side of the dielectric. The length of the ground plane exponential taper needs to be a quarter of the lowest frequency wavelength. The reduction of the strip line width, therefore, increases the impedance of the line, which is beneficial to the function of the antenna.

2.4. LITERATURE REVIEW SUMMARY

Substantial research has been performed on the development of medical imaging, using a wide range of technologies. It was decided that RF systems using the UHF frequency band were favourable, providing a portable, cost-effective imaging technique for bone fracture analysis. This project focuses primarily on the design, simulation, and experimentation of a UWB antenna system that can be electronically switched, to investigate if this is a practical alternative to mechanical rotation. The final investigation then briefly analysed the received $S_{x\text{-}x}$ and $S_{x\text{-}y}$ measurements from the system to calculate and reconstruct an image of the object under test.

CHAPTER 3. SIMULATED DESIGN MODELLING

The purpose of Chapter 3 is to summarise the process of mastering the commercial research simulation software CST and developing the antenna design. Replications of established Vivaldi designs were simulated as an introduction to the software and an understanding of common design practices. Design progression of the Model-A version of the antenna was then developed and characterised to show it has a UWB bandwidth and an overall VSWR of less than 2.

A cylindrical phantom was replicated using dimensions and materials from previous work to be used as the test subject for the system [7], [38]. Several tests were carried out to show an antenna's optimum distance from the Phantom and adjacent antennas. The distance was selected to be large enough to increase space between antennas, while small enough to decrease the overall system size. A single-port monostatic system was tested to show how the $S_{1\text{-}1}$ and beam pattern changes between different lesion positions in the phantom. An identical secondary antenna was then placed at decreasing angular distances around the centre of the set-up, to analyse its effect and therefore indicate a maximum effective system size. The secondary antenna was then placed 180° around the centre of the phantom, to show how the introduction and then change in lesion position affect $S_{2\text{-}1}$ simulations. This then suggested that if the phantom and lesion remained stationary, with the two antennas rotating around the set-up, it would produce comparable results. The requirement for the system was to introduce a multi-port, fixed position set of antennas which were electrically switched rather than mechanically moved. Due to reflections between antennas and computational limitations, a maximum size of 16 was selected, with an angular spacing of 22.5°. Reduced setup sizes, four at 90° apart and eight at 45° apart, were also tested to determine the optimal response. A comparable two-port setup was required to provide the same simulations as the multi-port fixed position setup to determine if the introduction of additional antennas impacted the system.

For experimental work to be carried out, a holding fixture was required to ensure each antenna remains stationary throughout testing. The antenna was then modified to Model-B to allow positioning within the holding fixture.

3.1. INTRODUCTION TO CST

The researched Vivaldi antennas described in section 2.3.2 were replicated in CST to familiarise me with the software and to understand how to generate $S_{1\text{-}1}$ and Smith chart results. As each antenna was not expected to perform effectively within the frequency range tested, the goal was to gain a further understanding from research papers of best design practices. All designs have vastly different characteristics due to their application; this provides enough of an understanding on how to design the antenna and how it can be improved. The five antennas used for reference were developed by Bang et al., Dvorsky et al., Nassar and Weller, Nurhayati et al. and Schneider et al. [32]–[35], [39].

3.2. MODEL-A SINGLE-PORT DESIGN DEVELOPMENT

It was necessary to design an Antipodal Vivaldi Antenna (AVA), using features selected from the established designs in section 3.1**.** The design focussed on creating a half-wave antenna using a dielectric material of FR-4, as it was low cost and structurally strong. The required operating frequency range was 2.0GHz to 2.5GHz. The antenna dimensions were calculated to achieve a lower cut-off frequency of 1.5GHz, centring load matching at 2.0GHz. The dielectric properties of FR-4 are described in Table 3-1. Section 3.3.1 describes the process of developing the initial concept to the final Model-A design, using several improvement techniques. The dimensional properties of the design are described in section 3.2.2 and then characterised in section 3.3.

Table 3-1 – Dielectric properties of FR-4 material

Material	ϵ_r	Loss tangent	Dielectric thickness	Conductor thickness
FR-4	4.3	0.025	1.6mm	35µm

Permittivity (ε) is described in Farads per meter and equates to the resistance a material has to the formation of an electric field within the material. At an atomic level, the amount of electrical energy needed to polarise the atoms to allow current to flow, permittivity is the resistive force. Similarly with capacitance, as the permittivity increases, the resistance also increases and therefore more energy is stored. Permeability (μ) is described in Henry's per meter and affects how easily a material becomes magnetised and allows the magnetic flux to pass through.

3.2.1. Model-A Design Development

The premise of all antenna conductors is to provide a radiating length proportional to the wavelength of the desired frequency, travelling through its dielectric counterpart as shown in (5). Variable *C* is the speed of light in a vacuum of 299,792,458 m/s, *F* is the desired frequency in Hertz, ε_r is the dielectric constant and *x* determines the multiplier for half and quarter wavelength.

$$\left[\frac{C}{xF\sqrt{\varepsilon_r}}\right] \quad (5)$$

The aperture dimension was set to 48.22mm, as this is correct for a frequency of 1.5GHz travelling through FR-4 material, which shows minor improvement in image processing. Due to how the Vivaldi antenna is constructed, frequencies higher than the aperture width are transmitted more effectively than lower frequencies. The feed line of the antenna is critical to the transmission between input connectors and the resonator and is described by (6), where *h* is the dielectric height, Z_0 is the characteristic impedance, ε_r is the dielectric constant and *t* is the conductor thickness [40]. This resulted in an approximate width of 2.99mm.

$$\left[\frac{7.48 + h}{e^{\left(\frac{Z_0\sqrt{\varepsilon_r+1.41}}{87}\right)}} - (1.25 * t)\right] \quad (6)$$

The minimum reflection loss within the frequency range was simulated at -8.41dB, which is undesirable as having high reflection losses cause poor transmission. Further development was then performed for each characteristic such as width, length, feedline, and aperture curve, to show the effect on frequency response.

3.2.1.1. Antenna resonant width

The width of the aperture of a Vivaldi antenna determines the minimum resonant frequency it can effectively transmit or receive. An initial wavelength of 48.22mm was calculated and testing was conducted on a range of widths between 45mm and 55mm, resulting in confirmation that an increased width produces a lower resonant frequency. Testing demonstrated that minor changes between 48.19mm to 50mm only affected the lower frequency range, increasing the real portion of the reflection coefficient and decreasing the imaginary portion, causing it to become capacitive.

3.2.1.2. Exponential vs Radial flare curve

The aperture of a Vivaldi antenna is critical to its performance and is used to produce a range of resonant frequencies and help guide the beam in an end-fire direction.

The two types of aperture that were researched are an exponential curve and a radial curve. The exponential curve produces a varying rate of change based on the values selected, as shown in the design by Nassar et al [35]. While a radial curve produces a uniform change, as shown in the design from Dvorsky et al [34]. With an exponential curve, while the initial curve rate is low, it resonates at substantially higher frequencies than what is required and therefore unnecessarily increases the antenna length. A radial curve was investigated as an alternative due to the curve rate being constant,

resulting in an overall reduced length for the antenna with minimal degradation to the frequency response. It was decided that a radial curve was used for the remaining testing and further techniques were investigated to improve the reflection coefficients.

3.2.1.3. Curved antenna edges

As a high-frequency signal reaches the edge of a conductor or a sharp edge, a portion of the current is reflected in the source, causing additional losses, and reducing the potential output power of the antenna. This issue can be reduced by introducing curved edges rather than strict angles within the design. The width of each conductor was extended between 2mm and 5mm, to allow space for the curved edges. Return loss testing was performed showing that an extended width of 3.75mm produced the lowest current density at the edges, as well as minor improvement to $S_{1\text{-}1}$ simulations.

3.2.1.4. Ground plane BALUN

The curvature of a ground plane can aid in producing a balanced input. The design by Nassar et al [35] effectively shows this, with the ground plane gradually reducing in width until it becomes a parallel transmission line with the microstrip. A reduced volume of a conductive material caused its resistance to increase, which impacts the real reflection coefficient.

Simulations were performed on a range of ground widths to investigate its effect on current density. As the ground curve increases, maximum current density shifts towards the radiating section of the antenna rather than the feed line. Increasing the width of the ground curve also decreased the resistance of the antenna and marginally extends the bandwidth. A ground width of 40mm was selected, with the feed width of 2.987mm; each side has a radial curve of 18.51mm.

3.2.1.5. Feed length

The feed line is critical to designing an effective transmission line to the radiating portion of the antenna. An extended feedline provides more capability to introduce a BALUN, however, has the most impact on antenna length. It was expected that with an extended transmission line, the resistance would increase as more of a conductor is used.

Testing was performed by gradually increasing the length of feed lines from 6mm, to a maximum of 45mm. As the feed length increases, the Smith chart response rotated clockwise by increasing inductance and resistance. This is caused by Ampere's Law, where an alternating current flowing through a conductor produces a magnetic field and in turn, increases its inductance.

Further research on transmission lines [41] shows that the length starts to have a large effect once the length is greater than 10% wavelength, which was why changes below 10mm had little effect. It was concluded that a feed length of 35mm provided a sufficient response while allowing feed curve investigations.

3.2.1.6. Feed width

The skin depth caused by an AC signal passing through a transmission line determines the feed line resistance due to reverse EMF being greatest at the centre of the feed. The capacitance of a feed line increases with the width due to more efficient coupling between the transmitting track and ground track.

Based on previous calculations, the appropriate feed width for a 1.6mm FR-4 board was 2.987mm, while the recommended feed width of an SMA connector was 1.79mm. Tests were performed comparing the two widths and showed that 1.79mm shifted the resonant frequency from 2.0GHz to

2.2GHz. This was accepted as further investigations into adjusting the bandwidth of the antenna were to be performed.

3.2.1.7. Ground parallel tracks

The selected connector requires mounting pads parallel to the feed line, however, set to a length of 6mm. An investigation was carried out by extending the tracks along the feed line, behaving as additional capacitors in parallel to the ground, reducing overall capacitance. At the full length of 35mm, an additional resonance developed at 1.55GHz, which expanded the bandwidth of the antenna.

Testing was also performed by shifting the distance each track has to the feed line. A reduction in the distance creates a decrease in capacitance, as there is less stored energy within the dielectric material.

3.2.2. Model-A Final Dimensions

Utilising the evidence collected within the experiments above, further development on a final Model-A antenna was performed, shown in Figure 3-1 and Figure 3-2. The antenna has been designed using a two-sided copper on an FR-4 board with an SMA connector input. The board thickness is 1.6mm with a copper thickness of 0.035mm. The ground plane is connected to both sides of the board with the connector being soldered, allowing for copper tracks to increase capacitance to the feed line. Simulation using open space boundaries shows an acceptable $S_{1\text{-}1}$ response and reflection coefficients, described in section 3.3.

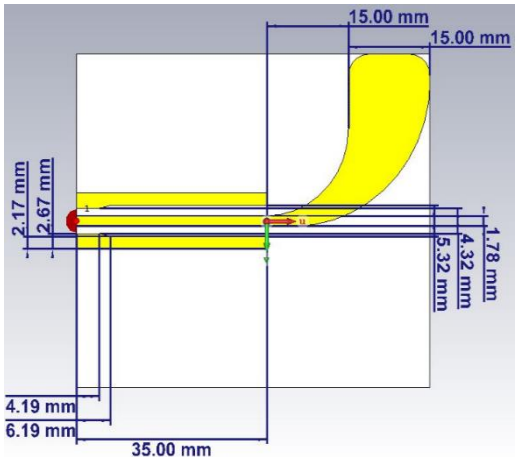

Figure 3-1 – Model-A antenna dimensions - radiator side

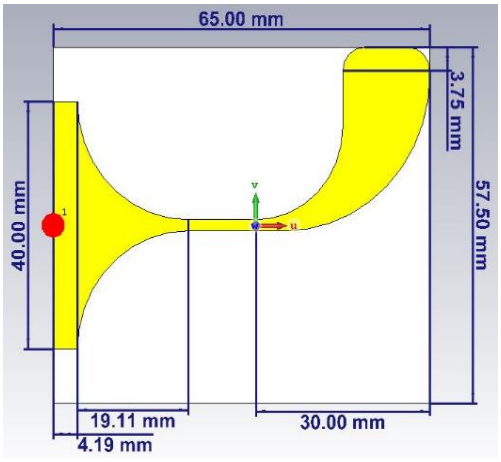

Figure 3-2 – Model-A antenna dimensions - ground side

3.2.3. Model-A Design Development Summary

The development of the Model-A design progressed after experimentation using previously established designs and gradual dimensional modifications. The design utilises an Antipodal Vivaldi Antenna, with a radial curved aperture and additional capacitive feedline tracks. The performance and characterisation of the antenna are described in section 3.3.

3.3. MODEL-A SINGLE PORT CHARACTERISATION

Throughout this section, the process of formal characterisation of a single-port antenna, as described in section 3.2.2, is performed concerning $S_{1\text{-}1}$ reflection loss and beam direction. The characterisation was performed for several test scenarios with different phantom configurations, being no phantom present, a homogenous phantom and a phantom with a lesion. The position of a lesion was determined by the angle relative to position 1 of the system, explained in section 3.3.3. The purpose of this was to understand the extent of the coupling effect an antenna has on a lesion in distinct positions.

The single-port S-parameters are described in 3.3.1, focussing on $S_{1\text{-}1}$ simulations, and the real/imaginary reflection coefficients throughout the frequency range. The far-field directivity was then described in 3.3.2, demonstrating the main lobe direction, gain and beamwidth of selected frequencies. The dimensions and material properties of a phantom with lesion are described in 3.3.3, as this was the basis of the test subject for further simulations. The phantom was then reproduced experimentally for use in practical testing at a later stage of the project. A healthy phantom, with no lesion present, was introduced into the simulation in line with the front face of the antenna. Simulations shown in 3.3.4 were performed at a range of distances to evaluate the coupling effect that a uniform phantom has on the antenna, and what the optimum distance was. A lesion was then introduced, described within 3.3.5, to the phantom at several locations to determine any effect on the antenna.

3.3.1. Model-A Single Port - Reflection Loss Characteristics

To determine the performance of an antenna, and whether it is capable of transmitting across a range of frequencies, reflection loss simulations are needed. These results are described in either magnitude/phase or real/imaginary reflection coefficients, as a ratio to the characteristic impedance. The transmission line of an ideal antenna connects a generator circuit to the radiating element and has a uniform real resistance and no imaginary reactance. For load matching to occur, each element of the system, being the generator, transmission line and load, needs to have equal impedances. This, in turn, provides optimum power transfer to the radiating element and therefore -∞dB loss, and is commonly set as 50Ω for RF systems. The reactance of an antenna is calculated using capacitive and inductive impedances, shown in (7), where *XC* is capacitive impedance, *C* is capacitance in Farads, *XL* is inductive impedance, and *L* is inductance in Henry's and *f* is the frequency in Hertz. A common

upper limit is set to -10dB reflection loss [32], [37], [42], [43] as this equated to 90% power being transmitted.

$$\left[X_C = \left(\frac{1}{2\pi fC}\right)\right] \qquad (7)$$
$$[X_L = 2\pi fL]$$

Simulations for the Model-A antenna were performed between 1.0GHz to 3.0GHz, as shown in Figure 3-3, and simulated *fL* to be 1.524GHz and *fH* to be 2.512GHz. The centre frequency was calculated using (1) to be 2.018GHz and therefore has a frequency bandwidth of 988MHz, being ±494MHz, which is above the required 500MHz. Using the same upper and lower frequency results, the fractional bandwidth was calculated using (2) as 2*988MHz ÷ 4036MHz, giving 48.96%. Both of these calculations confirm the antenna has an ultra-wideband.

Further testing was performed on the far-field beam, which demonstrated all frequencies below 1.8GHz had the front lobe approaching 60° and therefore away from the test body. The lower limit was revised from 1.524GHz to 1.80GHz as this produced an End fire beam, and the upper limit was revised from 2.512 to 2.50GHz to meet the required frequency limit. The bandwidth was calculated using the revised frequency limits, giving a centre frequency of 2.15GHz and therefore a frequency bandwidth of 700MHz, as well as a fractional bandwidth of 32.56%.

Figure 3-3 demonstrates all applicable frequencies are below the required -10dB reference point, equating to a VSWR of 2 and providing a minimum of 90% power transmission.

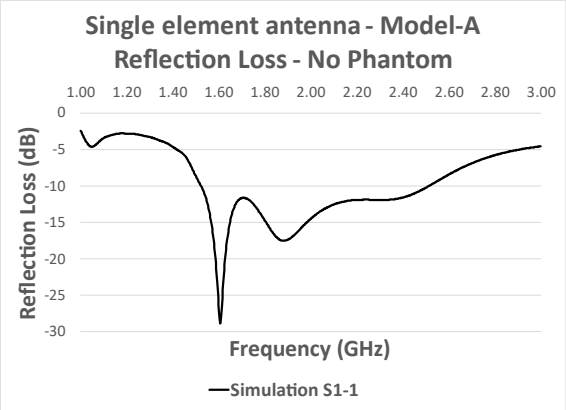

Figure 3-3 – Model-A reflection loss, 1.0GHz to 3.0GHz

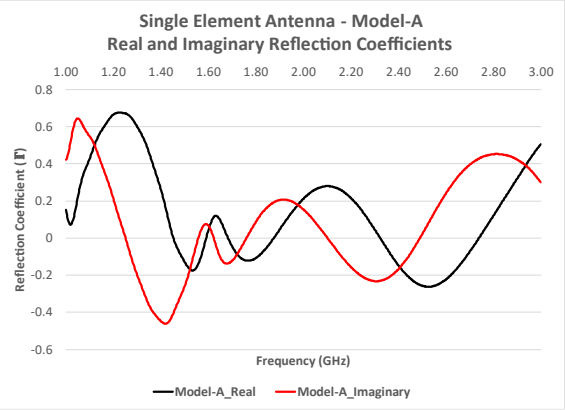

Figure 3-4 – Model-A reflection coefficient, 1.0GHz to 3.0GHz

Simulations throughout the project were taken in two formats, magnitude and phase, as well as real and imaginary coefficients. Magnitude simulations, in the form of reflection and insertion losses, were preferred to visualise the progression of the design and experimentation. The reconstruction code used in Chapter 5 requires the use of reflection coefficients, which describes a ratio with the characteristic impedance.

As an example, a single element simulation with no phantom present, were -10.91db and 36.15° phase offset at 2.0GHz, equal to $\Gamma = 0.212+0.155j$, seen in Figure 3-4. Equation (8) can then be used to calculate the simulated impedances in Ohms, for a 50Ω system. Z_L is the load impedance, Z_O is transmission impedance and Γ is the reflection coefficient. The resistive and reactive impedances at 2.0GHz is therefore $Z_L=72.18+24.03j\Omega$.

An ideally matched antenna is characterised to 50+0jΩ.

$$\left[\Gamma = \left(\frac{Z_L - Z_O}{Z_L + Z_O}\right)\right] \quad (8)$$

Secondly, the half-power frequency bandwidth was calculated by recording the frequencies with a reflection loss of 3dB higher than the peak. The two distinct resonances, being -28.85dB at 1.61GHz

and -17.50dB at 1.88GHz were used to determine the frequency ranges most effective in the antenna. At the 1.61GHz resonance, its half power value of -25.85dB results in a 20MHz bandwidth between 1.60GHz and 1.62GHz. At the 1.88GHz resonance, its half power value of -14.50dB, results at a 220MHz bandwidth between 1.79GHz and 2.01GHz.

3.3.2. Model-A Single Port – Far-field Beam Directivity

Testing was conducted to determine the near-field and far-field distances for the antenna design explained in section 2.3.1. The project is expected to function with the phantom placed within the far-field range to minimise coupling to the antenna which may deteriorate its performance. The three field ranges for antenna emissions are described as reactive near-field in (3), radiating near-field or Fresnel region lesser than in (4), and the far-field or Fraunhofer region greater than (4) [29]–[31]. The antenna field ranges were calculated using the maximum aperture length of 50mm for the value of *D* as this is the largest antenna dimension then using λ as the minimum and maximum frequency wavelengths.

Table 3-2 – Near-field and far-field range calculation results

Tx Frequency	D	λ	Reactive Near-field	Radiating Near-field	Far-field
1.80 GHz	50mm	166.6mm	$R \leq 16.98$mm	$16.98\text{mm} \leq R \leq 30.00$mm	$R \geq 30.00$mm
2.50 GHz	50mm	119.9mm	$R \leq 20.01$mm	$20.01\text{mm} \leq R \leq 41.67$mm	$R \geq 41.67$mm

For the second part of characterisation, the far-field beam direction was analysed to show whether or not the majority of the power was transmitted at the desired angle. Vivaldi antennas are designed to be an end-fire emitter, meaning the main lobe was transmitting at 0°. The half-power beamwidth was determined by the angle at which the power was reduced by 3dB, on either side of the maximum transmission. Commonly, Vivaldi antennas produce a doughnut-shaped beam around the centre of the aperture with the main power radiating from the front and rear. This was similar to what is caused by a dipole antenna, where the conductor resonates in all directions perpendicular to the current flow.

Further improvements can be added to improve the ratio between front and rear lobes however, due to time constraints, this performance was accepted.

Eleven equally spaced frequencies between 1.5GHz and 2.5GHz were selected for evaluation on beam direction for both theta and phi at 0°. It was noted that all frequencies between 1.5GHz to 1.7GHz had the main lobe shift greater than θ=10° when phi ϕ=0°. These frequencies were discounted from the remainder of the project as the majority of power was transmitted away from the phantom.

The charts Figure 3-5 and Figure 3-6 were created to demonstrate the beam angle of the antenna at 2.5GHz when θ=90° and when ϕ=0°. This shows that at θ=90°, the maximum far field gain of 2.53dBi was transmitted at ϕ=358° with a beamwidth of 77°, being -41.5° to +35.9°. Far field gain when viewed at phi ϕ=0° shows a uniform gain. It can be noted that on both axes the rear lobe was only marginally smaller than the front lobe gain, limiting the potential output power towards the phantom. At this stage, time limitations prevented further design work and were an accepted feature to allow further testing to proceed. Figure 3-6 demonstrates a 3D representation of the beam direction at 2.5GHz, which clearly shows a majority of the transmission was end-fire, towards a potential phantom.

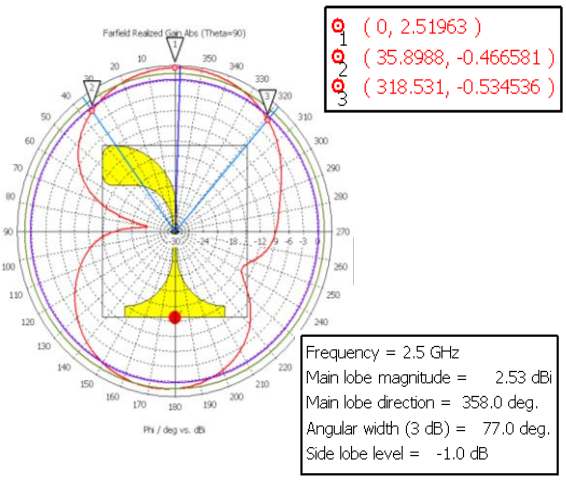

Figure 3-5 – Model-A realized gain in a vacuum with θ=90°, transmitting at 2.5GHz

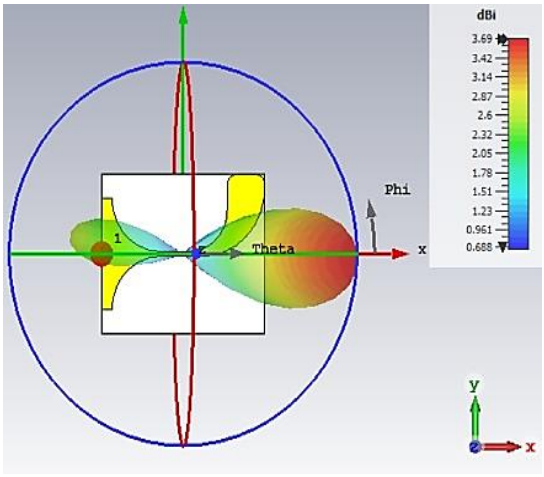

Figure 3-6 – Model-A far-field beam, transmitting at 2.5GHz

3.3.3. Phantom Dimensions and Material Properties

Test objects replicating human tissues, in the form of phantoms, have been studied by many researchers and provide a good insight into how scanning techniques can be used to investigate anomalies. A key aspect of the phantom design was to research materials with similar dielectric properties to that of human tissues, such as bone, muscle, and blood. Many studies have been performed, analysing the electrical and magnetic properties of the human body and finding comparable substitutes [3], [21], [44], [45].

Khalesi et al. and Raiz et al. share similar phantom designs which utilise specifically chosen liquids, rather than using biological materials as Ruvio et al. had done [1], [7], [38]. Utilising a non-biological phantom was selected due to practicality, as well as being readily available within the research group at LSBU. Table 3-3 compares the material properties of the two phantoms designed, as well as the physical size of bone and lesion.

For initial simulations, the design by Raiz et al. has been replicated and shown in Figure 3-7, due to the larger variation between the blood and cortical bone dielectric than was seen in findings by Khalesi et al. [7], [38].

Table 3-3 – Phantom material research

Material	**Human Reference Values [7]**	**Phantom by Raiz et al. [38]**	**Phantom by Khalesi et al. [7]**
Cortical Height (mm)	-	150.00	130.00
Cortical Radius (mm)	-	55.00	55.00
Cortical Dielectric (εr)	11.70	6.25	7.00
Cortical Conductivity (S/m)	0.31	0.28	0.31
Blood Height (mm)	-	70.00	110.00
Blood Radius (mm)	-	7.50	7.00
Blood Dielectric (εr)	59.00	80.00	60.00
Blood Conductivity (S/m)	2.19	2.19	2.00

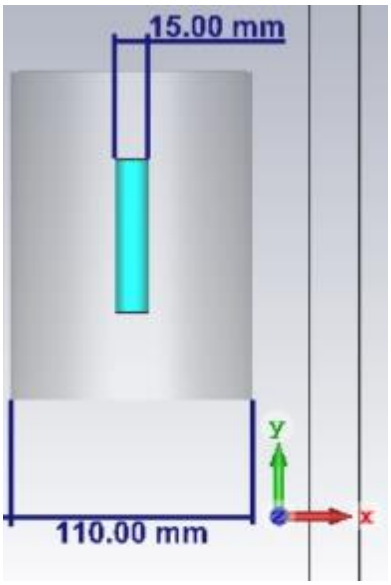

Figure 3-7 – Simulation of Riaz et al. phantom design [38]

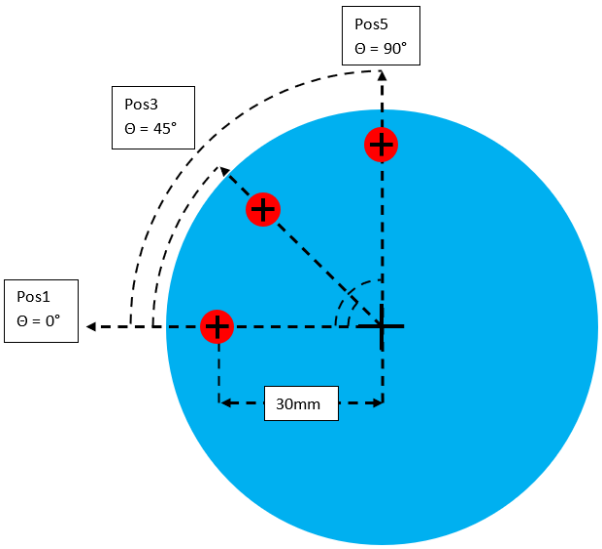

Figure 3-8 – Sketch of phantom lesion position

Figure 3-8 describes a sketch of where the lesion was placed throughout both simulation and experimental testing. The default location for the lesion was set to -30mm on the X-axis and no shift on the Y-axis. To change the position of the lesion, the entire phantom rotated by 22.5°, giving

sixteen equally spaced positions. The term ‘PosX’ refers to the position of the lesion, where ‘X’ was replaced by a numeric value multiplied by 22.5° and subtracting 22.5° for the initial position while remaining at 30mm from the centre. The term ‘PosX’ also refers to the position of an antenna, at the same angle, while remaining at a distance of 85mm from the phantom.

3.3.4. Model-A Single Port - Proximity to Phantom Analysis

A phantom, as described in section 3.3.3 but without a lesion, was included in the simulation to determine the effective distance between its outer surface and the front face of the antenna.

The purpose of this investigation was to determine the extent to which another object nearby affects the behaviour of an antenna. As described in section 3.3.2, objects within the near-field of an antenna cause substantially more coupling and reflections than those within the far-field range. For this project, the optimum distance was described to be the closest possible while limiting coupling to the phantom. A healthy phantom was selected for this investigation as it contains a uniform material so that further simulations including lesions could be performed.

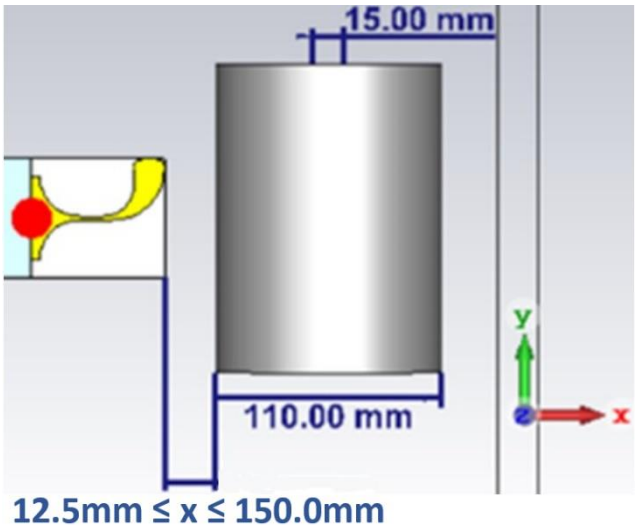

Figure 3-9 – Single element Model-A, distance from phantom front face

Figure 3-9 illustrates the dimensional distance between the front face of the antenna and the closest point of the phantom. Reflection loss simulations were performed at incremental steps of 12.50mm, starting from approximately a quarter wavelength of 12.50mm and ending at 150.00mm as anything above this was too large for practical use. An optimum range was selected to be between 75.00mm and 87.50mm, as these had identical results to one another, while other distances had an average increase of 2dB of loss throughout the frequency band.

Further testing described in section 3.4.1, introduced a secondary antenna, 180° around the centre of the phantom for insertion loss simulations. From there it was determined that 85.00mm was the optimum distance from the phantom.

3.3.5. Model-A Single Port – Shifting Beam Pattern with Lesion

A single antenna was placed 85mm from the front face of a phantom at 0° when viewed on the Y-axis. A lesion, as described in section 3.3.3, was introduced to the phantom for reflection loss and far-field beam pattern simulations. The lesion was placed at three test positions, Pos1, Pos2 and then Pos3, to confirm whether a noticeable change was seen.

With the introduction of a healthy phantom, the realised gain directly in front of the antenna, when viewed at ϕ=0°, was understandably attenuated by 4.552 dBi. Two additional points approximately ±25° from the centreline were also taken as these had substantially higher attenuation of 9.441dBi, however, remained equal in gain. Figure 3-10 shows the far field gain of the antenna transmitting at 2.0GHz, with a lesion in Pos5 and measuring the three points of 65°, 90° and 116°. It can be seen here, as well as further tabulated in Table 3-4, that the gain of -7.339dBi at 116° was noticeably higher than the -8.945dBi shown at 65°. This confirms that the introduction of inclusion influences the beam of the antenna.

Table 3-4 explains the comparison between all five beam pattern tests at 2.0GHz, on how the placement of a lesion affects the far field gain of the antenna. It was noted that with a lesion in Pos1, in front of the antenna, both values at 65° and 116° remained similar in a gain of approximately -8.1dBi. When the lesion was placed in Pos3, there was a substantial difference of 2.691dBi between values 65° and 116°. The effect was lesser when the lesion was placed in Pos5, giving a difference of 1.606dBi between 65° and 116°.

Within a monostatic system, a single antenna performs numerous tests around the phantom, resulting in different results. The position of a lesion causes a phase shift in a reflected signal, which can be analysed by ratio between real and imaginary reflection coefficients

Table 3-4 – Single-Port antenna – far-field with phantom simulation results

Phantom	Gain at 90°	Gain at 65°	Gain at 116°	Difference in 65° to 116°	Attenuation of 90° from 'No Phantom'
No Phantom	+1.482 dBi	+1.321 dBi	+1.297 dBi	0.024 dBi	0.000 dBi
Healthy	-3.070 dBi	-8.070 dBi	-8.195 dBi	0.125 dBi	4.552 dBi
Pos1 (θ=0°)	-2.723 dBi	-8.917 dBi	-9.035 dBi	0.118 dBi	4.205 dBi
Pos3 (θ=45°)	-2.515 dBi	-9.803 dBi	-7.112 dBi	2.691 dBi	3.997 dBi
Pos5 (θ=90°)	-2.479 dBi	-8.945 dBi	-7.339 dBi	1.606 dBi	3.961 dBi

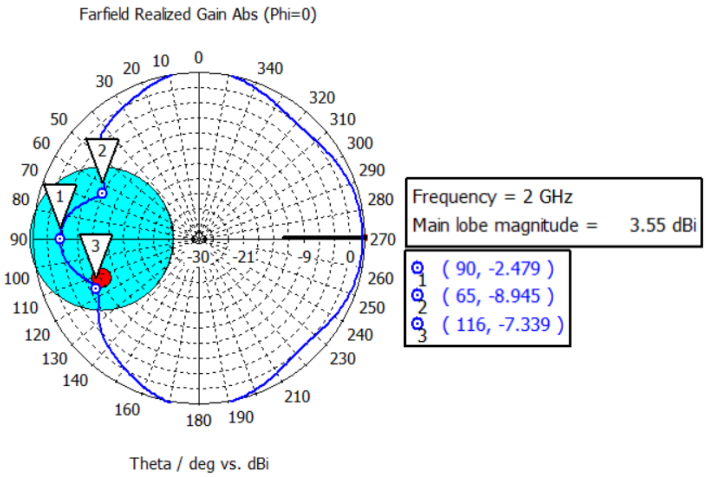

Figure 3-10 – Model-A far-field pattern of lesion at Pos5, transmitting at 2.0GHz

Reflection loss simulations were collected for four test scenarios, being no phantom, healthy phantom, Pos1 lesion and Pos5 lesion. Figure 3-11 shows there was minimal effect on $S_{1\text{-}1}$ for the antenna between each test scenario for frequencies 1.80GHz to 2.50GHz. These frequencies were selected as lower frequencies showed a main lobe direction of 30°. With the inclusion of a healthy phantom, the reflection loss increases by only 0.788dB, with the introduction of inclusion being negligible. This confirmed that the antenna was just within the far-field range while still close enough to be minimally affected by the phantom. As the difference between Pos1 and Pos5 was negligible, but the beam pattern was affected, it was expected that a bistatic system performs better than a monostatic system.

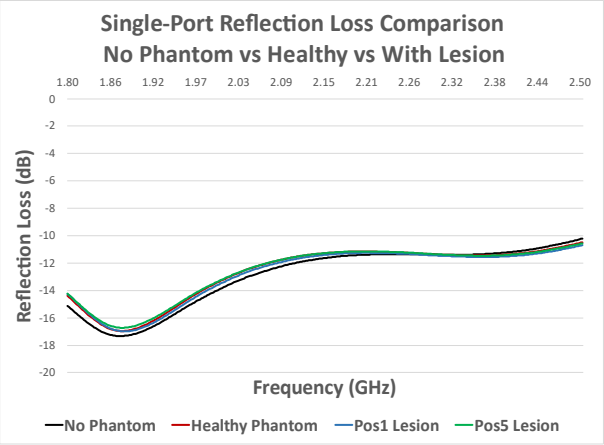

Figure 3-11 – Model-A reflection loss, comparison of phantom tests

3.3.6. Model-A Single Port Characterisation Summary

An antenna was successfully characterised to have a reflection loss simulations were below the desired -10dB reference value, between 1.5GHz and 2.5GHz. Far-field beam tests indicated that only frequencies above 1.8GHz had an effective end-fire beam between ±4° from the centreline.

As a healthy phantom was included in the simulation, coupling had occurred which marginally increased the reflection loss of the antenna. Simulations including a healthy phantom showed an understandable decrease in far-field gain as the signal was attenuated by the material. The lesion was then introduced at a different position for each test, showing a noticeable change in far-field gain, which can then impact the insertion loss signals within a bistatic system. A monostatic system may also be used within this set-up, as it was noted that the real and imaginary coefficients, and therefore phase, varied with relation to the lesion position. Further testing was then performed with a secondary antenna being introduced into the system, providing a bistatic set-up.

3.4. MODEL-A TWO-PORT CHARACTERISATION

This section describes the process of formal characterisation of a system using two Model-A antennas, by introducing a secondary receiver at 180° around the centre of the phantom. The primary antenna was placed in Pos1 while the secondary antenna was placed in Pos9. This develops from a single-port system as described in section 3.3, to allow insertion loss and further beam direction simulations. These tests were conducted in a range of angular distances between the primary and secondary antennas to determine if the results degraded when placed in the near-field range.

The centre point of the system was set to be the centre of the phantom, with both antennas initially being placed 180° apart. For simulations described as 'No Phantom', the model was included, however, the material properties were replaced with a vacuum to standardise the mesh calculations.

Additional distance testing, continuing from 3.3.1, to determine the optimum distance within a bistatic system was performed in section 3.4.1. Return loss and insertion loss values between Port1 and Port2 were recorded while Port2 was placed at incremental angles, shown in section 3.4.2. The beam pattern was then investigated in section 3.4.3 for Port1 with Port2 nearby. Finally, a healthy

phantom and then a phantom with a lesion were introduced to the system with Port1 and Port2 being 180° apart, in section 3.4.4.

3.4.1. Model-A Two-Port – Bistatic Distance Testing to Phantom

Following on from the monostatic testing performed in section 3.3.1, bistatic distance testing was performed to determine the optimum distance between antenna and phantom. The optimum distance allows for a change in lesion position to affect both S_{1-1} and S_{2-1} simulations while minimising close reflections to adjacent antennas.

Numerous distance testing was performed, ranging from 105mm to 155mm between antennas, equal to each antenna being 50mm to 100mm to the phantom. Two scenarios were performed at each distance, with the lesion placed at Pos1 and then at Pos5. The purpose of this was to determine if there was a noticeable change in S_{2-1} simulations when the lesion was rotated by 90°. At the closest distance to the phantom, coupling was more apparent and caused resonances in S_{1-1} and S_{2-1}. At the furthest distance from the phantom, the S_{2-1} simulations did not change between lesion positions. The optimum distance was selected to be 85mm from the phantom face or 140mm between antennas as there was a compromise between acceptable resonance and detection of the lesion.

3.4.2. Model-A Two-Port – Reflection and Insertion Loss Characteristics

Simulations were performed with the primary antenna, Port1, remaining stationary at Pos1 while the secondary antenna, Port2, was placed at intervals of 10°. Reflection and insertion losses were recorded to show the impact of reflections as the secondary antenna approaches the primary antenna. Figure 3-12 illustrates the change in angle between the primary and secondary antenna, to a limit of 90°. Testing concluded at 90° as reflection loss was shown to be similar to a single port simulation, indicating the secondary antenna was out of the near-field range.

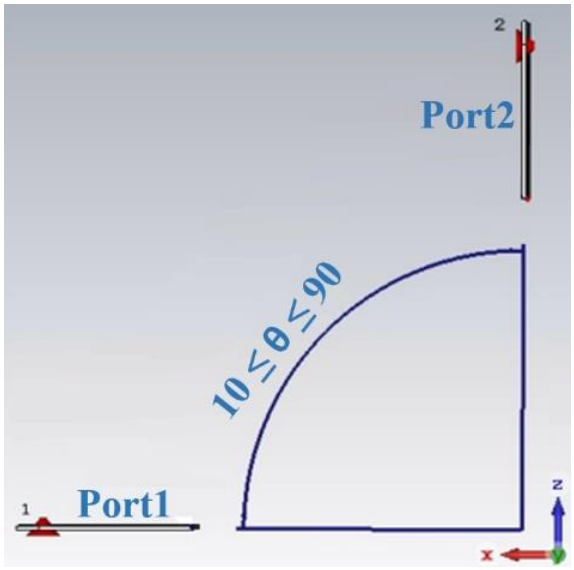

Figure 3-12 – S1-1 close proximity - 10° to 90° in 10° steps

Reflection loss simulations, in Figure 3-13, show interaction between the primary and secondary antennas, as the peak resonance changes from 1.87 GHz to 1.81 GHz. A position of 10° was selected as this produced the most noticeable change and as the secondary antenna was placed further from the primary antenna, the reflection losses became less impacted. Insertion loss simulations, in Figure 3-14, show that angles 10° to 30° have been attenuated between 1.80 GHz and 2.20 GHz, while an angle of 90° was seen to be more uniform. Once the secondary antenna was placed beyond 40°, both $S_{2\text{-}1}$ and $S_{1\text{-}2}$, were identical and decrease in known increments based on Free Space Path Loss (FSPL), calculated using the formula in (9). The value *D* is the distance between antennas, *f* is the transmitted frequency, *C* is the speed of light in a vacuum of 299,792,458 m/s, and G(Tx) or G(Rx) is transmitted or receive gain set to zero.

$$[FSPL] = \left[20Log_{10}(d) + 20Log_{10}(f) + 20Log_{10}\left(\frac{4\pi}{c}\right) - G(Tx) - G(Rx)\right] \quad (9)$$

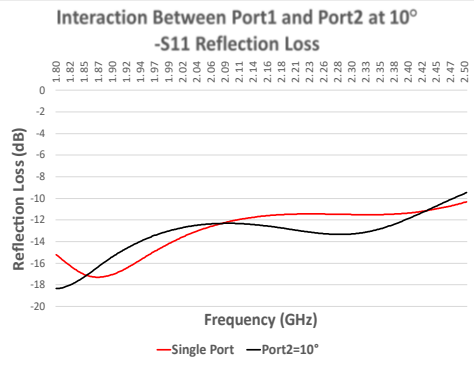

Figure 3-13 – S1-1 Near-field range between Port1 and Port2 at 10°

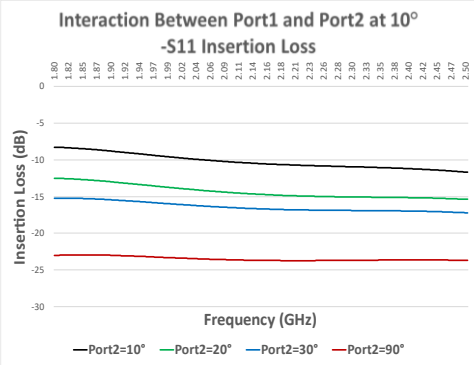

Figure 3-14 – S2-1 Near-field range between Port1 and Port2 at 10° intervals

Further analysis into multi-port, fixed position systems are investigated in section 3.5, and limit the quantity to 16-ports. This increases the angular positioning of adjacent antennas to 22.5°, rather than the previously tested 10°. The previous results continue to be applicable as they show the extent of interations between adjacent antennas. Further simulations were performed with the secondary antenna being placed at 22.5° intervals to compare with a multi-port fixed position system.

To supply an equal number of simulations to what was collected in a multi-port system, several rotational scans were performed. Initially, Port1 was placed in Pos1, while Port2 was placed in Pos2 to simulate $S_{2\text{-}1}$. The secondary antenna, Port2, was then placed in Pos3 to provide $S_{3\text{-}1}$ and this continued until $S_{16\text{-}1}$ was reached. The primary antenna, Port1, was then placed in Pos2 to allow for $S_{1\text{-}2}$ up to $S_{16\text{-}2}$ simulations. This continued until all possible simulations were performed.

3.4.3. Model-A Two-Port – Beam Pattern Investigation

Far-field beam pattern simulations were performed with the secondary antenna placed at Pos2, Pos3 and then Pos5. These positions were selected to allow for accurate comparison when a multi-port, fixed position system was simulated at equal angles. These results were compared to a single-port

beam direction, shown in section 3.3.2, showing that an additional antenna in the near-field range causes reflections.

There was minimal effect on the antenna when viewed at θ=90°, resulting in the frontal lobe shifting by a maximum of ±4° throughout the frequency range and antenna placements. This is shown in Figure 3-15, where the peak power was at 4.19°, with a beamwidth of 78.77°, compared to a single-port test having peak power at 3.0° and a beamwidth of 79.71°. There was a noticeable attenuation in the amplitude of 1.07 dBi with a secondary antenna at 22.5°, compared to 1.46 dBi simulated using a single port. The cause of this is seen in, where the introduction of a secondary antenna causes reflections at the opposite angle. As seen in Figure 3-16, when the secondary antenna was set 22.5° anti-clockwise to the primary antenna, the beam at 292.5° decreases while increasing at 247.5°. With the primary antenna shown to be 270°, at 292.5° the beam magnitude decreases from 1.876 dBi to 0.828dBi, while at 247.5° it increases from 1.880 dBi to 2.597 dBi when compared to single-port testing.

This interference was detrimental to the performance of the antenna as it causes reflections back to the transmitting antenna and therefore can increase reflection loss. For rotational scanning, it may be beneficial to discount any antenna results performed within a 90° angle to remove any distorted signals.

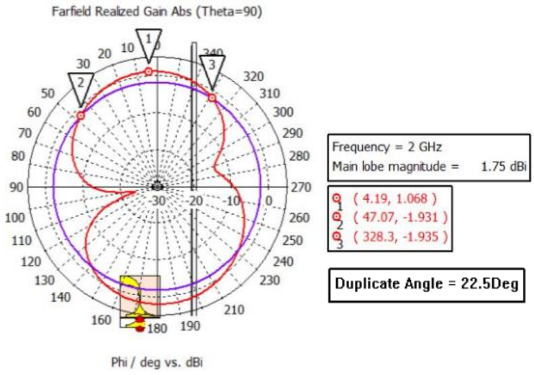

Figure 3-15 – Port1 far-field with Port2 set to 22.5° - Theta=90°

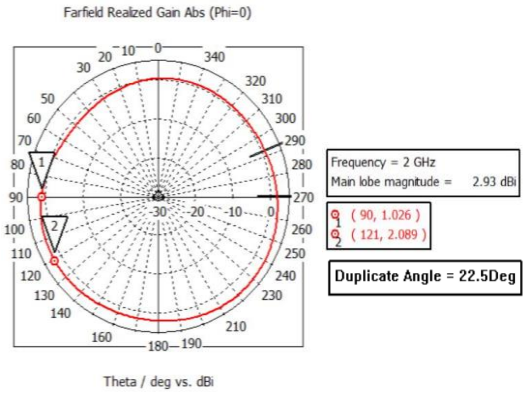

Figure 3-16 – Port1 far-field with Port2 set to 22.5° - Phi=90°

3.4.4. Model-A Two Port – Insertion Loss with Phantom and Lesion

Similar to testing performed for a single port in section 3.3.5, and continuing from the bistatic investigation in section 3.4.1, it was critical to determine the effect a phantom and lesion have on the insertion loss between antennas. The primary antenna was placed at Pos1 and the secondary antenna was placed at Pos9, where insertion loss simulations were performed between four test scenarios. These being with no phantom, a healthy phantom, a phantom with a lesion at Pos1 and a phantom with a lesion at Pos5.

There was an expected attenuation for insertion loss when a healthy phantom was introduced to the system, as shown in Figure 3-17. This was due to bone material having a substantially higher electrical and magnetic characteristics to the free space surrounding it, which induces losses. The losses are caused by both reflections from boundary changes, as well as a linear reduction through the uniform material. There was a noticeable change in insertion loss simulations when a lesion was introduced to the system, in the centre of the phantom. The frequencies below 2.10 GHz showed an average of 2dB increase in power, while frequencies above this were attenuated. The lesion was then

moved to Pos1, which was in parallel to both antennas, which had minimal effect on insertion loss when compared to a centre position.

The lesion was then moved perpendicular to the antennas in Pos5, where the results followed a similar curve to healthy phantom simulations. These however had approximately 1.5dB additional power across the frequency band and are caused by the lesion moving away from the antenna's direct beam. This occurs as the signal continues to couple to the lesion, however to a lesser extent if it was directly in front of the antenna. These findings were further explored by incrementing the lesion's distance from the centre.

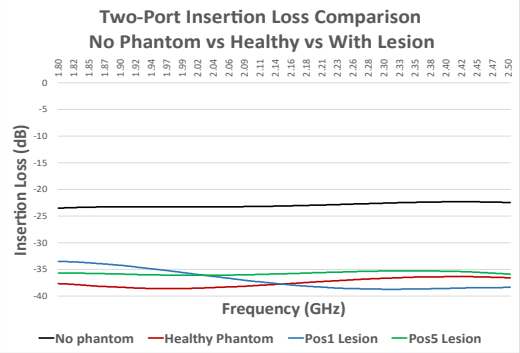

Figure 3-17 – Two-Port insertion loss – No phan vs Healthy vs Pos1 lesion vs Pos5 lesion

To illustrate the effect of changing the position of the lesion, several tests were performed with the transmit antenna placed in Pos1 and the receive antenna placed in Pos9, 85mm from the phantom edge. The lesion was then placed in the centre of the phantom and moved in incremental steps of 5mm up to 30mm, towards Pos1 and then Pos5, described in Figure 3-8. Figure 3-18 shows that as the lesion moves parallel to the direction of the beam, towards the transmit antenna at Pos1, there was minimal change in $S_{2\text{-}1}$ simulations. Figure 3-19 shows that as the lesion was moved perpendicular to the direction of the beam, towards Pos5, insertion loss changed for the majority of

frequencies. This suggests that the system was influenced by the location of the phantom, even when it was not at the edge of a phantom. Although this was interesting to note, all further testing was performed as per Figure 3-8, to allow for a fair comparison between test scenarios.

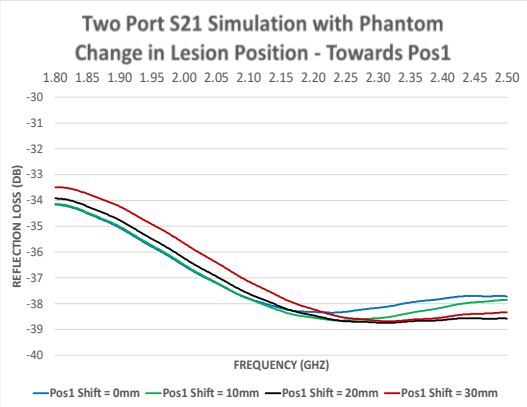

Figure 3-18 – Two Port S2-1, change in X-axis lesion position

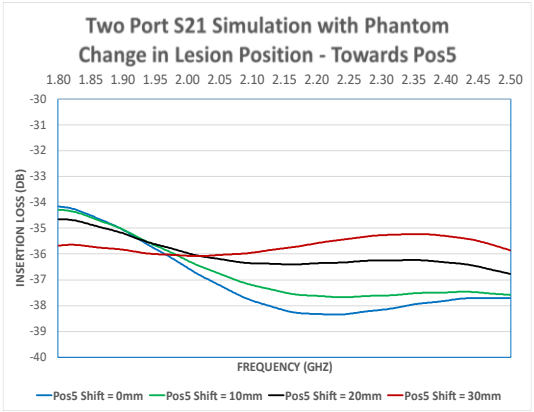

Figure 3-19 – Two Port S2-1, change in Z-axis lesion position

3.4.5. Model-A Dual-Port – Investigation Summary

The result in this chapter indicates that a system comprising two identical Model-A antennas can be used to determine the presence of a lesion but was not capable of detailing the exact location. In a uniform material, the $S_{2\text{-}1}$ simulations for opposite positions are expected to be equal and therefore indicate a healthy phantom. If results between opposite antennas change as they rotate around the phantom, this indicates that the object was not uniform and therefore may have a lesion.

The optimum distance of 140mm from the centre of the structure was selected as this provided a compromise between minimising resonance from a healthy phantom and having sufficient coupling to the lesion. This distance, equal to 85mm from the phantom edge, provides the opportunity for an increased number of angular positions in the system. As the distance between the antenna and phantom decreases, and the angle between adjacent antennas remains the same, the dimensional distances therefore decrease.

Reflections between adjacent antennas within the near-field showed substantial degradation to the reflection loss of each antenna and minor interference to insertion loss. For a rotational system, this may be removed by only selecting simulations when the secondary antenna was within the far-field range of the primary antenna. As the investigation looks into the comparison between rotational and fixed position systems, all results were used to provide comparable results.

The beam direction of the primary antenna was moderately impacted by the presence of a secondary antenna, especially when placed at an angle of 22.5°. This caused signal reflections, producing a beam angle that was tilted away from the secondary antenna. As the angle between the antennas increased, the extent of the reflections decreased, causing the beam pattern to become similar to that seen in a single-port simulation.

A phantom was then introduced to the system with a lesion placed in two different positions. Results were shown to indicate that as the lesion moves positions within the phantom, insertion losses have a perceivable change. A change in lesion position with antennas remaining stationary was comparable to the phantom remaining stationary and the antennas being moved.

The next investigation in section 3.5, moves on to discuss how increasing the number of antennas while remaining stationary may provide similar results to a rotating system.

3.5. MODEL-A FIXED POSITION SYSTEM INVESTIGATION

This section continues from the findings of the two-port rotational simulations at the equivalent multi-port, fixed position system. The proposal for the fixed position system was to create an increased quantity of antennas, capable of being time switched rather than mechanically rotated. This in turn drastically reduces the time under test if an RF switch was used to select a transmit and a receive port.

The limit for a fixed position system was set to sixteen, initially from the angular separation investigation in 3.4.2, showing that reflections had less of an impact after 20°. Investigations were performed between four-ports at 90° separation, eight-ports at 45° separation and 16-ports at 22.5° separation.

The purpose of this was to confirm whether the introduction of multiple new antennas has a detrimental effect on the performance of Port1 or allowed the system to become repeatable as there will be regular performance. The expectation was that additional antennas would cause reflections in the beam and distort the results, however as these effects all antennas equally, the average would account for the distortion.

Figure 3-20 shows the placement of a 16-port system where each antenna was spaced 22.5° apart at an equal distance of 140mm from the centre. The four and eight sized systems were similarly created with a spacing of 90° and 45°, respectively.

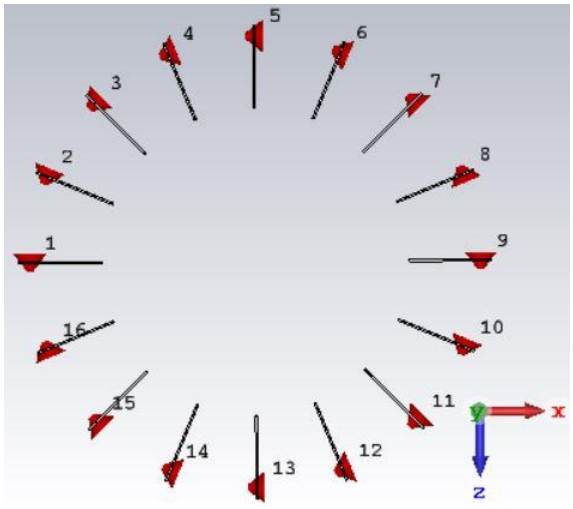

Figure 3-20 – Sixteen-port system, simulation top view, no phantom

A comparison was described in section 3.5.1 for reflection and insertion losses between the rotational system and fixed position systems. This looks at the reflection loss of Port1 in Pos1 with an increasing number of additional antennas. This also looks into the insertion loss between antennas 180° apart, being Pos1 with Pos9 to show the effect of signal reflections.

An investigation into how the beam pattern changes with the addition of new antennas was described in section 3.5.2, with no phantom present. It was expected that with equal antennas on either side, the signal narrows towards the phantom.

A phantom and then lesion was introduced to each system to analyse the effect on both $S_{1\text{-}1}$ and $S_{2\text{-}1}$ simulations between opposite antennas, shown in section 3.5.3. Previous testing had shown that a change in lesion position caused an observable change in insertion loss. This investigates whether the change caused by introducing additional antennas outweighs the change from different lesion positions.

The beam pattern for fixed position systems including phantoms were investigated and are described in section 3.5.4. A healthy phantom was introduced at this stage, with a lesion at Pos1 then Pos5, to show if a multi-port system was affected to the same extent as a single-port rotational system.

3.5.1. Fixed Position Antennas – Change in S1-1 and Sx-1 Losses – No Phantom

This section describes the differences seen for reflection losses on Port1 of all system sizes. Insertion losses were also recorded between the primary antenna at Pos1 and the secondary antenna at Pos9, being 180° apart. This was to analyse the interference seen with multiple antennas added to the simulation and compare to the findings in section 3.4.1 where only a secondary antenna was added.

Figure 3-21 describes the reflection loss characteristics of Port1 at Pos1 and was shown to have minimal changes between single port and four-port systems. This was expected as the distortion

shown in section 3.4.2 was marginal at 90°. However, this changes when an eight-port system was used, as it causes additional losses at frequencies up to 2.30 GHz. This was caused by reflections caused by all additional antennas within the simulation, especially adjacent ones. This worsened with the introduction of a 16-port system, by inducing substantial resonances, which was expected as the adjacent antennas are well within the near-field range. The reflection loss results for each antenna within their respective antenna systems, indicating that a "No Phantom" simulation may calibrate out any errors.

Figure 3-22 describes the insertion losses between Port1 at Pos1 and Port2 at Pos9, being placed 180° apart. The two-Port system was the most stable result as it was the furthest distance between adjacent antennas, reducing potential reflections. There are minor losses when a four-port system was introduced and was similar across all four antennas. An interesting occurrence happened with the eight-port system, where the response was increased by approximately 3dB or half-power across the frequency range. A possible cause of this was that reflections on either side of the transmitting antenna caused the beam to concentrate equally towards the centre of the system and therefore towards the receive antenna. Similar to the 16-port reflection loss simulation, insertion losses had significant resonances across the frequency band. It was expected that this was likely to cause errors with calculations, as the introduction of a phantom and lesion will have minor effects when compared to the current resonances and may be lost in the noise.

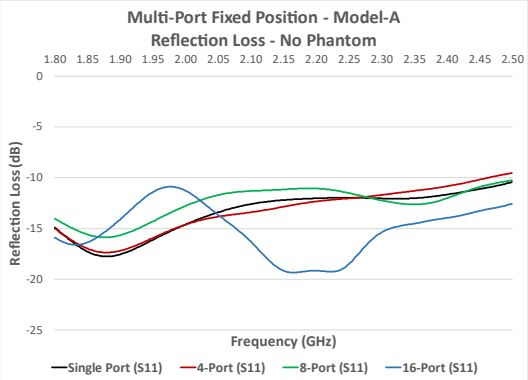

Figure 3-21 – Reflection loss for increased number of fixed position antennas – No Phantom

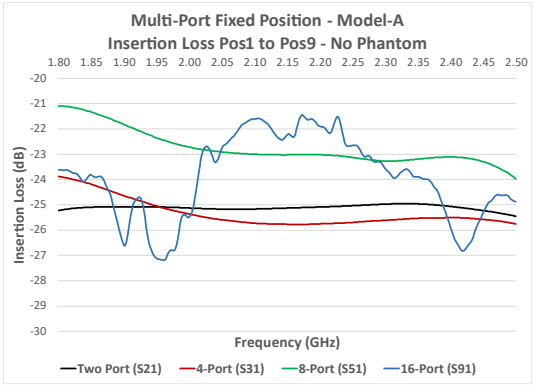

Figure 3-22 – Insertion loss for increased number of fixed position antennas – No Phantom

3.5.2. Fixed Position Antennas – Change in Port1 Beam Patterns – No Phantom

Simulations were performed with each system size to show the beam pattern towards a vacuum phantom. The transmission was from Port1 at Pos1 in each of the systems show how the increasing quantity of antennas affect the beam direction and width. Simulations taken where ϕ=0° show Pos1 was placed at θ=270°, with the main frontal lobe directed at θ=90°. Simulations points of θ=90°, θ=57°, and θ=124° were taken after a four-port in Figure 3-23, eight-port in Figure 3-24 and 16-port system in Figure 3-25 were simulated. The 16-port system showed substantial attenuation at θ=57°, and θ=124°.

The introduction of further antennas has induced additional nulls and minor lobes when compared to a single antenna system in section 3.3.2. It was shown previously in section 3.4.3, that placing Port2 near Port1 caused beam distortion towards the opposite angle. This was compounded with the introduction of multiple elements in the system, equally on either side of Port1 which reflects the beam similarly. Far-field gain at θ=90° decreased from 1.482 dBi using a single port system, to 0.584 dBi using a four-port and 0.894 dBi using an eight-port system. This was caused by periodic nulls within the far-field range, causing maximum power to be transmitted at approximately θ=70° and

θ=110° for the four-port system. The 16-port system, however, produces additional gain at θ=90° to 1.763 dBi by narrowing the front lobe towards the centre of the setup, causing two large nulls.

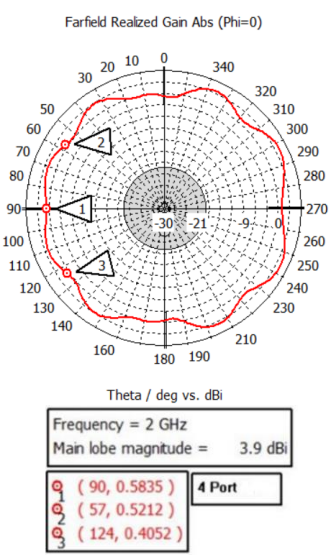

Figure 3-23 – 4-Port Phi=0° at 2.0GHz

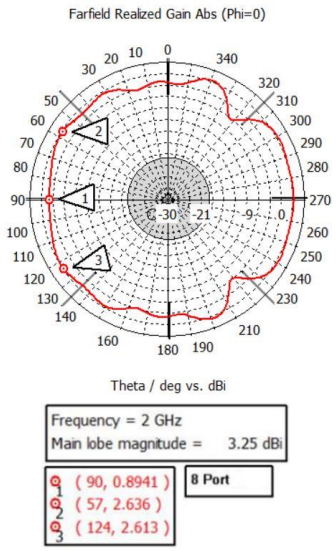

Figure 3-24 – 8-Port Phi=0° at 2.0GHz

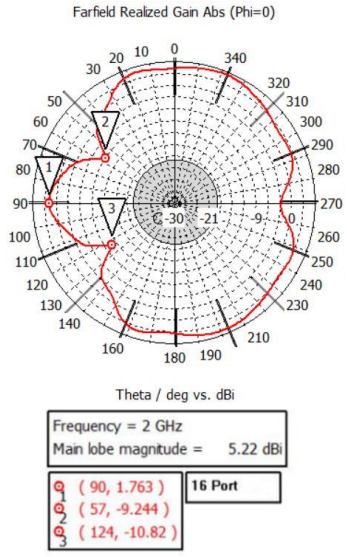

Figure 3-25 – 16-Port Phi=0° at 2.0GHz

3.5.3. Fixed Position Antennas – Change in S1-1 and Sx-1 Losses – With Phantom

This section describes the changes in both reflection and insertion losses for each system size when a phantom and lesion are introduced. Examination of Figure 3-26 and Figure 3-28 shows that four-port and eight-port systems display similar reflection loss simulations between all phantom tests, suggesting that the additional elements within an eight-port system have minimal impact on the primary antenna. There are noticeable resonances for insertion loss, seen in Figure 3-27 and Figure 3-29 when additional elements are added to the system. This can be compared to the previous two-port system in Figure 3-17, where the response was stable across the frequency band and therefore caused by the wave reflecting off adjacent elements.

When the system was increased to 16 elements, substantial resonance occurred as seen in Figure 3-30, as the spacing reduced to 22.5° and therefore within near-field range, calculated in Table 3-2. This does show a more noticeable attenuation between the healthy phantom and one with a lesion present, which suggested monostatic image reconstruction may be possible. The risk with antennas placed within near-field range was that the behaviour of electrical and magnetic fields are less predictable and therefore resonance may not be the same for repeated testing [46], [47].

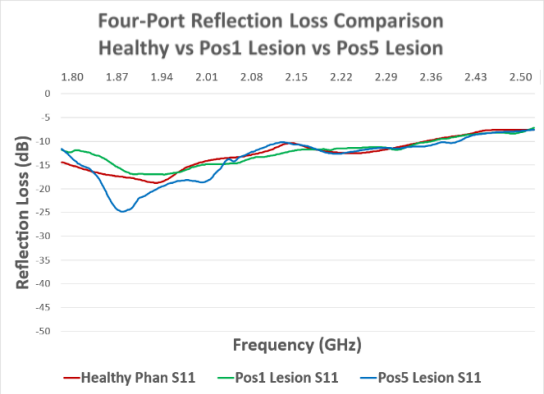

Figure 3-26 – Four-port reflection loss, phantom composition

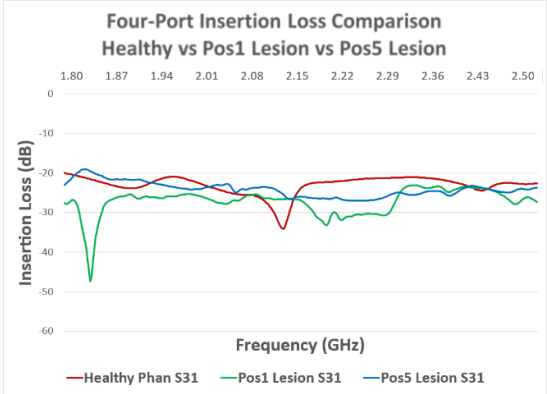

Figure 3-27 – Four-port insertion loss, phantom composition

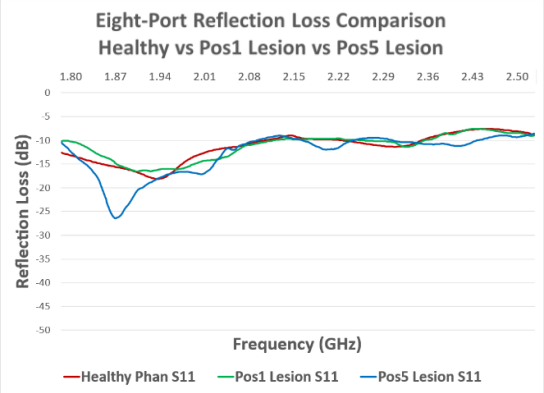

Figure 3-28 – Eight-port reflection loss, phantom composition

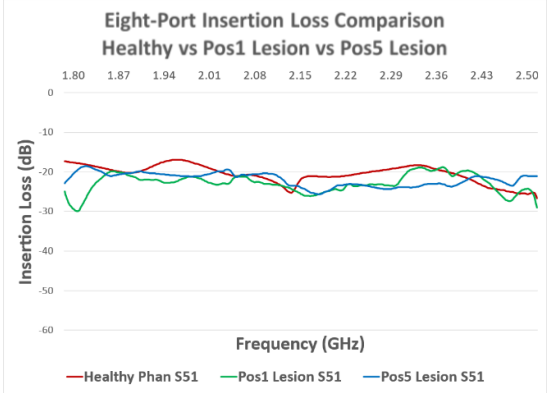

Figure 3-29 – Eight-port insertion loss, phantom composition

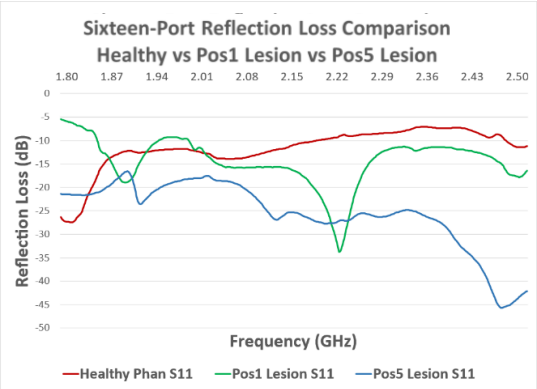

Figure 3-30 – Sixteen-port reflection loss, phantom composition

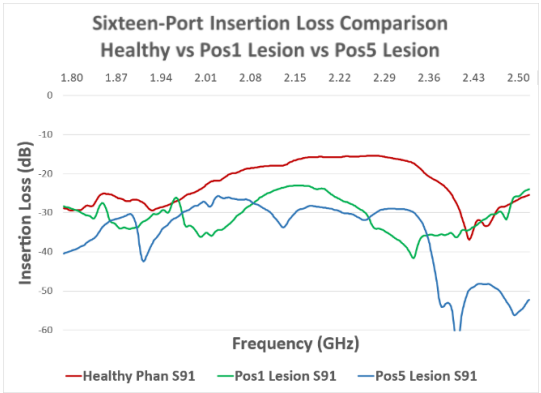

Figure 3-31 – Sixteen-port insertion loss, phantom composition

3.5.4. Fixed Position Antennas – Change in Beam Patterns– With Phantom

This section describes the far-field simulations for the primary antenna at Pos1 for each quantity of antenna set-ups. Previous tests in section 3.3.5, show that a change in lesion position has a noticeable effect on far-field gain simulation. This was repeated, including additional elements to create the four, eight and sixteen element systems to examine if they behave similarly. Initial expectations were that the introduction of more elements would produce reflections and noise which may shadow the any impact caused by a change in position.

A value was taken from the direct end-fire direction, listed as '1', to show the losses caused by introducing a phantom into the system. Additional values of ±33° from the centreline, listed as '2' and '3', similar to Figure 3-25, to show how the beam was distorted between a simulation with a lesion at Pos1 and a simulation with a lesion at Pos5. These angles were selected as there is a clear increase in power of '3' and decrease for '2', between the two simulations.

Simulations for all system sizes were performed on a healthy phantom, giving a reference point denoted as '1' at θ=90°, and approximately equal gain for '2' and '3'. This suggests that the phantom was comprised of a uniform material as the beam was not distorted and only attenuated. A lesion was

then introduced at Pos1, in line with the primary antenna, which increased the gain for '1', with '2' and '3' remaining equal. This result by itself cannot determine if a lesion was present, as a similar response may occur with a different phantom material. A number of samples surrounding the phantom is required to suggest if the phantom is homogenous or not.

Simulations with the lesion placed in Pos5 showed a decrease in gain for '2', being the side furthest from the lesion, which was amplified while '3' was attenuated. Figure 3-32 shows the result of a four-port system, transmitting at 2.0GHz, with the lesion placed at Pos5. Point '2' had a far field gain of -4.952 dBi, while point '3' had -3.940 dBi, giving a discrepancy of 1.012 dBi.

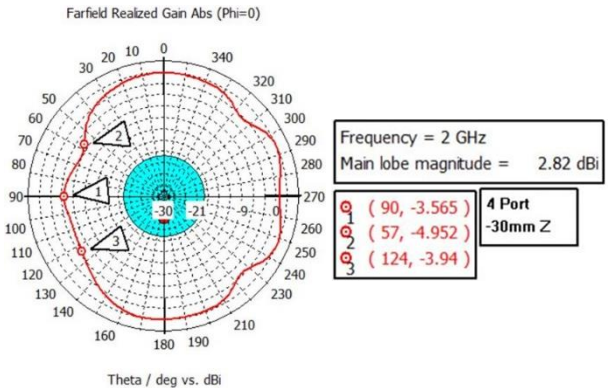

Figure 3-32 – Simulated of far-field pattern using four elements with Pos5 lesion

3.5.5. Fixed Position Antennas – Summary

An increased quantity of elements was introduced to the system allowing for a fixed position set-up to perform similar testing to a two-port rotational system. The system sizes selected were four at 90° spacing, eight at 45° spacing and sixteen at 22.5°, as any further failed to produce sufficient reflection and insertion losses. Simulations that were performed, demonstrated that four and eight-element systems were the most stable, providing comparable results to a two-port system, while a sixteen-port system-induced substantial resonance. Reflection and insertion loss simulations were recorded

for all system sizes and phantom tests, showing a clear variation between a lesion placed in Pos1 and a lesion placed in Pos5. It was seen that a sixteen-port system produced the highest variation for S_{1-1} and S_{9-1} when the lesion moved positions, however, the literature suggests that adjacent antenna in the near-field behave unreliably and therefore may give false results. Further experimental testing was performed and explained in Chapter 4, replicating the simulations that were used here to confirm the results.

3.6. MODEL-B DESIGN DEVELOPMENT

This section describes the modification of the Model-A antenna to the Model-B antenna, to perform experimental testing more conveniently. A holding fixture was created to position the antenna in the correct location relative to each other and the Phantom. This resulted in the antenna requiring additional material to lock into the holding fixture, as well as create separation to limit nearfield interaction with the holding fixture. The holding fixture design was described in section 3.6.1 to allow a maximum of sixteen elements to be placed at 22.5° intervals around the phantom at a minimum distance of 85mm. The design of the Model-A antenna was altered to fit with the holding fixture, producing Model-B, and the dimensional characteristics are described in section 3.6.2. The performance was then analysed in section 3.6.3, to confirm any differences in the two designs and the introduction of a holding fixture.

3.6.1. Holding Fixture Design Development

The holding fixture was created to facilitate a fixed position system and comprised of two sections, the bracket and a joint between adjacent brackets. The dimensions of the bracket are shown in Figure 3-33 and Figure 3-34, the joint dimensions are shown in Figure 3-35 and Figure 3-36, subsequently a full assembly with two antennas is shown in Figure 3-37.

This allowed the bracket to be a final design, while the joint can change the number of elements and the inner diameter, with initially designed to allow for sixteen elements. Both sections were 3D printed from ABS as this was easy to manufacture and had known electrical properties, allowing for simulations to be performed. The purpose of this was to have a holding fixture that can be easily disassembled and stored when not in use. The main section positions each antenna, with a minimum distance of 85mm to the phantom surface or 140mm to the centre. There are additional slots spaced 10mm apart, allowing for minor adjustments to the system if needed.

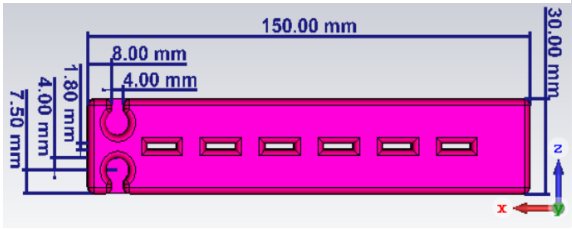

Figure 3-33 – Holding fixture base top view

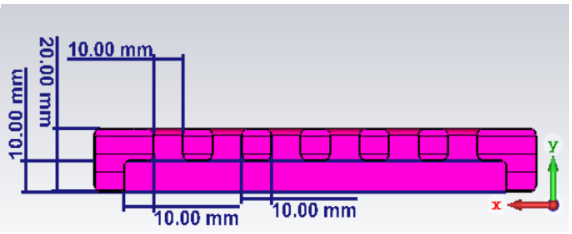

Figure 3-34 – Holding fixture base cut view

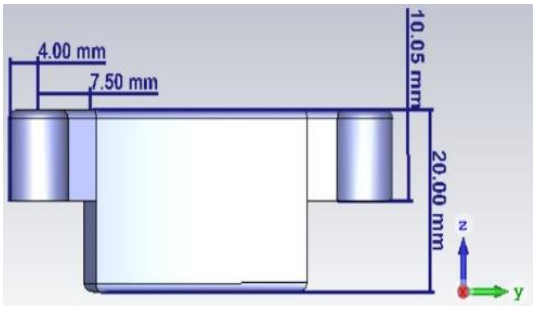

Figure 3-35 – Holding fixture peg side view

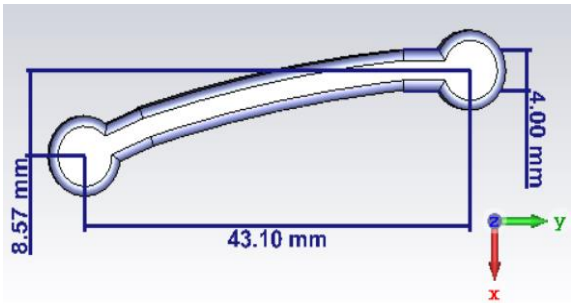

Figure 3-36 – Holding fixture peg, top view

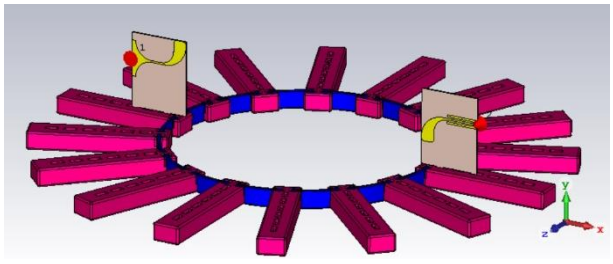

Figure 3-37 – Holding fixture assembly, perspective view

3.6.2. Model-B Design Changes

The antenna was modified to the Model-B version, where two feet have been included and the antenna was extended away from the holding fixture. This was produced by extending the dielectric material which was rigid enough to support the weight of the antenna and the attached cable. Simulations were performed to show the closest placement between the antenna and holding fixture while reducing interference. This allowed the holding fixture to have a limited impact on the antenna and therefore previous simulation results could be read across to the new antenna model.

For the following tests, both sections of the holding fixture were comprised of Acrylonitrile Butadiene Styrene (ABS), which is a common material for 3D printing. Veselý et al. performed dielectric testing on three types of 3D printing materials to determine their permittivity and loss tangents, one of which was ABS [48]. The conclusion of the paper focuses on the frequency range up to 150MHz, which is lower than the requirement for this project. These results were still used for simulation purposes, with the understanding that practical testing may be different. For these reasons, it was acceptable to use the values quoted in Table 3-5.

Table 3-5 – Dielectric properties of ABS 3D print material

Material	ϵ_r	Loss tangent
ABS	3.0856	0.0269

The following tests were performed by increasing the space between the holding fixture and the radiating section of the antenna. The tests increased in steps of 5mm with each dimension being compared to the first design, adjusted antenna by itself and the antenna with a holding fixture. A spacer of 25mm was selected for further testing as this produces an adequate result for reflection loss, insertion loss and beam direction while being small enough to limit damage to the pegs, see Figure 3-38 for new dimensions.

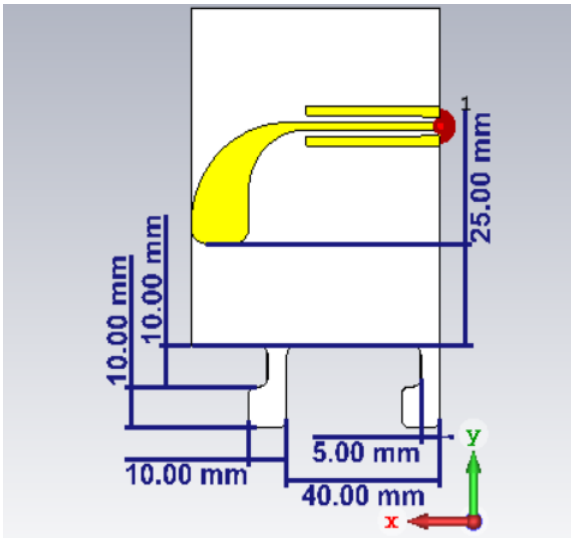

Figure 3-38 – Model-B antenna

3.6.3. Model-A vs Model-B Performance Comparison

Model-A and Model-B antenna designs were compared through reflection loss and beam characteristics to detail any major variations. There was a minor discrepancy between each antenna, however, this was accepted at this stage to allow practical testing to commence.

Performance comparison in Figure 3-39 shows resonance at 1.60GHz is now simulated to be approximately -18.59dB, however has improved the 1.88GHz resonance. At this stage it was not feasible to repeat all simulations, however previous testing was valid for understanding the performance of the system.

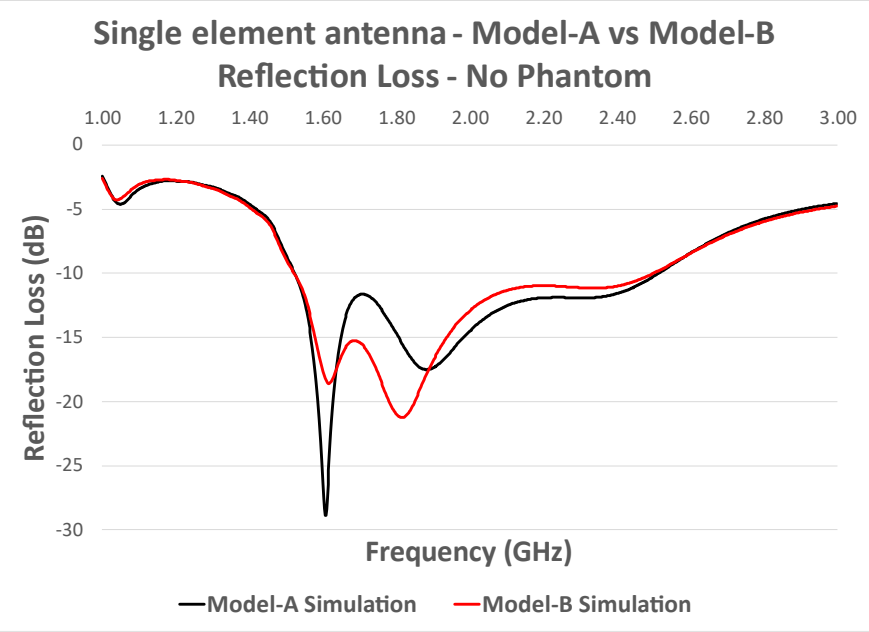

Figure 3-39 – Reflection loss comparison, Model-A vs Model-B

3.6.4. Model-B Design Summary

To summarise, before experimental testing, the Model-A design was adjusted to facilitate use with a holding fixture. The holding fixture was comprised of 3D printed ABS, while the extension of the antenna was through the FR4 dielectric, as these are commonly used materials, cheap and rigid.

Simulations have shown that with a holding fixture present, the lower frequency band was affected by changing its reflection losses. It was agreed that this was an acceptable design change as it produced an improved reflection loss above 1.8GHz, which was the minimum frequency that has shown to have good beam direction.

3.7. SIMULATION SUMMARY

This section has attempted to provide a summary of the simulation design process for modelling a Vivaldi antenna system. The Model-A design was characterised and used primarily throughout

simulations to understand the effect introducing a phantom and lesion into the system has on its performance. Far-field simulations suggested the optimum performance of the antenna was between 1.80GHz and 2.50GHz, providing an end-fire beamwidth of approximately 75°, at a direction of ±4°. Both single-port and two-port systems demonstrated that a change in lesion position impacted $S_{1\text{-}1}$ and $S_{2\text{-}1}$ reflection losses, indicating that the system may be used for image reconstruction.

The number of antennas was then increased to four, eight and then sixteen, in a fixed position system where they could be electrically switched. Simulation results of fixed position systems also showed some interaction between the antennas and lesion position in both reflection and insertion loss simulations. A sixteen-port system demonstrated the greatest change for insertion loss between a lesion placed at Pos1 and a lesion placed at Pos5, combined with a potential set of 240 bistatic results, which suggests it's the optimum quantity.

For practical experimentation, the antenna was modified to the Model-B version and optimised to have minimal performance differences from Model-A. Further testing was carried out experimentally in Chapter 4 to investigate how elements of the proposed system performs in an anechoic chamber.

CHAPTER 4. EXPERIMENTAL SYSTEM APPROACH

This chapter presents the experimental work carried out on the chosen Model-B antenna as described in Chapter 3 modelling section. Here several standard experiments were carried out using a Vector Network Analyser (VNA), Copper Mountain S5065 [49], so that any changes to reflection and insertion losses were recorded and evaluated. All testing was performed inside an anechoic chamber, comprised of Radiation Absorbent Material (RAM) to eliminate external noise from the system and minimise reflections, at LSBU [50]. Initially, a single element was characterised in free space and placed in a holding fixture described in section 3.6. Further testing was then performed using 2, 4, 8 and 16 elements in the same anechoic environment.

Simulation testing clearly showed that the S-Parameters within the system changed as the lesion within a phantom moved position. This chapter reproduces the work in an experimental set-up to confirm that a change in lesion position relative to the transmitting antenna, causes a change in $S_{1\text{-}1}$ and $S_{2\text{-}1}$ measurements.

4.1. EXPERIMENTAL TESTING OVERVIEW

Section 4.2 presents the work to experimentally characterise a single antenna within an anechoic chamber. The characterisation was performed in free space to show return loss and beam directivity in both vertical and horizontal polarization. The holding fixture, designed in section 3.6, was 3D printed and was used as the base for the remainder of experimental testing. Figure 4-10 shows the setup using all 16 antenna elements with the phantom and Lesion set to Position-1. Continuing, each location was referred to as Pos1 to Pos16 for both antenna and lesion placement. The phantom was placed in the centre of the system, however, rotated so that the lesion was closest to each position.

A single element was placed in the holding fixture with no phantom present, to perform $S_{1\text{-}1}$ measurements and compare with measurements performed in free space and simulation. A phantom with similar properties to the one described in section 3.3.3 was placed in the centre of the set-up with no lesion present and further $S_{1\text{-}1}$ measurements were performed. The lesion was added to the phantom at Pos1 and incrementally rotated clockwise by 22.5° to face each position. The return losses were then analysed to show if the introduction and change in the placement of a lesion had an impact on the antenna.

Section 4.3 presents the work carried out during two-port testing to determine the impact of including a phantom and lesion. A two-port rotational system was investigated, as this was comparable to previous work performed by the group, explained in section 2.2. The limitation to this setup was having a minimum rotation angle of 22.5°, selected in section 3.4, whereas previous studies have used a much smaller angular shift such as 10° and 6° [1], [9]. The phantom and lesion was designed within the group and shares similar properties to the one Khalesi et al. investigated [7]. Their experiment used a small lesion with a diameter of 6mm in cortical bone and provided excellent optical resolution of 11mm, equal to $\lambda_{fmax}/4$. With fewer measurement points, it was expected that the resultant reconstructed images of this project would have a lower resolution accuracy, however, was accepted to show proof-of-concept. Initial testing was performed with two elements placed 180° apart in Pos1 and Pos9, with no phantom present to measure reflection and insertion losses of both elements. A phantom without lesion was then included to show the extent of attenuation in insertion loss as the signal passed through a uniform material. A lesion was introduced at Pos1 and incrementally rotated to each position for a new $S_{2\text{-}1}$ measurement. Four full system tests were then performed without a phantom, with a healthy phantom, with a lesion at Pos1, and then with a lesion at Pos5. A full cycle was performed by having the primary antenna stationary, starting at Pos1, while

the second antenna was moved to each remaining position to measure all S_{x-1} insertion losses. The primary antennas then moved to Pos2, and another cycle was performed for all S_{x-2} insertion losses. This was repeated until all S_{x-y} measurements were performed. The results of these tests were then collected to give the full 16-position, two-port test cycle, to have the results compare with the equivalent 16-port system. Some of the measurements were removed to produce an equivalent eight-port system and then a four-port system.

Section 4.4 presents the fixed position testing, using an increased number of elements. Return loss testing was performed with no phantom present to show the effect of including multiple equally spaced elements into the system, being 4, 8 and 16 elements in total. The introduction of adjacent antennas caused reflections to the primary impacting S_{1-1} losses. A phantom was then included without a lesion to show how this affected the system for each number of elements. The lesion was then placed at Pos1, measured, and then placed at Pos5 to be measured again. It was noted that insertion loss measurements between antennas 90° to 135° apart were most impacted by changes in lesion position. Measurements between Pos1 and Pos9, being 180° apart, had minimal change, while measurements between Pos1 and Pos7 showed a noticeable difference in magnitude and phase.

Four full system tests were then performed for all system sizes, similar to the two-port testing. Each element and phantom remained stationary throughout testing, however, the RF cabling was carefully removed and attached to the new ports. This approach was used as an RF switch with 16 inputs was unavailable at the time, therefore switching was performed manually.

4.2. MODEL-B SINGLE-PORT EXPERIMENTAL INVESTIGATION

This section characterises the performance of a single-port antenna for reflection loss and beam direction. The antenna was then placed on the holding fixture designed in section 3.6, to demonstrate the effect of introducing a healthy phantom and lesions in different positions affect its performance.

All antennas were machined from FR-4 sheets with double-sided copper and a SubMiniature type A (SMA) connector soldered to the input, shown in Figure 4-1 and Figure 4-2 with the dimensions described in section 3.6.2.

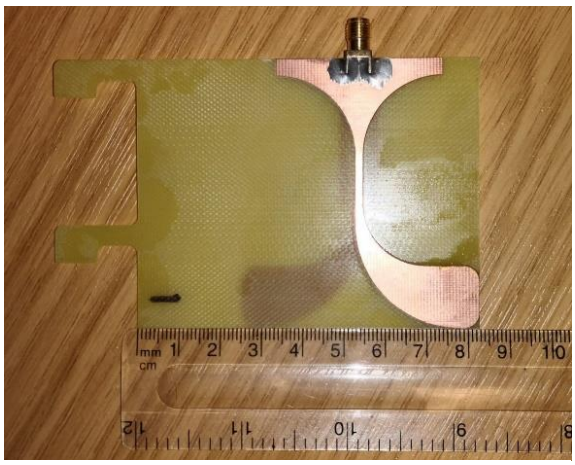

Figure 4-1 – Model-B antenna – Width

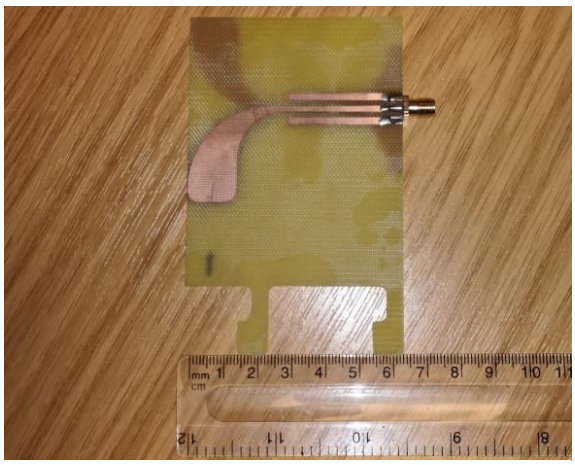

Figure 4-2 – Model-B antenna – Length

4.2.1. Experimental Phantom and Lesion

An experimental phantom was provided by another member of the group, designed by Khalesi et al., with similar dimensions and properties to the simulated phantom in section 3.3.3 [7].

Figure 4-3 – Experimental phantom with lesion designed by Khalesi et al. [7]

To construct a test object representing a bone phantom with a lesion, multiple cylindrical tubes were used to hold liquids comparable to human tissues, as shown in Figure 4-3. Table 4-1 describes the dielectric properties of human cortical bone and blood, and then details other readily available materials as an appropriate replacement. A single jar of 130mm in height and a radius of 55cm was filled with the liquid mimicking cortical bone, while a tube of 130mm in length and a radius of 7.5mm was filled with a liquid mimicking blood. The lesion was placed at 30mm from the centre of the cortical jar, where the angle relative to Pos1 was used to determine a new lesion position, further described in section 4.2.3.

Table 4-1 – Phantom material research

Material	**Relative Permittivity (εr)**	**Conductivity (S/m)**
Bone Cortical	11.70	0.31
Blood	59.00	2.19
Equivalent Bone Cortical (ZMT Zurich MedTech Company, TLe11.5c.045 oil)	7.00	0.30
Equivalent Blood (40% glycerol and 60% water)	60.00	2.00

4.2.2. Reflection Loss and Beam Direction

Here, reflection and insertion loss measurements were taken at 5° increments to plot far-field gain with the antenna placed vertically when $\theta = 0°$ and then horizontally when $\theta = 90°$. A standard set-up using a calibrated horn antenna, ETS-Lindgren's Model 3117 Double-ridged Waveguide Horn [51], was used as the reference transmitter and placed 3m from the rotating platform holding a Model-B antenna as shown in Figure 4-4.

Testing was performed within an anechoic chamber with a Vector Network Analyser (VNA), Copper Mountain S5065 [49], placed outside and RF extension cable assemblies used to feed the signal to the antennas. A full two-port calibration, consisting of open, load, shorted and through, was performed to account for any losses within the cabling and connections, which was performed each

time the test setup changed. Model-B antenna was placed vertically on the rotating platform, facing at 0° and connected to Port1 on the VNA while Port2 on the VNA was then connected to the reference horn antenna, also placed vertically.

All four scatter parameters were measured, $S_{1\text{-}1}$, $S_{2\text{-}1}$, $S_{1\text{-}2}$ and $S_{2\text{-}2}$, which were used to calculate the far-field gain for the Model-B antenna. The platform then rotated by 5°, where another set of measurements was taken, this was repeated for all 72 positions. Vivaldi antennas are linearly polarised, resulting in a single axis of transmission, with reference to the earth, either horizontal being parallel or vertical being perpendicular. An effective antenna is unable to receive signals from the opposing linear direction. Two tests were performed for both axis, with the reference antenna transmitting in the same then opposite linear polarisation.

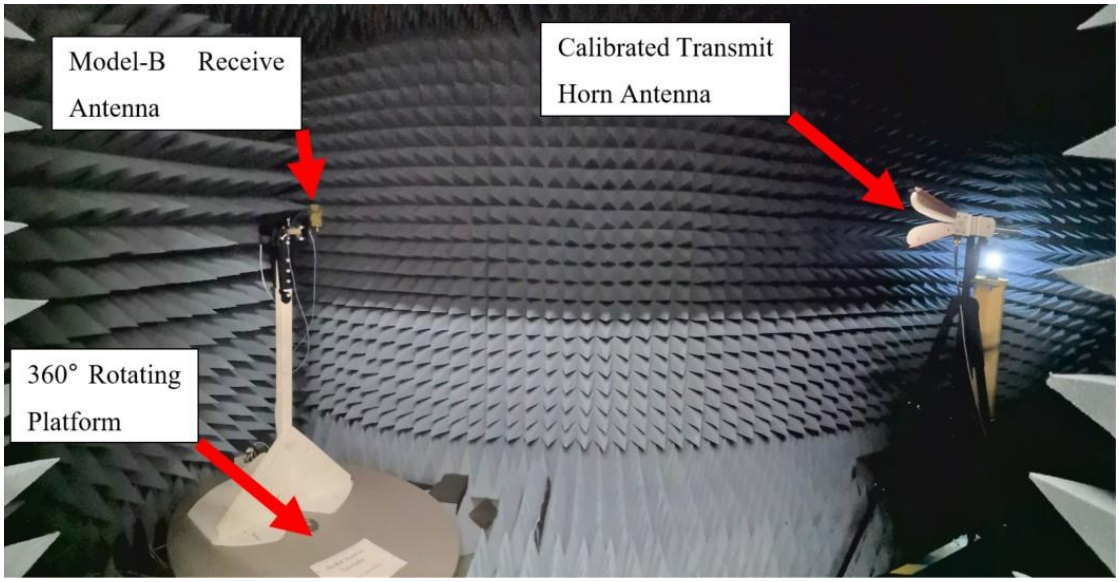

Figure 4-4 – Beam pattern measurement – Anechoic chamber

Horizontal and vertical far-field gain plots were analysed for eleven frequencies between 1.5GHz and 2.5GHz, equally spaced at 100MHz intervals. Similar to simulation results, the maximum frontal gain measured for frequencies below 1.8GHz was at $\phi = 40°$ when viewed horizontally with $\theta = 90°$.

This improved and is shown in Figure 4-5, where the maximum gain was measured to be 2.618dB at 355°. The vertical plot shown in Figure 4-6, demonstrates a similar omnidirectional beam pattern for when the antenna was viewed at $\phi = 0°$. A Frequency of 2.5GHz was selected as this provided the highest frontal gain measurement between ±4° and was comparable to simulated results Figure 3-5.

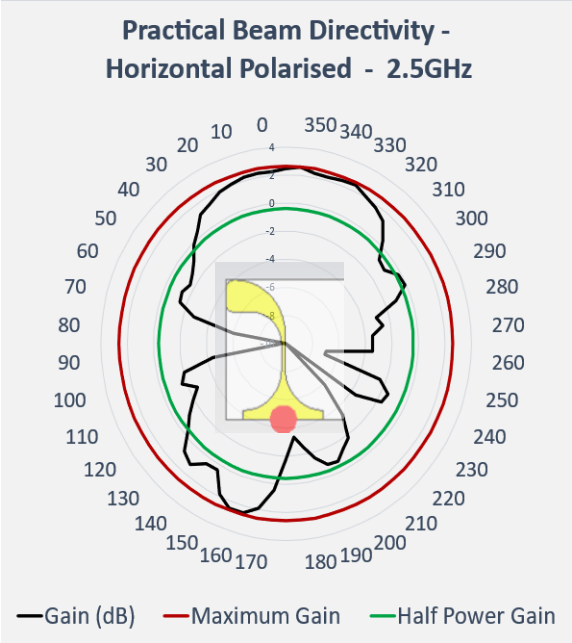

Figure 4-5 – Single port beam characterisation, horizontally polarised

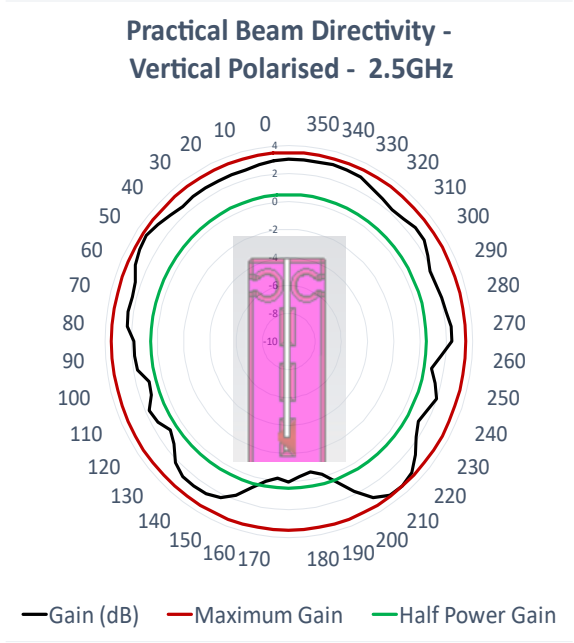

Figure 4-6 – Single port beam characterisation, vertically polarised

Reflection loss measurement on a single element was taken between 1.0GHz and 3.0GHz at steps of 2MHz, with no phantom or holding fixture present to confirm the full bandwidth of the antenna matches simulation. The same process seen in section 3.3.1, was used to measure centre, upper and lower frequencies to calculate bandwidth and determine if it continues to be classified as a UWB antenna.

Using $S_{1\text{-}1}$ measurements, the centre frequency can be calculated using equation (1) or can calculate fractional bandwidth in equation (2). Experimental results are compared to simulations and shown in Figure 4-7, where *fH* was measured to be 2.612GHz and *fL* to be 1.522GHz, resulting in a bandwidth of 1090MHz and a centre frequency of 2.067GHz. The fractional bandwidth calculations used the same upper and lower limits, resulting in 52.73%, confirming the experimental results provide a UWB frequency range.

The frequency limits were then reduced between 1.80GHz and 2.50GHz, as this frequency range provided a stable end-fire beam when viewed at $\theta = 90°$. The same calculations were then performed on the reduced frequency range, giving a centre frequency of 2.15GHz, a bandwidth of 700MHz and a fractional bandwidth of 32.56%.

Simulated and experimental testing show a similar response, however, the frequencies at which the resonances occur increased during measurement testing. This is a common occurrence during testing as the results can be impacted by production quality, close objects such as a clamp, and human error during setup or calibration. Due to the required holding fixture shape, this was placed on the base of the anechoic chamber made of rigid polystyrene. The properties of this material is designed to have minimal impact on the performance of an antenna, however may have caused reflections or distortion from being too close. The modelling created to simulate the antenna was not accurate enough to account for this, however, provides an acceptable response as the antenna continues to transmit appropriately.

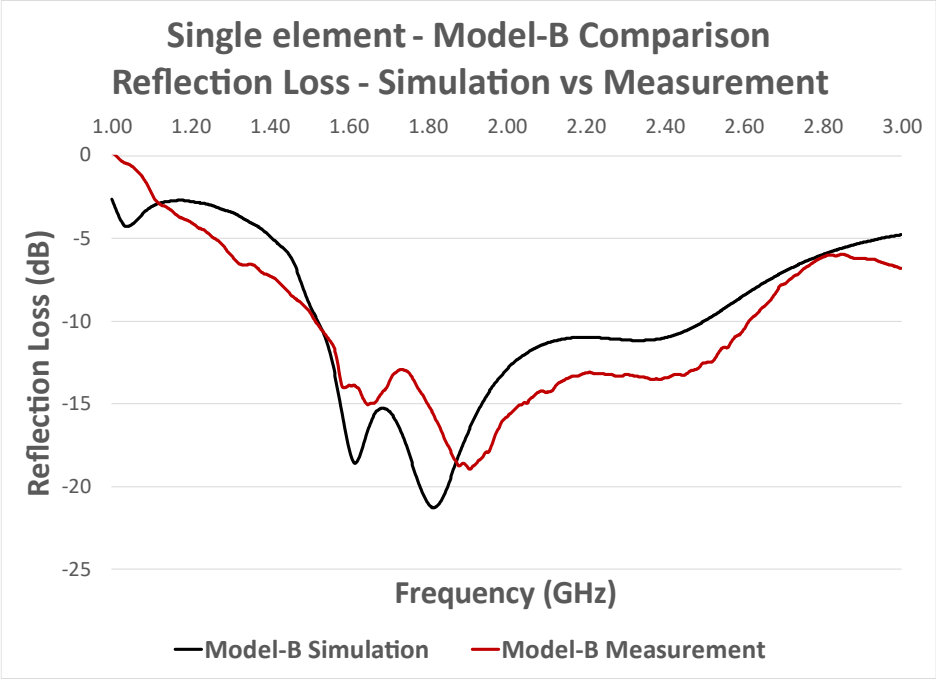

Figure 4-7 – Single element – reflection loss – simulation vs experimental

Further design work into a Model-C, to tune the performance, will ensure experimental testing produced the desired frequency response.

4.2.3. Experimental Test Setup

The holding fixture designed in section 3.6.1 was 3D printed from ABS to provide a 16-position system as shown in Figure 4-8 to allow repeatable placement of each antenna. With regards to testing, the "primary antenna" refers to the antenna connected with Port-1 on the VNA, while the "secondary antenna" refers to the antenna connected with Port-2 on the VNA.

An identical setup to section 3.5, Figure 3-20, was used to position each element and lesion in the correct location. The placement of an antenna was referred to as PosN based on its position facing down vertically, with the initial position, Pos1, being set to the left hand side of the fixture as seen

in Figure 4-11. The position of an inclusion used a similar method, being placed at 30mm from the centre of the phantom and closest to the desired antenna PosN.

For example, Figure 4-8 has no phantom present, referred to as “No Phan” testing. Figure 4-9 shows a phantom with no lesion present and therefore homogenous, referred to as “Healthy” testing. Figure 4-10 shows a phantom with a lesion facing Pos1 and therefore referred to as “Pos1 lesion” testing. Finally, Figure 4-11 shows an identical phantom with lesion, however, was placed facing Pos5, referred to as “Pos5 lesion” testing.

An example of bistatic measurement testing was the primary antenna connected to Port-1 of the VNA was placed in Pos1 of the fixture, while the secondary antenna connected to Port-2 of the VNA was placed in Pos9, with a phantom placed in the centre and a lesion facing Pos1. This measurement therefore is described as $S_{9\text{-}1}$ insertion loss for a Pos1 lesion.

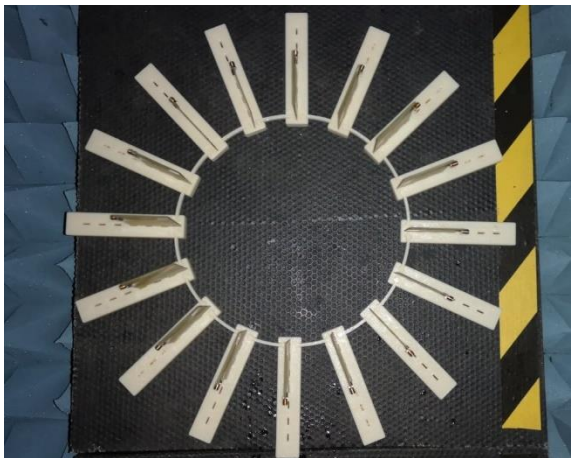

Figure 4-8 – Measurement test A – No phantom present

Figure 4-9 – Measurement test B – Healthy phantom present

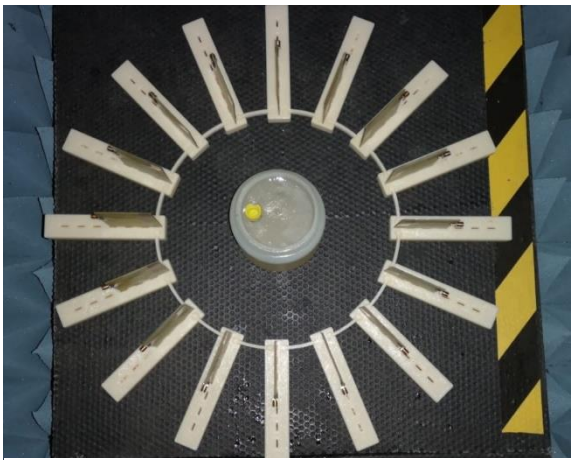

Figure 4-10 – Measurement test C – Phantom with lesion at Pos1

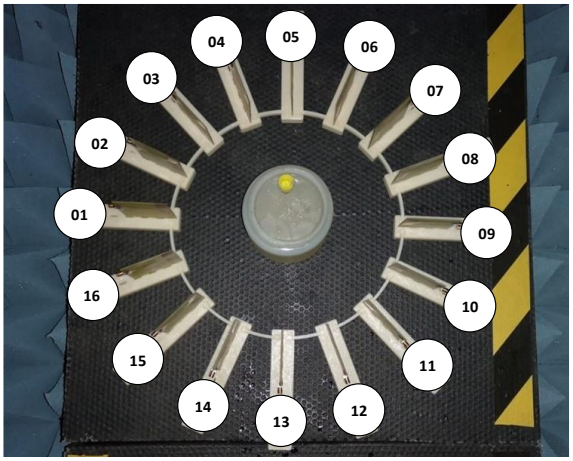

Figure 4-11 – Measurement test D – Phantom with lesion at Pos5

4.2.4. Single Port Phantom Effect

Monostatic tests were performed sequentially, with only a single antenna being placed in the holding fixture, as described in section 4.2.3, and all other positions empty. The single antenna was then removed and placed in each position before performing reflection loss testing, providing $S_{1\text{-}1}$ to $S_{16\text{-}16}$ measurements. Further bistatic testing was performed with an additional antenna used as a receiver, in section 4.3. The reflection loss measurements were taken when a healthy phantom was introduced, to then be used as a reference for when a lesion was added. Figure 4-12 shows that with the introduction of lesion Pos5, the $S_{1\text{-}1}$ losses measured were notably higher at 1.94GHz, by 3.77dB. A sequential test that rotated the lesion to the first nine positions showed the losses increased linearly until the lesion was placed in Pos5. Beyond this, with the lesion placed between Pos6 and Pos9, the losses reduced linearly until Pos9 was like the response of Pos1.

Throughout testing, the VNA was set to transmit at 0dBm, equating to 1mW, where the reflected signal was also measured in Watts, then converted and displayed in decibels. Reflection losses between 1.80GHz and 2.50GHz were shown here to more clearly demonstrate the behaviour

throughout the applicable frequency range. This frequency range was selected as their beam pattern was correct at approximately 0°, towards the phantom. Frequencies below this transmitted at approximately 30°, while frequencies above this were not beneficial to image reconstruction [7].

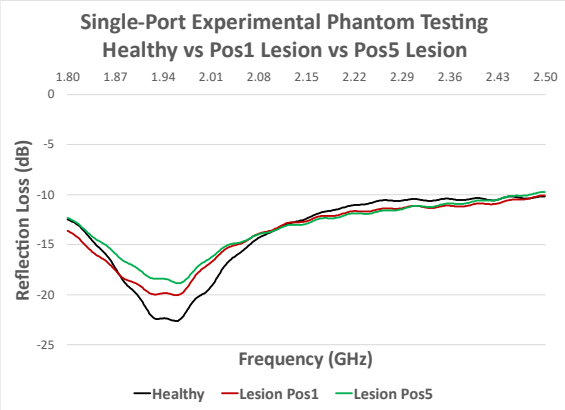

Figure 4-12 – Impact of phantom composition on single port reflection loss

4.2.5. Single-Port Experimental Summary

The single-port characterisation was performed, showing a similar beam pattern and reflection loss coefficient when compared to simulated results. Reflection loss measurements, comparing all test scenarios, confirmed a single-port antenna was capable of coupling with the lesion to different amounts as it moves position. Further testing was required to show the beam pattern with a phantom present as it was not feasible at the time.

4.3. MODEL-B TWO-PORT EXPERIMENTAL INVESTIGATION

This section seeks to assess the performance of a two-element rotational system, comparable to the work performed in section 3.4. A secondary antenna was introduced to the system and connected to Port2 on the VNA, enabling insertion loss measurements. The first subdivision placed the primary antenna in Pos1 and performed $S_{1\text{-}1}$ measurements for when the secondary antenna was placed in

each of the remaining positions, with no phantom present. This was to determine the effect of reflections between antennas placed in the near-field range, to then compare with simulated results. The insertion loss between Pos1 and Pos9, giving $S_{9\text{-}1}$, allowed for a reference measurement to compare with further investigations that included phantoms. The second subdivision describes the effect on $S_{9\text{-}1}$ insertion loss when a phantom with lesion was introduced and placed facing each of the system positions. Far-field beam measurements were not taken at this stage due to time restraints; therefore s-parameter results provided a sufficient comparison.

4.3.1. Two-Port – Near-field Impact on S1-1 Reflection Loss

Experimental testing was performed with the secondary antenna placed in each remaining position of the holding fixture, comparable to the simulations performed in section 3.4.2, with no phantom present. Figure 4-13 shows the $S_{1\text{-}1}$ changes measured from the primary antenna when a secondary antenna at 90°, 45° and 22.5°, equal to a four-port, eight-port, and 16-port system. This was to give an accurate comparison to a fixed position system using the same positions. Reflection loss for the primary antenna, with the secondary antenna placed 90° apart, showed similar coefficients across the required frequency range, indicating the additional antenna did not have an impact. With the secondary antenna placed in Pos3, equal to a 45° angle, reflection loss increased by 2dB at 2.00GHz when compared to a single port measurement. A potential cause of this was reflections off the conductive surface between antennas, as it affects a limited number of frequencies. The secondary antenna was then placed in Pos2, equal to 22.5°, increasing the resonance at 1.90GHz. This confirms that the secondary antenna was within the near-field range and therefore impacts the characteristics of the primary antenna. Finally, the secondary antenna was placed in Pos9 to provide $S_{1\text{-}1}$ and $S_{9\text{-}1}$ measurements with no phantom present, which was then used as a reference when a phantom was introduced.

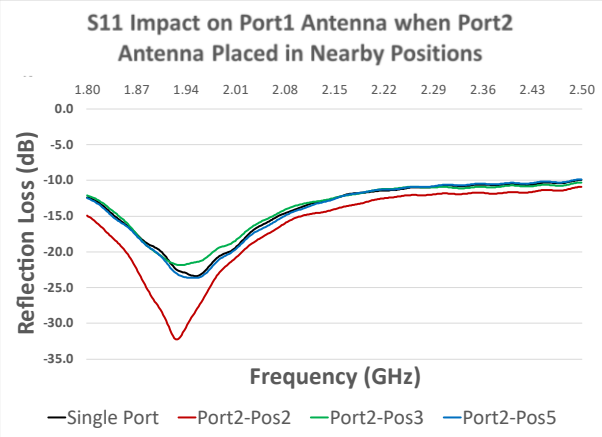

Figure 4-13 – Impact on Port1 S1-1 performance with different Port2 locations

4.3.2. Insertion Loss Comparison – With Phantom

This section investigates the $S_{9\text{-}1}$ insertion loss changes between key phantom scenarios, being healthy, lesion facing Pos1 and lesion facing Pos5. This process isolates the test to a single variable, being the phantom condition, as both antennas remained stationary in an anechoic chamber. Tests were performed with the lesion facing all positions, from Pos1, Pos2, up to Pos16, however only the results for the perpendicular positions, Pos1 and Pos5 were shown in Figure 4-14.

With the introduction of a healthy phantom, insertion loss decreased regularly by 3.2dB up to 2.20GHz, where the amplification began to diminish, while the resonance remained present. This demonstrates that a higher gain was measured when a phantom was introduced, which was in contrast to the findings shown during the simulation, Figure 3-17. The key aspect of the setup was to confirm there was a noticeable performance change when different phantoms were introduced to the system. For both lesion positions, there was substantial attenuation between 1.83GHz and 2.03GHz of 3.0dB from what was expected. Following the remaining frequency response between 2.03GHz and 2.50GHz of the Pos5 lesion, the loss was similar to a healthy phantom with a regular attenuation of

1.2dB. This suggests that a lesion may be present if the frequency response below 2.0GHz was attenuated, however further investigation was required to confirm this.

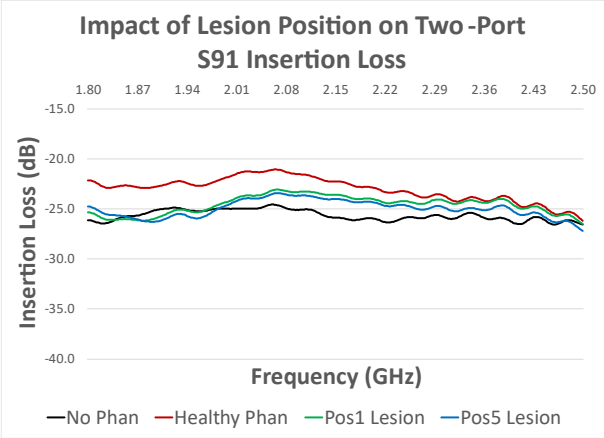

Figure 4-14 – Impact on S9-1 insertion loss from lesion position

Full system testing was performed with the phantom and primary antenna remaining stationary in Pos1, and the secondary antenna placed sequentially in the remaining 15 positions. This provided a full set of $S_{2\text{-}1}$, $S_{3\text{-}1}$ up to $S_{16\text{-}1}$ measurements. The primary antenna was then moved to Pos2 with the secondary antenna being placed in the remaining 14 other positions, as $S_{1\text{-}2}$ had been performed previously. This then provided the full set of $S_{3\text{-}2}$ and $S_{4\text{-}2}$ up to $S_{16\text{-}2}$ measurements. Testing was then repeated until the primary antenna had been placed in all positions to provide the maximum number of measurement points for further analysis. A second scenario was tested where the lesion in Pos5, to give different results to the first scenario during image reconstruction.

It was seen that, once the secondary antenna was outside of the near field range, further movement had minimal effect on reflection loss measurements. The four standard test scenarios were performed during each measurement position, as correct placement of the phantom was more reliable than reattachment of antennas. Therefore, once the antennas were moved, a healthy phantom was then

placed in the centre, a lesion was then added to Pos1, the phantom was then rotated to Pos5 and the antennas were repositioned again.

Inspection of the VNA measurement screen showed a clear change in results, such as in Figure 4-12 for monostatic and Figure 4-14 for a bistatic measurement. This was apparent for all measurement positions; however, the most noticeable difference was seen when antennas were placed between 90° and 270° apart. Meaning, as the secondary antenna was placed at either ±22.5° or ±45° from the primary antenna, the reflections off other antennas caused a larger affect to the system than a change in lesion position.

4.3.3. Two-Port Investigation Summary

Experimental investigations using two antennas on a stable holding fixture with several phantom configurations were investigated. Substantial resonances, shown in $S_{1\text{-}1}$ measurements, between antennas placed 22.5° apart was noticed but lessened when placed 45° apart. The $S_{9\text{-}1}$ insertion loss testing that was performed on three phantom configurations showed a measurable difference in received power when the lesion position was changed. These results match the findings seen in simulated testing, prompting further experimentation using an increased number of equally spaced antennas.

4.4. MODEL-B MULTI-PORT EXPERIMENTAL INVESTIGATION

The following section describes the performance of the primary antenna when additional elements were introduced into the system at regular angles. The simulated finding shown in section 3.5 was used as a basis for the following experimental testing. A similar number of elements were used to construct each setup, being four, eight and sixteen, at an angular spacing of 90°, 45° and 22.5° respectively. This design facilitates the use of a 16-output electronic switch to control which antenna

was active, however, due to financial limitations this was not implemented. To perform a new measurement using different antenna positions, the RF cable was disconnected from one antenna and reconnected to another. Individual 50Ω loads were then attached to the unused antennas, to prevent an incoming signal from being re-resonated and therefore causing further resonance. Further project development using an electronic switching matrix will allow the system to perform faster and more reliable scans as human error will be removed.

An additional 14 antennas were constructed and compared in section 4.4.1, showing variation in manufacturing tolerances. Testing was conducted to demonstrate in section 4.4.2, how $S_{1\text{-}1}$ and $S_{9\text{-}1}$ measurements varied between the number of elements that were introduced, with no phantom present. Finally, a 16-port system was used to demonstrate the effect on performance when phantoms were introduced. A 16-port system was selected to be analysed as this induced the most noticeable reflections off adjacent antennas, becoming the 'worst-case scenario'. An increased quantity of elements provides exponentially more potential measurements, which may increase the accuracy of the results, while the increased reflections can degrade the performance.

4.4.1. Reflection Loss Differences for 16 Model-B Antenna

To accommodate a full 16-port system, an additional 14 antennas were manufactured and tested in the anechoic chamber to confirm their performance. A frequency range of 1.0GHz to 3.0GHz, with a step size of 20MHz, was tested with each antenna placed on the rotating platform. This eliminated any potential coupling to the holding fixture or phantom to isolate the performance of each antenna. Far-field beam analysis wasn't performed on each antenna, due to time constraints.

For each frequency step, the minimum, average and maximum value was plotted in Figure 4-15, showing how the material and machine quality impacts reflection loss. This was a common occurrence due to board and machining tolerances, soldering error and reassembly of the test rig. As

the difference between minimum and maximum was large, calibration files for each antenna were needed, along with assigning each antenna a dedicated position. Prior to phantom testing, an identical measurement with no phantom present was required to be used as a reference during reconstruction.

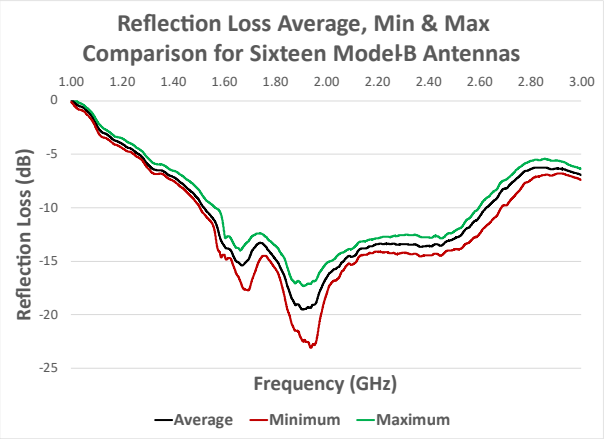

Figure 4-15 – Reflection loss average, min, and max comparison for sixteen antennas

4.4.2. Fixed Position – System Size Comparison – No Phantom

This section performs experimental testing to complement the simulation work in section 3.5.1 and compares with two-port experimental results in section 4.3.1. Previous rotational testing placed the secondary antenna at each position of the holding fixture, incrementing at 22.5°. This showed substantial impact from neighbouring positions, Pos1 with Pos2 and Pos16, which then influenced the beam direction. Simulated fixed position systems showed that resonances worsened with an increased number of elements, however, the beam was symmetrical around 0° as well as all antennas performed similarly.

Figure 4-16 shows reflection losses for the primary antenna as the number of elements in the system increases from 2, 4, 8 and 16. With the introduction of a four and eight-element system, the resonance was initially seen at 1.95GHz reduced in frequency by 60MHz and 30MHz respectively. Both four

and eight sized systems caused an increase in reflection loss at their resonant frequency, which reduces the transmitted power of the antenna. The two-port resonance was measured at -23.61dB, while the four-port resonance increased this to -20.06dB and the eight-port increased it to -16.52dB. This was more impactful than what was seen during simulation in Figure 3-21, where four-port was almost identical, and an eight-port had minor attenuation up to 2.29GHz.

The response measured during experimental work on a 16-port system matched the expected result given from the simulation. The experimental response in Figure 4-16 and the simulated response in Figure 3-21, both develop resonance at approximately 2.15GHz and increase the losses at 1.95GHz. Distortion of the $S_{1\text{-}1}$ response was caused by both reflections of the adjacent antennas conductive surfaces. Testing was performed on each element of a 16-port system, to analyse the average and range of each frequency step. As seen during individual antenna tests in section 4.4.1, the $S_{x\text{-}x}$ measurements followed a similar response which suggests all antennas are impacted equally by adjacent antennas.

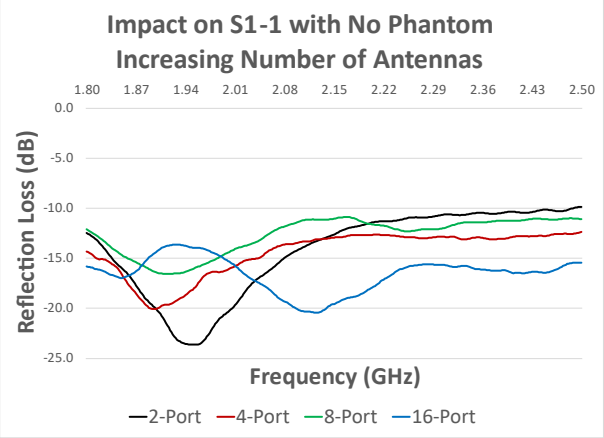

Figure 4-16 – Impact on S1-1 with no phantom – increasing number of antennas

Insertion loss measurements between antennas at Pos1 and Pos9 were recorded for all system sizes, with no phantom present, to show the impact on additional antennas. Simulations described in section 3.5.1, Figure 3-22, compliment the results using a two-port and four-port system in Figure 4-17.

Simulations that included eight elements recorded an additional 4dB at the minimum frequency of 1.80GHz, reducing to 2dB at maximum frequency of 2.50GHz. Initially, it was speculated that reflections to adjacent antennas guided the beam towards the phantom, but this wasn't present during experimental work. Noise has impacted experimental tests to a higher degree than simulations on all system sizes and was not limited to a 16-port system.

Simulations performed on a 16-port system demonstrated an increase of approximately 3dB between 2.00GHz and 2.25GHz, which was present during experimental work without the resonance at 2.42GHz. The results were promising for the system sizes, giving similar measurements to simulations, indicating that the tests were performed correctly. Analysis of similar positions, $S_{9\text{-}1}$, $S_{10\text{-}2}$ up to $S_{16\text{-}8}$, revealed only minor insertion loss differences which may have been due to user error and manufacturing tolerances.

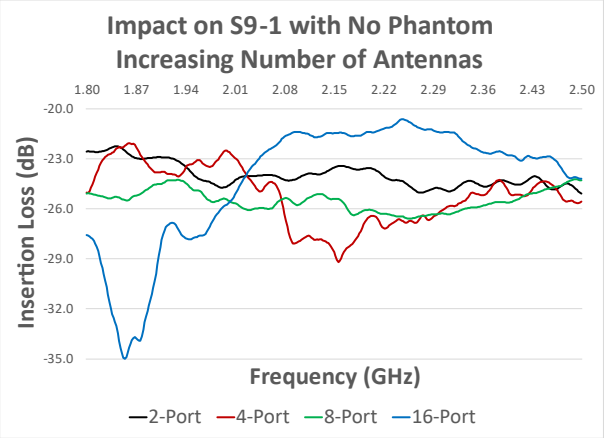

Figure 4-17 – Multi-port system Pos1 to Pos9 insertion loss comparison – no phantom

4.4.3. Fixed Position – System Size Comparison – With Phantom

This section explains the experimental testing performed with three phantom configurations to show the impact on $S_{1\text{-}1}$ and $S_{9\text{-}1}$ measurements. Testing was performed on all system sizes and phantom configurations to demonstrate if the reflections caused by additional antennas masked the changes between lesion positions.

Figure 4-18 graphs the $S_{1\text{-}1}$ reflection losses measured using a healthy phantom, a phantom with a lesion at Pos1 and a phantom with a lesion at Pos5. There was no significant attenuation between phantoms beyond a frequency of 2.18GHz, confirming a change in lesion position has minimal effect on the antenna. Figure 4-19 graphs the $S_{9\text{-}1}$ insertion losses for the three phantom configurations. By comparing this to the two-port system in Figure 4-14, additional noise was recorded and resulted in resonances across the frequency range. Both systems measure negligible reflection loss differences between Pos1 and Pos5 lesions, which can even occur due to human error during setup, indicating the lesion position has minimal effect. The introduction of a lesion by itself, however, does cause a noticeable attenuation in measured power across the entire frequency range. The use of this setup may therefore be used to indicate whether a lesion was present but may prove difficult to show the exact location and dimensions. An additional drawback to this system size is the limited potential measurements available, being 4 monostatic $S_{x\text{-}x}$ and 12 bistatic $S_{x\text{-}y}$, and further limiting the accuracy of the reconstruction.

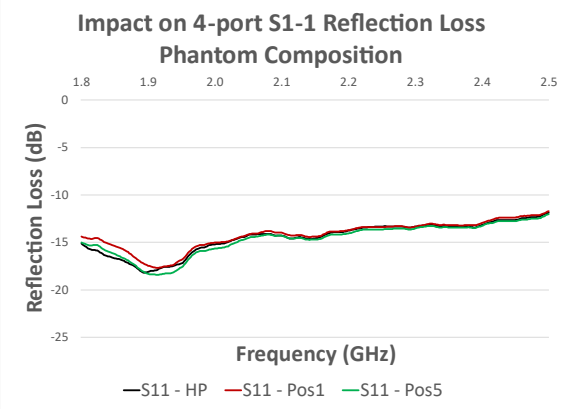

Figure 4-18 – Impact on 4-port phantom composition – S1-1

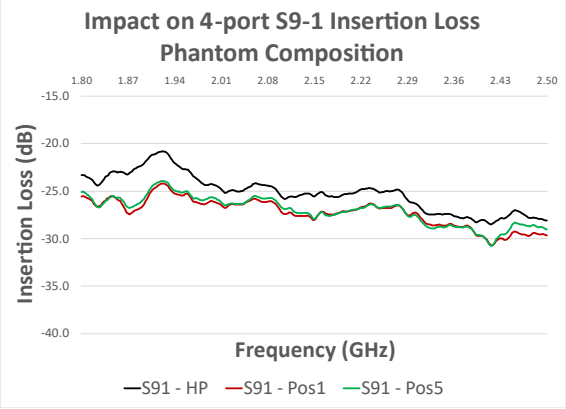

Figure 4-19 – Impact on 4-port phantom composition – S9-1

The eight-port system produced a similar $S_{1\text{-}1}$ to the four-port system, shown in Figure 4-20, where beyond 2.10GHz, there was no significant difference between phantom configurations. Before this, it can be seen that with a lesion placed in Pos1, approximately a further 1dB was reflected in the antenna. Figure 4-21 graphs the $S_{9\text{-}1}$ insertion loss for the eight-port system, demonstrating the most noticeable variation between lesion positions, with Pos5 receiving 1.8dB less power at 1.92GHz than what was measured with the lesion at Pos1. This then reverses at 2.12GHz where the Pos1 lesion measures 2.2dB less than when the lesion was placed at Pos5. For frequencies beyond 2.37GHz, healthy phantom and Pos1 lesion measure comparable $S_{9\text{-}1}$ results, indicating the lesion position has minimal effect. For frequencies between 2.23GHz and 2.50GHz, the Pos5 lesion has a stable attenuation of 0.8dB. This demonstrates that antennas placed 180° apart in an eight-port system are influenced by the location of a lesion within a phantom.

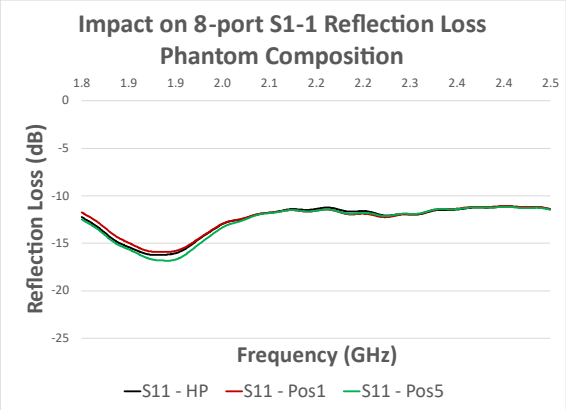

Figure 4-20 – Impact on 8-port phantom composition – S1-1

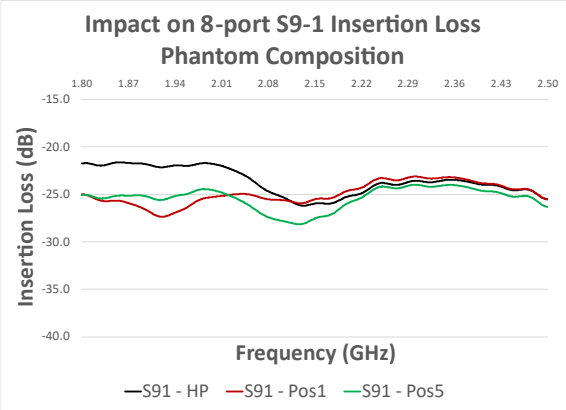

Figure 4-21 – Impact on 8-port phantom composition – S9-1

Finally, a 16-port system was created, and similar testing was performed. Reflection loss measurements were graphed in Figure 4-22, showing a similar response for each phantom configuration. The response for the system has changed, as shown previously in Figure 4-16 where the resonance increases in frequency from 1.95GHz to 2.08GHz. This was as a result of antennas being placed closer together and as well as additional surfaces for the signal to reflect off. Figure 4-22 shows that a healthy phantom and Pos5 lesion provided almost identical loss measurements, while Pos1 lesion has a negligible increase in loss up to 2.1GHz. This suggests that monostatic testing using a fixed 16-port system may provide a low-resolution image as the change in reflection loss with respect to lesion position, was minimal.

Insertion loss testing, graphed in Figure 4-23 shows that the inclusion of additional antennas may be detrimental to the performance of the system. Previously shown in an eight-port system, a noticeable attenuation was seen at 1.92GHz, which for the 16-port system was measured as a null at -35dB. As scatter parameters are graphed logarithmically, the real power variation cannot be clearly shown. By transmitting at 0dBm, equal to 1mW, a received signal for a 16-port system at -34.9dB, equal to 324nW. There was an attenuation of 1.1dB between Pos1 and Pos5, resulting in a 22.5% power

reduction of 73nW. This was compared to an eight-port system, measuring the same frequency at -25.6dB, equal to 2.75μW for Pos5. The attenuation measured on an eight-port system was 34.1% at 935nW.

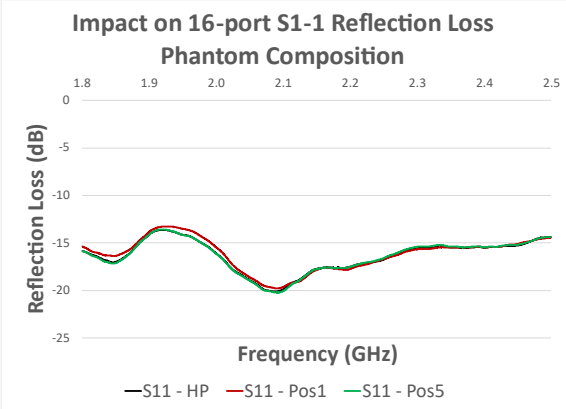

Figure 4-22 – Impact on 16-port phantom composition – S1-1

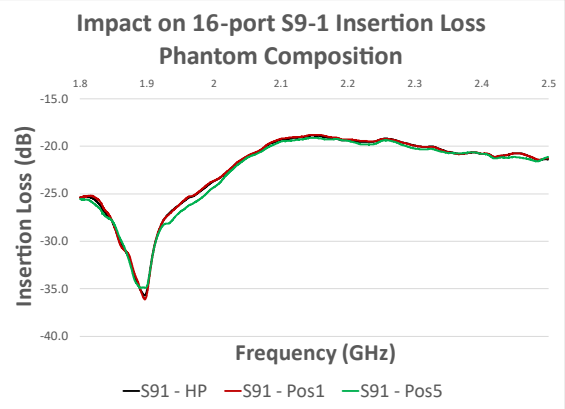

Figure 4-23 – Impact on 16-port phantom composition – S9-1

Full system testing was performed, with each scatter parameter being measured for the reflection coefficients with respect to a 50Ω transmission line, discussed in section 3.3.1. A 16-port system provided a set of 240 insertion loss measurements, ranging from $S_{2\text{-}1}$, and $S_{3\text{-}1}$, up to $S_{14\text{-}16}$ and $S_{15\text{-}16}$. The results of these were then collected into a usable format for image reconstruction.

4.4.4. Multi-Port Investigation Summary

Multi-port experimental investigations were performed by manufacturing sixteen antennas and placing a number of them equally spaced apart, resulting in either four, eight or sixteen sized systems. Initial testing confirmed that manufacturing and user errors caused variation in $S_{x\text{-}x}$ reflection losses between all antennas, which needed to be accounted for during further tests.

Testing was conducted on all system sizes, with no phantom present, to demonstrate if the introduction of additional antennas impacted the individual performance. Additional reflections were

shown to be detrimental in a 16-port system as the $S_{1\text{-}1}$ losses generated resonances at different frequencies, which then impacted $S_{9\text{-}1}$ insertion losses.

Three phantom configurations were then introduced to each system, to determine if a change in lesion position interacted with $S_{1\text{-}1}$ and $S_{9\text{-}1}$ measurements. All configurations showed minimal impact on reflection loss, primarily between 1.80GHz and 2.05GHz, suggesting monostatic testing was not optimal. Four and eight-port systems demonstrated a noticeable impact on insertion loss, by a reduction in measured gain throughout the frequency range, while 16-ports was less affected. An increased system size worsened the performance of each antenna, however, exponentially increased the quantity of potential monostatic and bistatic measurements. Further reconstruction investigations were performed to show if the benefit of additional measurements outweighed the performance degradation.

4.5. EXPERIMENTAL INVESTIGATION SUMMARY

Experimental measurements and simulated testing show an agreement in $S_{x\text{-}x}$ reflection loss and $S_{x\text{-}y}$ insertion loss for several test scenarios. The single-port characterisation was performed by measuring far-field gain using a calibrated horn antenna. Experimental results were comparable to simulate testing, demonstrating that frequencies between 1.80GHz and 2.50GHz provided an end-fire transmission. Reflection loss measurements were performed on sixteen elements, each providing subtly different reflected power levels.

A two-port system was constructed, showing reflections between antennas when placed at an angle of 22.5°, 140mm from the centre of the system which increased resonance at 1.92GHz. A phantom was introduced to the system with three configurations, a healthy homogenous phantom, a phantom with a lesion +30mm from the centre at an angle of 0° being Pos1, and then a phantom with a lesion

at an angle of 90° being Pos5. Insertion loss measurements, recorded as $S_{9\text{-}1}$, show attenuation and amplification of the received signal at various frequencies when comparing the two lesion positions.

Experimental testing was then performed on a fixed position system with an increased quantity of antennas. Results for each system size being tested with all phantom configurations were analysed suggesting between eight and sixteen antennas was the optimum number. Further evaluation during reconstruction was performed to show if this was sufficient for measuring the location and dimension of a lesion.

CHAPTER 5. RECONSTRUCTION

This section describes the established code that has been designed to reconstruct cross-sectional images of a phantom, by using monostatic and bistatic measurements recorded in Chapter 4 [9]. With the introduction of a fixed position system, the MATLAB code required adaptation for this project as fewer antenna measurements were performed, the full export of the code is shown in Appendix 1.

The MATLAB code was written to analyse the effect on field measurements of the centre object to indicate the presence and location of an inclusion. This is done through understanding Huygens' Principle of "e*ach locus of a wave excites the local matter which reradiates a secondary wavelet, and all wavelets superpose to a new, resulting wave*" [52]. As the inclusion possesses a substantially higher dielectric constant to the surrounding material, when the wave front meets the boundary, it reradiates as a new wave front. In this project the object is illuminated by a wave front at a known frequency by the Primary antenna, at a fixed position. The resultant wave is then measured using each of the Secondary antennas, which were placed at equal angular spacing around the centre object. A reference measurement was taken without a centre object, allowing for a vector subtraction to be performed against the test scenario, removing the impact from a wave interacting with each antenna.

Further details on the code can be seen in Appendix 1 and Appendix 2, however, here is brief overview for each portion. Matrices of the test file and the three reference files were imported from a text file containing the real and imaginary coefficients of each antenna pairing at each measured frequency. The test setup is defined for angular steps, environmental dielectric properties of air and the desired frequency range. The code then sequentially steps through and averages each new frequency, for all antenna measurements. The resultant matrix can then generate a density map, showing the contrast between mismatched boundaries, therefore locating the position and size of an inclusion.

Previous work conducted by the group comprised two antennas, with the primary remaining stationary and the secondary being rotated in 4.5° increments through the 360° required [53]. The maximum quantity of antennas in the system discussed in this project was sixteen, with an angular separation of 22.5°. Matrices of insertion loss and reflection loss measurements were generated by measuring all S_{x-y} configurations incrementally. Measurements were recorded for frequencies between 1.00GHz and 3.00GHz at steps of 20MHz, however, only frequencies between 1.80GHz and 2.50GHz were used for reconstruction as this frequency range provided a stable beam direction close to ϕ=0° when viewed at θ = 90°.

The four test scenarios studied were with no phantom present, in Figure 4-8, a homogenous healthy phantom in Figure 4-9, a phantom with lesion at Pos1 in Figure 4-10 and a phantom with lesion at Pos5 in Figure 4-11.Reconstruction image processing was performed to show if experimental measurements reflected what was generated during simulation.

The code used for image reconstruction is seen in Appendix 1 for monostatic and Appendix 2 for bistatic reconstruction. Other than the titles for each file to be loaded into the MATLAB code, the following variables were changed based on the test being performed.

Table 5-1 – Reconstruction variables – four position system

Variable	Description
Er1	This is the dielectric constant of the known homogenous phantom material. It is assumed that the inclusion consists of a material with a higher dielectric constant. This can be set during simulation to be an exact value, however, during experimental testing it is unknown. Values are set between 1 and 4.
Sigma1	This is the conductivity of the known homogenous phantom material. It is assumed that the inclusion consists of a material with a conductivity. This can be set during simulation to be an exact value, however, during experimental testing it is unknown. Values are set between 0 and 0.5.
delta_phi	This describes the positioning steps of the antenna in radians, which is calculated using the number of positions used. Values are set to xx*pi/180, with xx being the angle in degrees.

phi_note_multisource	This is the angular range and step size of the test that was performed, calculated using the number of positions. Values are set to [0:xx:359], with xx being the angle in degrees and the limits being minimum and maximum angles.
multisource_index	This is the quantity of transmit antenna positions. Value is set to either 4, 8 or 16 positions.
Caxis ([ ])	This configures the figure axis to accurately show the desired range of intensity values. Initial measurements have the axis unrestricted to show the peak values for "Healthy", "Pos1 lesion", and "Pos5 lesion". Caxis was then configured so that the intended lesion position was visible and a healthy phantom became a uniform colour. Peak measurements were shown for each image.

Calculations were performed to produce raw intensity plots of the test area, which then allowed for 'caxis' to be adjusted accordingly. In the images, we plot the intensity which was given in arbitrary units (a.u). It follows that images represent qualitative maps of the dielectric contrast.

5.1. RESULT RECONSTRUCTION SETUP

Full system testing was conducted on each of the phantom configurations, shown in Figure 5-1, for both a two-port rotational system and the equivalent fixed position systems. More information on dimensions and materials can be found in section 4.2.1. The purpose of the reconstruction was to supply a yes or no confirmation that a lesion was present rather than giving an exact location. Further discussions provide options for optimisation such as filtering and setting limit values for detection. To appropriately compare rotational and fixed position systems, equivalent measurement quantities were used, with MATLAB variables being constant. See section 4.2.3 for images and explanation on phantom and antenna positions. Similar tests were performed for rotational and fixed position systems, using the same number of measurements.

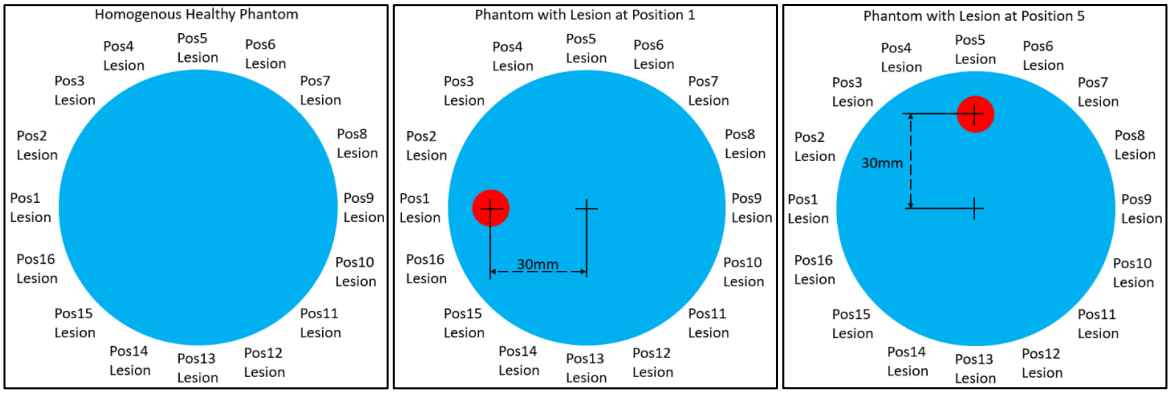

Figure 5-1 – Reconstruction phantom configuration sketch – Healthy, Pos1 and Pos5

For example, a four position, two antenna, test on a healthy phantom was conducted as follows. The healthy phantom was placed in the centre, Port-1 antenna was placed as Pos1 and Port-5 antenna placed at Pos2, resulting in both $S_{5\text{-}1}$ and $S_{1\text{-}5}$ measurements. Port-2 antenna was then removed from Pos5 and placed in Pos9, while Port-1 and the phantom remained stationary, giving in $S_{9\text{-}1}$ and $S_{1\text{-}9}$ measurements. This repeated until all 12 bistatic measurements were collected, similarly to the results generated during simulation. Monostatic measurements were performed with a single antenna being placed in each of the positions, with no other antenna present.

A similar test was then performed using a fixed position system, where four passive antennas were placed at Pos1, Pos5, Pos9 and Pos13, being loaded with 50Ω. The loads were then removed from Pos1 and Pos5 antennas and the antennas connected to the VNA, resulting in $S_{5\text{-}1}$ and $S_{1\text{-}5}$ measurements. The Pos5 antenna was then disconnected, and a load was reconnected. The process was repeated until all 12 bistatic measurements were performed. Each monostatic measurement was taken with the three remaining antennas loaded with 50Ω to limit reflections and reradiation. Each system size for both rotational and fixed position was repeated with all four-phantom configuration.

Reconstruction images were created by performing a vector subtraction with the "No phantom" tests, which removes any discrepancies caused by the antennas themselves. Raw images of each test,

without a vector subtraction, showed almost no difference between each tests, proving this process was necessary.

Further image processing may be performed once an acceptable result is given to provide a clearer image. If multiple simulations or experiments, using the same setup but with different lesion in positions, show similar peak values then a threshold can be used. For example, if the healthy phantom showed a peak of 0.4a.u, while all lesion images showed a value of 0.8a.u, all values below 0.6a.u will revert to 0.0a.u. This then limits false artefacts caused by errors during measurements or setup.

5.2. SYSTEM SIZES WITH UNDETERMINED RESULTS

Reconstruction images created through using the results from simulation and experimentation for a four and eight position system, gave an undeterminable result. The generated images contained "ghost artefacts", giving a false indication of multiple lesions or a lesion in the incorrect place. This is due to having an insufficient number of samples, such as four positions providing only twelve.

It was seen in many of these images would only produce acceptable results if the vector subtraction was performed with a "healthy" phantom. This shows the test was performed correctly, however was discounted as this is not possible in a real-world scenario. Each images was constructed using arbitrary units (a.u) as a result of the MATLAB calculations, which was plotted on an X,Y graph, with higher values suggesting materials with higher dielectric constants.

A simulation was performed using four antennas surrounding the phantom, which was then repeated experimentally. The results of the simulation, as seen in Figure 5-2, show lesions in the correct position and some ghost artefacts. The issue with these results were the limited difference between healthy phantom image giving a peak value of 0.347a.u and Pos1 lesion giving a peak value of

0.388a.u. As a ratio of peak intensity, being 0.388/0.347 giving 1.12, confirms these results are unreliable. The desired limit to confirm a lesion is present is a minimum ratio of 1.5.

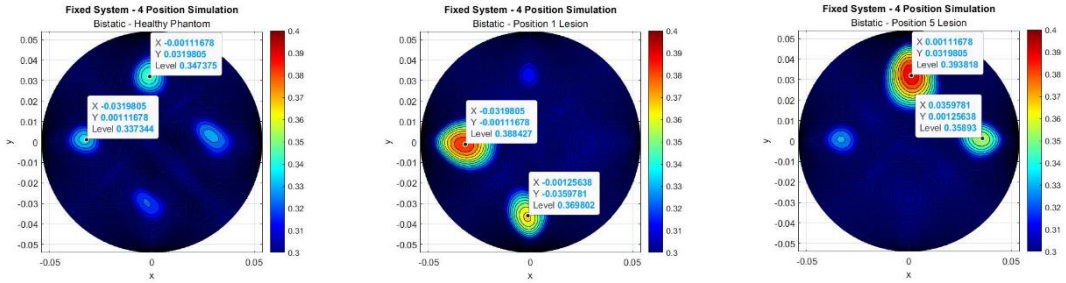

Figure 5-2 – Simulated bistatic results - four fixed elements - healthy phantom, phantom with Pos1 lesion and Pos5 lesion

The same test was performed experimentally with results seen in Figure 5-3, shows a more favourable peak intensity ratio but with an increased number of ghost artefacts. Pos1 lesion measured a peak intensity of 0.434a.u, while healthy phantom measured 0.272a.u, resulting in a ratio of 1.596. Pos5 lesion shows additional lesion positions at 90° from the expected position. The final discrepancy in these tests were the difference between peak intensity of Pos1 and Pos5 images, being 0.434a.u and 0.583a.u respectively, suggesting either user error or antenna differences. It was expected that these values would be almost identical, as it was from the simulated results.

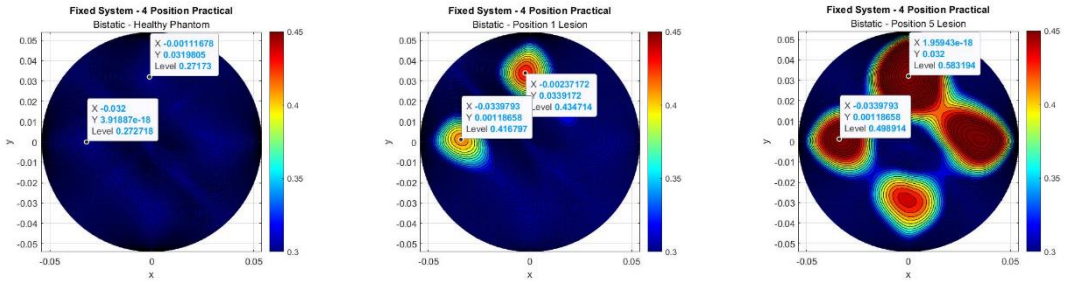

Figure 5-3 – Experimental bistatic results - four fixed elements - healthy phantom, phantom with Pos1 lesion and Pos5 lesion

Monostatic reconstruction for both 4 positions and 8 position, provided poor images with minimal differences in peak values between all phantoms. As seen in Figure 5-4, the peak for healthy was

0.167a.u, Pos1 lesion was 0.191a.u and Pos5 was 0.207a.u. This gives a peak value ratio for Pos1 lesion of 1.144, and Pos5 lesion being 1.239. Neither lesion result gave an indication of a location either.

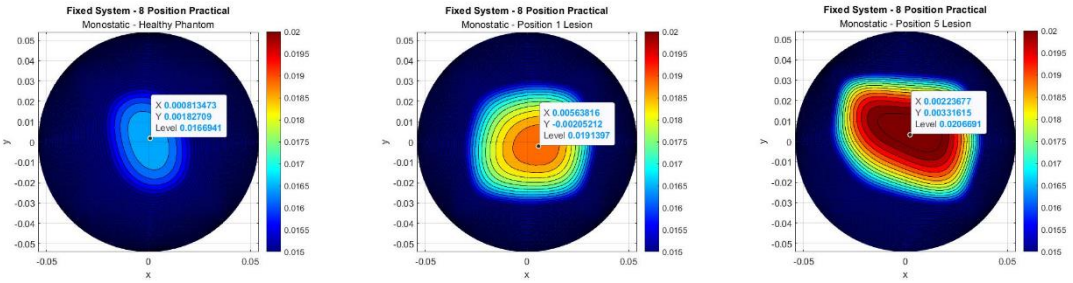

Figure 5-4 – Experimental monostatic results – eight fixed elements - healthy phantom, phantom with Pos1 lesion and Pos5 lesion

5.3. SUCCESSFUL RECONSTRUCTION RESULTS USING SIXTEEN POSITIONS

Using the simulated and measured scatter parameters of a sixteen-position system showed promising results for both bistatic and monostatic calculations. The fixed position systems were focussed on here as earlier research has shown the effectiveness of two port rotational systems. As described previously, the peak values for all three phantom tests were compared to produce a ratio, with a higher value being a better result. A second comparison was then taken for each of the phantoms with a lesion, to show the ratio between peak and additional ghost artefacts. The preferred results is having a single point peak with no additional noise, however, this is not achievable due to measurement uncertainty.

With these two ratio values, further post processing may be performed to give a more clear result. The lesion/healthy ratio sets a lower limit so that a healthy phantom doesn't produce a false reading. The noise ratio then sets a limit to filter out any artefacts that are unlikely to be actual lesions. Further testing is required, with multiple lesions, to confirm that they each produce a similar peak a.u value.

Unlike the previous setups, the 16-position system showed better experimental result using the monostatic calculations than the bistatic calculations. The results of the simulated bistatic testing in Figure 5-5, showed a clear single peak for the location of the lesion. The healthy phantom shows a peak value of 0.0198a.u, while Pos1 being 0.0505a.u and Pos5 being 0.0582a.u. This results in a lesion/healthy ratio of 2.55 for Pos1 and 2.94 for Pos5. For the Pos1 result, a secondary peak was 0.0405, and gives a peak/noise ratio of 1.247. The Pos5 result gave a secondary peak of 0.0219 and a ratio of 2.658. Further investigation is needed to understand why the Pos5 simulation produced more favourable results.

Experimentally, the results were not as clear as all images in Figure 5-6 had an elongated lesion. A healthy phantom produced a higher than predicted peak value, which therefore lowered the lesion/healthy ratio, making the results unreliable. Comparing the positioning of the artefacts shown in the healthy phantom with Pos1 lesion image, indicates an error in measurement. This is caused by other antennas being within the near field range. The full set of bistatic results were used in the reconstruction process, which included adjacent S_{x-y} measurements that were not changed by the lesion. Further work, using only the opposing elements may produce a more accurate result. For example, transmitting from Port-1 at Pos1, using only the measurement received from Port-2 at Pos10 to Pos12. See Table 5-2 for further details on the recorded values for each test.

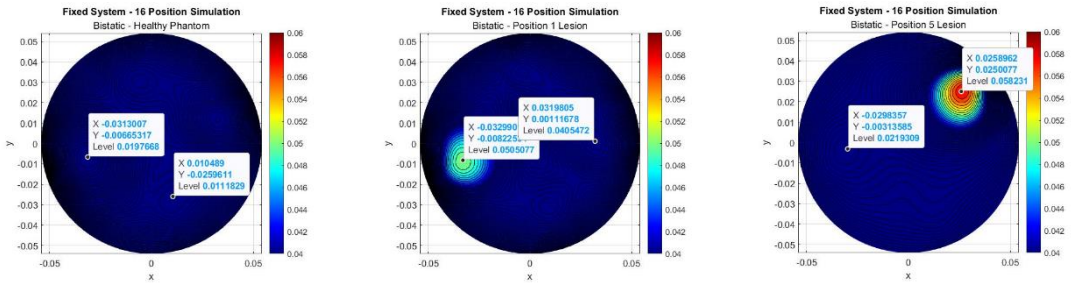

Figure 5-5 – Simulated bistatic results - sixteen fixed elements - healthy phantom, phantom with Pos1 lesion and Pos5 lesion

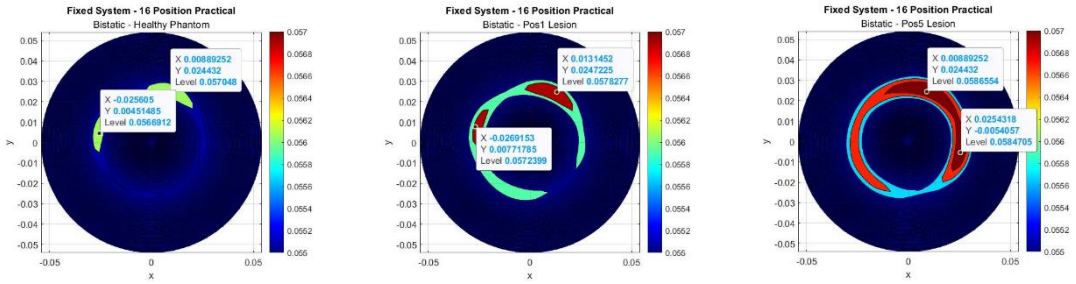

Figure 5-6 – Experimental bistatic results - sixteen fixed elements - healthy phantom, phantom with Pos1 lesion and Pos5 lesion

Fixed monostatic reconstruction imaging on a 16-position system, produced much better results when compared to lower quantity systems. In Figure 5-7, the results of a simulated 16 fixed position monostatic system, gave an excellent lesion/healthy ratio, as well as good peak/noise ratio. The Pos1 image gives a lesion/healthy ratio of 7.234a.u but a peak/noise ratio of only 1.099a.u. The Pos5 image gives a lesion/healthy ratio of 9.721a.u and a marginally better peak/noise ratio of 1.114a.u.

It can be seen in Figure 5-8, that experimental monostatic measurements produced the preferred results in terms of lesion/healthy and peak/noise ratios. However, the size of the suspected lesion is larger than expected, which exaggerated the severity of the lesion. The Pos1 image gives a lesion/healthy ratio of 5.549a.u but a peak/noise ratio of only 1.275a.u. The Pos5 image gives a lesion/healthy ratio of 5.589a.u and a peak/noise ratio of 1.261a.u. Both results produce similar ratios when compared to a healthy phantom, which confirms that a monostatic 16 element system

successfully detects a change in lesion position. Table 5-2 more clearly compares the recorded a.u values for each system.

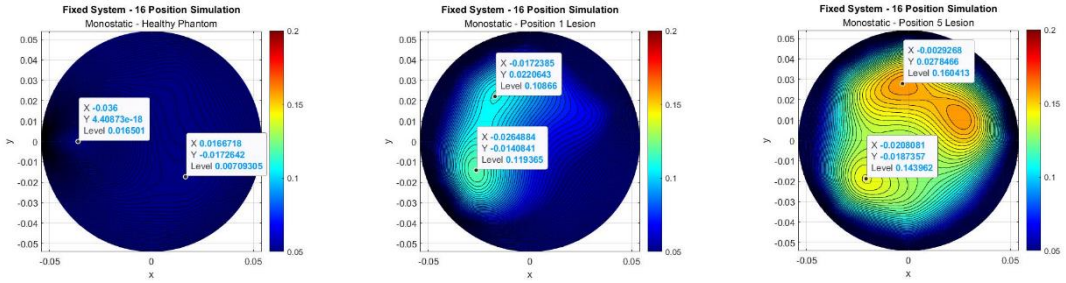

Figure 5-7 – Simulated monostatic results – sixteen fixed elements - healthy phantom, phantom with Pos1 lesion and Pos5 lesion

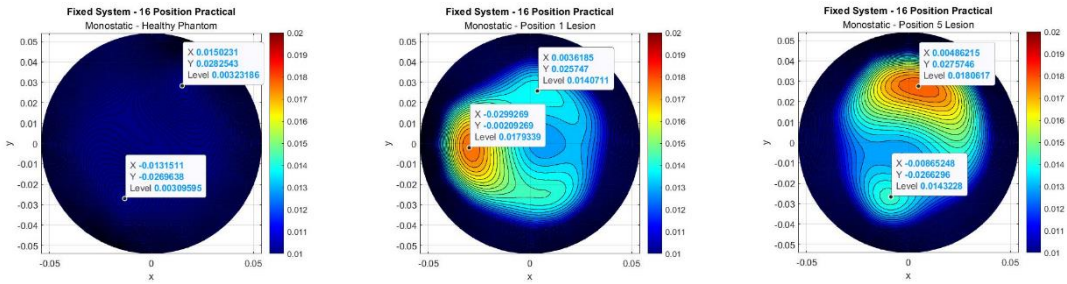

Figure 5-8 – Experimental monostatic results – sixteen fixed elements - healthy phantom, phantom with Pos1 lesion and Pos5 lesion

Table 5-2 – Reconstruction peak values and ratios

Reconstruction setup	Test image	Peak value	Noise Value	Lesion/Healthy ratio	Peak/noise ratio
Simulated bistatic	Healthy phantom	0.0198	0.0112	-	-
	Pos1 lesion	0.0505	0.0405	2.5552	1.2457
	Pos5 lesion	0.0582	0.0219	2.9459	2.6552
Measured bistatic	Healthy phantom	0.0570	0.0567	-	-
	Pos1 lesion	0.0578	0.0572	1.0137	1.0103
	Pos5 lesion	0.0587	0.0585	1.0282	1.0032
Simulated monostatic	Healthy phantom	0.0165	0.0071	-	-
	Pos1 lesion	0.1194	0.1087	7.2338	1.0985
	Pos5 lesion	0.1604	0.1440	9.7214	1.1143
Measured monostatic	Healthy phantom	0.0032	0.0031	-	-
	Pos1 lesion	0.0179	0.0141	5.5491	1.2745
	Pos5 lesion	0.0181	0.0143	5.5886	1.2610

External factors affect testing, such as user error, individual element performance, and repositioning of the phantom, which further testing will improve. For these reasons, sixteen is currently the preferred number of elements in a fixed position system as it produces a clear indication that a lesion is present and accurately suggests a potential location.

5.4. RECONSTRUCTION SUMMARY

Analysis of the reconstructed images provided by the results for several test scenarios concluded that the development of a usable fixed position system was practical. Current research has shown rotational scanning provides a clear indication of the location and dimensions of a lesion [9], [53]. The findings are shown in section 5.1, for two-port rotational scanning, confirm this as they each provide a reasonable indication of the lesion.

Throughout simulation and experimental testing, it was expected that monostatic measurements would provide a lower resolution to bistatic measurements. The results gathered during reconstruction show that was true for a four and eight element system, but not when using sixteen elements.

All of the testing performed used a two-port VNA and consecutively measured the scatter parameters of the elements present. The results compare the use of two antennas being placed in sequential positions to a set of fixed elements that were tested individually. Therefore, the number of measurements remained equal, and the investigation focused on whether further passive elements degraded the results. This presents an opportunity for further development into either an electronic switch to perform sequential testing, or the design of a phased array which may focus the beam direction.

Reconstruction imaging using an increased quantity of elements in a fixed position system showed promising results. All three system sizes produced a noticeable peak increase when a lesion was introduced, confirming it affects the antennas. Further signal processing and an improved test setup will increase the reliability of the system and therefore provide clearer results.

With the image processing techniques used in this project, a common error occurs where 'ghost' artefacts are present. These are commonly presented as added peaks in the phantom image, either at 90° or 180° from the true artefact. This was shown most clearly in Figure 5-3 where there are four potential lesions. Further image processing can reduce this effect and is to be used in further development now that a reconstructed image was possible.

The eight-position system provided the best rotational results, as the fewer artefacts were also at a lower measurement than the true position. The eight-port fixed system has generated lower quality results than expected, as neither of the artefacts was shown in the true location. The testing does confirm a lesion was present, however, analysis by itself cannot be used to determine an exact location.

The rotating sixteen position system produced an acceptable reconstruction, which clearly shows the true location of a lesion. The resolution of each image was reduced because of the intensity discrepancy, however, does confirm the presence and approximate location of the lesion. The most favourable results for a fixed position system were produced using sixteen elements, as the peak artefacts were in the true position. Further investigations are required to determine why a change in lesion position affected the peak intensity.

The findings from this chapter suggest an optimum fixed position size may be between eight and sixteen elements. Further testing is required to improve the system performance and determine an appropriate number of ports and the associated separation angle.

CHAPTER 6. CONCLUSION AND FUTURE IMPROVEMENTS

This report has covered the development of a potential alternative to the current non-intrusive research surrounding lesion detection in phantoms using UHF transmissions from UWB antennas. An investigation was carried out on whether the scatter parameter measurements from a collection of antennas surrounding a phantom were suitable to be reconstructed into a cross-sectional image. Conclusions are divided into four sections, reviewing the research process, evaluation of the design and testing process, summary of results and recommendations for further development.

In Chapter 2, an examination of recent research gave a baseline understanding of successful systems capable of reconstructing phantom images. A discussion focussing on the right antenna designs paved the way for achieving the successful designs used in this project.

6.1. EVALUATION OF THE DESIGN AND TEST PROCESS

6.1.1. Evaluation of the Simulation Process

In Chapter 3, a preliminary Model-A design was produced through understanding best practices from established similar antennas, and progressive modifications for fine-tuning. Successful characterisation of the antenna confirmed the UWB antenna transmits at an end-fire beam angle of ±4° between the frequencies 1.80GHz and 2.50GHz with a beam width less than 80°.

Simulations between two antennas demonstrated reduced reflections after an angular separation of 30° from a centre-point at 140mm, as $S_{1\text{-}1}$ was less affected. The introduction of a phantom and lesion, with both antennas remaining stationary, caused attenuation and amplification of both reflection and insertion losses. Far-field measurements at ±25° from the antenna showed a noticeable gain increase of 1.606dB towards the lesion when placed perpendicular to the antenna. This result indicated that,

if used in a calibrated system, antennas on one side would measure a higher power than their counterpart and suggests the presence of a lesion.

Fixed position simulations were performed consisting of several elements equally spaced around the phantom. S-parameter simulations showed that a 16-port system produced substantial resonances while a four-port and eight-port system decreased in measured power but remained stable. Further nulls were seen during far-field measurements as the number of antennas was increased, with the 16-port system producing a more concentrated beam towards the phantom.

A similar effect occurred with the placement of a lesion to what was seen in a two-port system, where the far-field beam was coupling to the lesion, resulting in one antenna measuring a higher power than its opposite. Simulations using a 16-port system produced irregular and possibly unreliable results, as the reflection losses were affected substantially more than either a four-port or eight-port system. Further simulations may be required to confirm the results. The results of this section gave the project confidence to progress with experimental work by manufacturing and testing antennas practically. The antenna was modified to allow structural rigidity during experimental testing, with the creation of a holding fixture. Testing on both antennas demonstrated minimal impact on performance.

6.1.2. Evaluation of the Experimental Process

In Chapter 4, experimental testing occurred after 16-elements were constructed and tested, where discrepancies were seen during reflection loss measurements. An improved manufacturing process will result in more reliable performances and therefore better system results. Far-field gain measurements were recorded using a calibrated horn antenna, confirming similar responses to those seen during simulation. Frequencies below 1.80GHz showed an acceptable beam width below 80°, however, the beam angle drifted away from the centreline and resulted in an undesirable response. Further improvements to the design can focus these frequencies by potentially including a parasitic

patch, to further increase the usable bandwidth. Practical reflection loss measurements had similar performance to simulated results, however, minor resonances occurred which can be attributed to several measurement errors.

Rotational testing was limited to an angular spacing of 22.5°, due to the holding fixture construction, where reflections between adjacent placements occurred and reinforces the findings during simulation. The introduction of a phantom with lesion resulted in $S_{1\text{-}1}$ and $S_{2\text{-}1}$ measurements being impacted, similarly to what was seen during simulation. Experimental insertion loss testing showed a larger change, in terms of a received power, when the lesion was moved than an antennas reflection loss for frequencies above 2.00GHz.

Fixed position testing was conducted for four-port, eight-port and 16-port systems, where an eight-port system was seen to be the most responsive. Reflection loss measurements for all systems remained stable, regardless of phantom composition, on all systems which further suggests a monostatic approach was inferior. The eight-port system, comparing Pos5 and Pos1 lesions, demonstrated a noticeable gain increase for $S_{2\text{-}1}$ up to 2.00GHz and then attenuation up to 2.21GHz where it became stable. Further analysis of insertion losses between antennas having an angle over ±90° was impacted by a change in the lesion and suggested a bistatic system would produce a favourable result.

6.2. SUMMARY OF THE RESULTS

Chapter 5 discussed the potential image reconstruction of a phantom, using the reflection and insertion loss characteristics of several system configurations. The results were promising, showing a clear peak power increase after introducing a lesion, suggesting the location can be determined. The rotational system provided clearer results than a fixed position system, which was due to a

reduced reflections off adjacent antennas. These findings are in line with the previous research performed by the group, suggesting the results are valid but need improvement.

The fixed position systems showed that the presence of a lesion was easily detectable; however, the exact positioning was difficult to define. Sixteen fixed position elements produced the best outcome, where the artefact approximated the true position of the lesion.

Section 6.3 discusses further improvements to the system, which will result in more accurate reconstruction imaging.

6.3. RECOMMENDATION FOR FURTHER DEVELOPMENT

Now that the proposed solution has been investigated and has confirmed that a fixed position system is a suitable alternative for RF imaging systems, further improvements can be applied. These improvements are split into three sections, improvements to the antenna design, holding fixture, simultaneous signal processing of array elements and experimental testing. These improvements will make the device a commercially valuable tool for medical analysis, combined with other established methods to achieve rapid results. The project development is worth perusing to develop into a fully functioning product, providing first responders with more information to select the most appropriate course of action. This in turn will save medical resources if no fracture is suspected, whereas previously an X-ray will be required.

Several aspects of the antenna design can be changed to either improve the functionality of the antenna itself or the system as a whole. A reduction from half-wave calculations to quarter-wave calculations is capable of largely increasing the number of elements within the system, and therefore allows for a higher number of samples. The dielectric material is limited, however only FR-4 was fully investigated, further design and simulations into other options may improve performance. An

improved alternative to the AVA design utilises a secondary ground plane, which may be produced through another section of single-sided FR-4 to create a Balanced AVA. Further investigations are required into improving the beam direction for lower frequencies from 1.50GHz to 1.80GHz, such as a parasitic patch or adaptations to the aperture.

The holding fixture and assembly of the system can be developed for a more repeatable testing process. A more robust design with either physical or sensory distance gauges towards the phantom will ensure positioning is correct each time. An investigation into limiting the system to using half of the fixture, Pos1 to Pos9, may indicate that the full perimeter is not necessary. In doing so, a handheld device can be constructed which does not need to be wrapped around the area under investigation, which further increases the product's use case. The current design has investigated a phantom with a diameter of 110mm, a preferred design improvement would be to have a device capable of easily adjusting its diameter to suit a range of phantoms. An investigation into interlaced rigid RAM panels may improve performance by reflections between antennas.

The testing in this project focused on the comparison between a two-port, rotational system and an equivalent fixed position, multiple port system. Previous research rotated a receiver antenna, sequentially measured the scatter parameters and superimposed the results. By introducing a number of additional elements in fixed positions, either cable connected to the VNA could be removed and reconnected to another antenna. This allows for a system where the antennas and phantoms remain stationary, along with regular performance for each antenna, as the angular shift remains equal.

This research opens the door to further development into either electronically switched sequential testing, or discussions into a phased array. An electronically switched system will be the preferred next step, through the use of an RF switch to sequentially transmit and receive elements. By doing so, the risk of human error is reduced, as well as vastly decreasing the time taken to perform a scan.

By allowing all antennas to be fixed in position after a single cable fitment, the reference scan will be more reliable as the only disturbance will be positioning the phantom.

An improvement that may be incorporated into the system is the use of a smaller RF switch. The expectation early on in the project was to use a 16-port switch so that the maximum number of elements that were simulated, could electronically switched sequentially. A cost-effective alternative would be to use a combination of four-port and two-port RF switches, which are readily available. This would then allow for the 4-position fixed system to be electronically switch rather than manually repositioned. A four-port switch, attached to Port1 on the VNA, would be connected to the primary port on each dedicated two-port switch that all elements have. The same would have been done with Port2 on the VNA, to the secondary ports for each element. This allows all elements to be either a transmit or receive antenna.

A more advanced development to the project would be to allow a number of antennas to transmit the same frequency. By doing so, each beam interacts with each other and causes narrowing of the main beam, which can be guided using a phase offset. This can therefore be used to direct the peak power at a specific point in the phantom and scan linearly across to generate more readings. As the antennas are regularly spaced throughout, a homogenous phantom should theoretically produce equal measurements for all scans.

Experimental testing proved to be difficult through manual disassembly of the system, which produced measurement discrepancies. The introduction of a 16:2 RF switch will drastically decrease testing times and user error as the system can be constructed once, calibrated, and then have the phantom introduced. Further structural development should be performed to allow far-field measurements on a full system rather than limiting to a single antenna. More stringent testing is needed and can be performed by using several phantoms with differing dimensions, materials, and

lesion positions. Further work into data analysis, working within the research group, may develop a solution for real-time measurements.

6.4. CONCLUDING WORDS

The purpose of this project was to investigate if an increased number of electronic elements could replace the current two-port rotational systems with the sequential move towards array element testing. Simulation and experimentation demonstrated the introduction of a homogenous phantom, as well as a phantom with a lesion, affected the S_{x-x} reflection loss and S_{x-y} insertion loss measurements for each antenna. Depending on the proximity to the lesion, each antenna was affected to a varying extent, suggesting that image reconstruction was possible.

These systems successfully reconstructed cross-sectional images of phantoms with lesions, mimicking the properties of a fractured bone. The positive results from both simulation and experimentation testing confirmed the functionality of each system, with the preferred quantity of elements that were assessed being sixteen. Further development will determine the optimum number of elements.

REFERENCES

[1] G. Ruvio, A. Cuccaro, R. Solimene, A. Brancaccio, B. Basile, and M. J. Ammann, "Microwave bone imaging: a preliminary scanning system for proof-of-concept," *Healthc. Technol. Lett.*, vol. 3, no. 3, pp. 218–221, Jun. 2016, doi: 10.1049/htl.2016.0003.

[2] K. C. Santos, Carlos. A. Fernandes, and J. R. Costa, "A study on the sensitivity of microwave imaging for detecting small-width bone fractures," in *2021 15th European Conference on Antennas and Propagation (EuCAP)*, Mar. 2021, pp. 1–4. doi: 10.23919/EuCAP51087.2021.9411065.

[3] H. Bahramiabarghouei, E. Porter, A. Santorelli, B. Gosselin, M. Popović, and L. A. Rusch, "Flexible 16 Antenna Array for Microwave Breast Cancer Detection," *IEEE Trans. Biomed. Eng.*, vol. 62, no. 10, pp. 2516–2525, Oct. 2015, doi: 10.1109/TBME.2015.2434956.

[4] N. Ghavami, G. Tiberi, D. J. Edwards, and A. Monorchio, "UWB Microwave Imaging of Objects With Canonical Shape," *IEEE Trans. Antennas Propag.*, vol. 60, no. 1, pp. 231–239, Jan. 2012, doi: 10.1109/TAP.2011.2167905.

[5] H. M. Jafari, M. J. Deen, S. Hranilovic, and N. K. Nikolova, "A Study of Ultrawideband Antennas for Near-Field Imaging," *IEEE Trans. Antennas Propag.*, vol. 55, no. 4, pp. 1184–1188, Apr. 2007, doi: 10.1109/TAP.2007.893405.

[6] B. T. Cetin and L. Alatan, "Performance comparison of different sparse array configurations for ultra-wideband, near-field imaging applications," in *2017 11th European Conference on Antennas and Propagation (EUCAP)*, Mar. 2017, pp. 458–460. doi: 10.23919/EuCAP.2017.7928802.

[7] B. Khalesi, B. Sohani, N. Ghavami, M. Ghavami, S. Dudley, and G. Tiberi, "A Phantom Investigation to Quantify Huygens Principle Based Microwave Imaging for Bone Lesion Detection," *Electronics*, vol. 8, no. 12, p. 1505, Dec. 2019, doi: 10.3390/electronics8121505.

[8] R. Augustine, D. G. Kurup, S. Raman, D. Lee, K. Kim, and A. Rydberg, "Bone mineral density analysis using ultra wideband microwave measurements," in *2015 IEEE MTT-S International Microwave and RF Conference (IMaRC)*, Dec. 2015, pp. 102–104. doi: 10.1109/IMaRC.2015.7411399.

[9] G. Tiberi, B. Khalesi, B. Sohani, S. Dudley, M. Ghavami, and N. Ghavami, "Phase-weighted UWB Imaging through Huygens Principle," in *2019 PhotonIcs Electromagnetics Research Symposium - Spring (PIERS-Spring)*, Jun. 2019, pp. 949–952. doi: 10.1109/PIERS-Spring46901.2019.9017794.

[10] G. Dougherty, "Medical imaging — An illustrated overview," in *2009 24th International Conference Image and Vision Computing New Zealand*, Nov. 2009, pp. 171–178. doi: 10.1109/IVCNZ.2009.5378416.

[11] J. A. Seibert, "X-ray imaging physics for nuclear medicine technologists. Part 1: Basic principles of x-ray production," *J. Nucl. Med. Technol.*, vol. 32, no. 3, pp. 139–147, Sep. 2004.

[12] J. Hsieh, *Computed Tomography: Principles, Design, Artifacts, and Recent Advances*. SPIE Press, 2003.

[13] J. B. Little, "Radiation carcinogenesis," *Carcinogenesis*, vol. 21, no. 3, pp. 397–404, Mar. 2000, doi: 10.1093/carcin/21.3.397.

[14] E. Van Reeth, I. W. K. Tham, C. H. Tan, and C. L. Poh, "Super-resolution in magnetic resonance imaging: A review," *Concepts Magn. Reson. Part A*, vol. 40A, no. 6, pp. 306–325, 2012, doi: 10.1002/cmr.a.21249.

[15] A. Berger, "Magnetic resonance imaging," *BMJ*, vol. 324, no. 7328, p. 35, Jan. 2002.

[16] "basic MR imaging." http://www.med.harvard.edu/aanlib/basicsMR.html (accessed Mar. 13, 2022).

[17] "MRI Machine Price Guide." https://info.blockimaging.com/bid/92623/mri-machine-cost-and-price-guide (accessed Mar. 13, 2022).

[18] "Claustrophobia and MRI," *UCSF Radiology*, May 29, 2013. https://radiology.ucsf.edu/patient-care/prepare/claustrophobia-mri (accessed Mar. 13, 2022).

[19] A. Carovac, F. Smajlovic, and D. Junuzovic, "Application of Ultrasound in Medicine," *Acta Inform. Medica*, vol. 19, no. 3, pp. 168–171, Sep. 2011, doi: 10.5455/aim.2011.19.168-171.

[20] F. A. Duck, "Hazards, risks and safety of diagnostic ultrasound," *Med. Eng. Phys.*, vol. 30, no. 10, pp. 1338–1348, Dec. 2008, doi: 10.1016/j.medengphy.2008.06.002.

[21] V. S. Ramalingam, M. Kanagasabai, and E. F. Sundarsingh, "A Compact Microwave Device for Fracture Diagnosis of the Human Tibia," *IEEE Trans. Compon. Packag. Manuf. Technol.*, vol. 9, no. 4, pp. 661–668, Apr. 2019, doi: 10.1109/TCPMT.2019.2893367.

[22] G. Tiberi, N. Ghavami, D. J. Edwards, and A. Monorchio, "Ultrawideband microwave imaging of cylindrical objects with inclusions," *IET Microw. Antennas Amp Propag.*, vol. 5, no. 12, pp. 1440–1446, Sep. 2011, doi: 10.1049/iet-map.2011.0033.

[23] "VSWR." https://www.antenna-theory.com/definitions/vswr.php (accessed Mar. 13, 2022).

[24] D. M. Hailu and S. Safavi-Naeini, “Narrow focus ultra-wideband antenna for breast cancer detection,” in *2009 IEEE Radio and Wireless Symposium*, Jan. 2009, pp. 437–440. doi: 10.1109/RWS.2009.4957377.

[25] G. Tiberi, N. Ghavami, D. Edwards, and A. Monorchio, “UWB body area network channel modeling: An analytical approach,” *AEU - Int. J. Electron. Commun.*, vol. 66, pp. 913–919, Nov. 2012, doi: 10.1016/j.aeue.2012.03.014.

[26] A. I. Afifi and A. B. Abdel-Rahman, “Ring resonator for breast cancer and broken bones detection,” in *2016 Asia-Pacific Microwave Conference (APMC)*, Dec. 2016, pp. 1–4. doi: 10.1109/APMC.2016.7931292.

[27] M. Lodro, *Antennas and Wave Propagation*. 2016.

[28] A. S. Dixit and S. Kumar, “A Survey of Performance Enhancement Techniques of Antipodal Vivaldi Antenna,” *IEEE Access*, vol. 8, pp. 45774–45796, 2020, doi: 10.1109/ACCESS.2020.2977167.

[29] A. Yaghjian, “An overview of near-field antenna measurements,” *IEEE Trans. Antennas Propag.*, vol. 34, no. 1, pp. 30–45, Jan. 1986, doi: 10.1109/TAP.1986.1143727.

[30] “Antenna Near Field & Far Field Distance Calculator | Southwest Antennas - High Performance RF and Microwave Antennas & Custom Antenna Manufacturing.” https://www.southwestantennas.com/calculator/antenna-near-field-far-field-distance (accessed Apr. 09, 2022).

[31] T. Dlugosz and H. Trzaska, “How to Measure in the Near Field and in the Far Field,” *Commun. Netw.*, vol. 02, no. 01, pp. 65–68, 2010, doi: 10.4236/cn.2010.21010.

[32] Nurhayati, E. Setijadi, and G. Hendrantoro, "Comparison study of S-Band Vivaldi-based antennas," in *2016 IEEE Region 10 Symposium (TENSYMP)*, May 2016, pp. 188–193. doi: 10.1109/TENCONSpring.2016.7519402.

[33] J. Schneider, M. Mrnka, J. Gamec, M. Gamcova, and Z. Raida, "Vivaldi Antenna for RF Energy Harvesting," *Radioengineering*, vol. 25, no. 4, pp. 666–671, Sep. 2016, doi: 10.13164/re.2016.0666.

[34] M. Dvorsky, H. S. Ganesh, and S. S. Prabhu, "Design and Validation of an Antipodal Vivaldi Antenna with Additional Slots," *Int. J. Antennas Propag.*, vol. 2019, p. e7472186, May 2019, doi: 10.1155/2019/7472186.

[35] I. T. Nassar and T. M. Weller, "A Novel Method for Improving Antipodal Vivaldi Antenna Performance," *IEEE Trans. Antennas Propag.*, vol. 63, no. 7, pp. 3321–3324, Jul. 2015, doi: 10.1109/TAP.2015.2429749.

[36] J. Bang, J. Lee, and J. Choi, "Design of a Wideband Antipodal Vivaldi Antenna with an Asymmetric Parasitic Patch," *J. Electromagn. Eng. Sci.*, vol. 18, no. 1, pp. 29–34, Jan. 2018, doi: 10.26866/jees.2018.18.1.29.

[37] P. L. Carro and J. de Mingo, "Electromagnetic Bandgap Microstrip to Parallel-strip Balun in Ultrawideband Applications," in *2008 38th European Microwave Conference*, Oct. 2008, pp. 1137–1140. doi: 10.1109/EUMC.2008.4751659.

[38] M. Riaz, G. Tiberi, H. Asani, M. Ghavami, and S. Dudley, "A Non-Invasive Bone Fracture Monitoring Analysis using an UHF Antenna," in *2020 12th International Symposium on Communication Systems, Networks and Digital Signal Processing (CSNDSP)*, Porto, Portugal, Jul. 2020, pp. 1–5. doi: 10.1109/CSNDSP49049.2020.9249570.

[39] J. Bang, J. Lee, and J. Choi, "Design of a Wideband Antipodal Vivaldi Antenna with an Asymmetric Parasitic Patch," *J. Electromagn. Eng. Sci.*, vol. 18, pp. 29–34, Jan. 2018, doi: 10.26866/jees.2018.18.1.29.

[40] "Microstrip Width Calculator." https://www.everythingrf.com/rf-calculators/microstrip-width-calculator (accessed Mar. 13, 2022).

[41] "Transmission Lines." https://www.antenna-theory.com/tutorial/txline/transmissionline.php#txline (accessed Mar. 13, 2022).

[42] T. Peter, T. A. Rahman, S. W. Cheung, R. Nilavalan, H. F. Abutarboush, and A. Vilches, "A Novel Transparent UWB Antenna for Photovoltaic Solar Panel Integration and RF Energy Harvesting," *IEEE Trans. Antennas Propag.*, vol. 62, no. 4, pp. 1844–1853, Apr. 2014, doi: 10.1109/TAP.2014.2298044.

[43] Z. Li, X. Kang, J. Su, Q. Guo, Y. (Lamar) Yang, and J. Wang, "A Wideband End-Fire Conformal Vivaldi Antenna Array Mounted on a Dielectric Cone," *Int. J. Antennas Propag.*, vol. 2016, p. e9812642, Aug. 2016, doi: 10.1155/2016/9812642.

[44] C. Gabriel, S. Gabriel, and E. Corthout, "The dielectric properties of biological tissues: I. Literature survey," *Phys. Med. Biol.*, vol. 41, no. 11, pp. 2231–2249, Nov. 1996, doi: 10.1088/0031-9155/41/11/001.

[45] A. Santorelli *et al.*, "Investigation of Anemia and the Dielectric Properties of Human Blood at Microwave Frequencies," *IEEE Access*, vol. 6, pp. 56885–56892, 2018, doi: 10.1109/ACCESS.2018.2873447.

[46] C. A. Balanis, *Antenna Theory: Analysis and Design*. John Wiley & Sons, 2016.

[47] D. Lynch and D. D. Lynch, *Introduction to RF Stealth*. SciTech, 2004.

[48] P. Veselý, E. Horynová, T. Tichý, and O. Šefl, "Study of electrical properties of 3D printed objects," p. 5, 2018.

[49] "S5065 2-Port 6.5 GHz Analyzer," *Copper Mountain Technologies*. https://coppermountaintech.com/vna/s5065-2-port-6-5-ghz-analyzer/ (accessed Apr. 29, 2022).

[50] P. Marin, D. Cortina, and A. Hernando, "Electromagnetic Wave Absorbing Material Based on Magnetic Microwires," *IEEE Trans. Magn.*, vol. 44, no. 11, pp. 3934–3937, Nov. 2008, doi: 10.1109/TMAG.2008.2002472.

[51] "3117 Double-Ridged Guide Antenna - ETS-Lindgren." https://www.ets-lindgren.com/products/antennas/double-ridged-guide/4002/400205?page=Products-Item-Page (accessed Apr. 29, 2022).

[52] "(PDF) Huygens' Principle as Universal Model of Propagation." https://www.researchgate.net/publication/41847165_Huygens%27_Principle_as_Universal_Model_of_Propagation (accessed Oct. 02, 2022).

[53] B. Khalid, B. Khalesi, N. Ghavami, S. Dudley, M. Ghavami, and G. Tiberi, "3D Microwave Imaging Using Huygens Principle: A Phantom-based Validation," in *2021 Photonics Electromagnetics Research Symposium (PIERS)*, Nov. 2021, pp. 2892–2896. doi: 10.1109/PIERS53385.2021.9695090.

APPENDIX 1. MONOSTATIC RECONSTRUCTION TEMPLATE

```
%-----------------------------------------------------------------------------------------------------------
% Practical_Fixed_Healthy_16Positions_Monostatic.txt
% Practical_Fixed_NoPhan_16Positions_Monostatic.txt
% Practical_Fixed_Pos1_16Positions_Monostatic.txt
% Practical_Fixed_Pos5_16Positions_Monostatic.txt
%-----------------------------------------------------------------------------------------------------------
%Test File
	clear all
	matrix1 = load('_Monostatic_Files/Practical_Fixed_Pos1_16Positions_Monostatic.txt');
	aa1 = matrix1(:, 1:2:end);
	bb1 = - matrix1(:, 2:2:end);
	matrixComplex1(:,:) = complex(aa1, bb1);
%-----------------------------------------------------------------------------------------------------------
%Uncalibrated test
	% matrix2 = load('_Monostatic_Files/Practical_Fixed_NoPhan_16Positions_Monostatic.txt');
	% aa2 = matrix2(:, 1:2:end);
	% bb2 = - matrix2(:, 2:2:end);
	% matrixComplex2(:,:) = complex(aa2, bb2)*0;
```

```
        % matrixComplex=matrixComplex1-matrixComplex2;
%Healthy Phantom Calibration
        % matrix2 = load('_Monostatic_Files/Practical_Fixed_Healthy_16Positions_Monostatic.txt');
        % aa2 = matrix2(:, 1:2:end);
        % bb2 = - matrix2(:, 2:2:end);
        % matrixComplex2(:,:) = complex(aa2, bb2)*1;
        % matrixComplex=matrixComplex1-matrixComplex2;
% No Phantom Calibration
        matrix2 = load('_Monostatic_Files/Practical_Fixed_NoPhan_16Positions_Monostatic.txt');
        aa2 = matrix2(:, 1:2:end);
        bb2 = - matrix2(:, 2:2:end);
        matrixComplex2(:,:) = complex(aa2, bb2)*1;
        matrixComplex=matrixComplex1-matrixComplex2;
%-------------------------------------------------------------------------------------------------------------
%Phantom / Test Setup
        er1=1;
        ur1=1;
        sigma1=0.4;
        raggio0=0.055;
```

```
        delta_phi=22.5*pi/180;   % phi step
        phi_oss=[0:delta_phi:2*pi-delta_phi] ;
        rho_oss=raggio0*ones(1,length(phi_oss))*1.0;
% grid where we want to reconstruct the  internal field
        delta_phi_reconstr=pi/90;
        delta_rho_reconstr=0.0005*4;
        [phi_oss_reconstr,rho_oss_reconstr]= meshgrid(0:delta_phi_reconstr:2*pi, 0:delta_rho_reconstr:rho_oss);
        NP_rho=size(phi_oss_reconstr,1)
        NP_phi=size(phi_oss_reconstr,2)
% free-space
        u0=4*pi*10^(-7);
        e0=1/(36*pi)*10^-9;
        Z0=120*pi;
        c0=300000000;
% frequency
        f_min=1.8*10^9
        f_max=2.5*10^9
        df_new=7*10^5;  % frequency step
        new_ff=[f_min:df_new:f_max]';
```

```
NF=length(new_ff);
BB=df_new*NF;
phi_note_MULTISOURCE=[00:45:359]./180*pi % phi coordinate of line source
[X_reconstr,Y_reconstr] = pol2cart(phi_oss_reconstr,rho_oss_reconstr);

simulated_reconstr_HuygensG_diff_OLD=zeros(NP_rho,NP_phi,length(new_ff))*5;
simulated_reconstr_HuygensG_diff_NEW=zeros(NP_rho,NP_phi,length(new_ff))*5;
newindex=1
COEFF_NORM=1/(2*pi*raggio0)*df_new/(df_new*NF)*1/length(phi_note_MULTISOURCE);
%-------------------------------------------------------------------------------------------------------
% NOTE: here i'm using avg subtraction artefact removal
mmm=mean(matrixComplex,1);
for multisource_index=1:8
    phi_note=phi_note_MULTISOURCE(multisource_index)
    phi_oss=-[phi_note:delta_phi:2*pi+phi_note] ;
    for i=1:10:1001
        f=new_ff(i);
        e1=er1*e0*(1-j*sigma1/(2*pi*f*er1*e0));
        u1=ur1*u0;
```

```
            k1=sqrt((2*pi*f)^2*u1*e1);
            Z1=sqrt(u1/e1);
            lambda1=2*pi./real(k1);
            pen_depth=-1./imag(k1)
            for np=1:7
                d1=sqrt(rho_oss_reconstr.^2+rho_oss(np).^2-2*rho_oss_reconstr.*rho_oss(np).*cos(phi_oss_reconstr-
                phi_oss(np)+delta_phi*(np)));
            %(k1)
                simulated_reconstr_HuygensG_diff_OLD(:,:,newindex)=simulated_reconstr_HuygensG_diff_OLD(:,:,newindex)+COEFF_NORM
                *delta_phi*raggio0*(k1)/(2*pi*f*e1)*(matrixComplex(np+(multisource_index-1)*7,i)-  mmm(1,i))*exp(-1i*(k1)*(d1)).*exp(-
                imag(k1)*sqrt(rho_oss(np).^2-rho_oss_reconstr.^2));
            %real(k1)
                simulated_reconstr_HuygensG_diff_NEW(:,:,newindex)=simulated_reconstr_HuygensG_diff_NEW(:,:,newindex)+COEFF_NOR
                M*delta_phi*raggio0*real(k1)/(2*pi*f*real(e1))*(matrixComplex(np+(multisource_index-1)*7,i)-  mmm(1,i))*exp(-
                1i*real(k1)*(d1)); %NOTE: here I removed the last part with the aim of checking what happens if we fullfill monostatic theory
            end
            newindex=newindex+1;
            i
        end
end
```

```
MAG_uwb_scatt_incoh_reconstr_diff_OLD=zeros(NP_rho,NP_phi);
MAG_uwb_scatt_incoh_reconstr_diff_NEW=zeros(NP_rho,NP_phi);
new_ff
MAG_uwb_scatt_incoh_reconstr_diff=zeros(NP_rho,NP_phi);
new_ff
for i=1:length(new_ff)*1
    MAG_uwb_scatt_incoh_reconstr_diff_OLD(:,:)=MAG_uwb_scatt_incoh_reconstr_diff_OLD(:,:)+abs(simulated_reconstr_HuygensG_diff_OLD(:,:,i)).^1;
    MAG_uwb_scatt_incoh_reconstr_diff_NEW(:,:)=MAG_uwb_scatt_incoh_reconstr_diff_NEW(:,:)+abs(simulated_reconstr_HuygensG_diff_NEW(:,:,i)).^1;
end
totalIntesita_MAG=0;
for m=1:size(rho_oss_reconstr,1)
    for n=1:size(phi_oss_reconstr,2)
        totalIntesita_MAG=totalIntesita_MAG+MAG_uwb_scatt_incoh_reconstr_diff_OLD(m,n)*delta_phi_reconstr*delta_rho_reconstr*rho_oss_reconstr(m,n);
    end
end
mediaIntesita_MAG=totalIntesita_MAG/(pi*raggio0^2);
%-----------------------------------------------------------------------------------------------------------------------
```

```
figure
contourf(X_reconstr,Y_reconstr,(MAG_uwb_scatt_incoh_reconstr_diff_OLD).^1,50), colormap(jet), caxis([0.1 0.11])
xlabel('x')
ylabel('y')
title('Fixed System - 8 Position Practical', 'Monostatic - Healthy Phantom')
axis square
colorbar
grid
```

APPENDIX 2. BISTATIC RECONSTRUCTION TEMPLATE

```
%-------------------------------------------------------------------------------------------------------------------------
% Practical_Fixed_Healthy_16Positions_Bistatic.txt
% Practical_Fixed_NoPhan_16Positions_Bistatic.txt
% Practical_Fixed_Pos1_16Positions_Bistatic.txt
% Practical_Fixed_Pos5_16Positions_Bistatic.txt
%-------------------------------------------------------------------------------------------------------------------------
%Test File
        clear all
        matrix1 = load('_Bistatic_Files/Practical_Fixed_Pos5_16Positions_Bistatic.txt');
```

```
        aa1 = matrix1(:, 1:2:end);
        bb1 = - matrix1(:, 2:2:end);
        matrixComplex1(:,:) = complex(aa1, bb1);
%-------------------------------------------------------------------------------------------------------------------------
%Uncalibrated test
        % matrix2 = load('_Bistatic_Files/Practical_Fixed_NoPhan_16Positions_Bistatic.txt');
        % aa2 = matrix2(:, 1:2:end);
        % bb2 = - matrix2(:, 2:2:end);
        % matrixComplex2(:,:) = complex(aa2, bb2)*0;
        % matrixComplex=matrixComplex1-matrixComplex2;
%Healthy Phantom Calibration
        % matrix2 = load('_Bistatic_Files/Practical_Fixed_Healthy_16Positions_Bistatic.txt');
        % aa2 = matrix2(:, 1:2:end);
        % bb2 = - matrix2(:, 2:2:end);
        % matrixComplex2(:,:) = complex(aa2, bb2)*1;
        % matrixComplex=matrixComplex1-matrixComplex2;
%No Phantom Calibration
        matrix2 = load('_Bistatic_Files/Practical_Fixed_NoPhan_16Positions_Bistatic.txt');
        aa2 = matrix2(:, 1:2:end);
```

```
        bb2 = - matrix2(:, 2:2:end);
        matrixComplex2(:,:) = complex(aa2, bb2)*1;
        matrixComplex=matrixComplex1-matrixComplex2;
%-------------------------------------------------------------------------------------------------------------------------
%Phantom / Test Setup
        er1=1;
        ur1=1;
        sigma1=0.2;
        raggio0=0.055;
        delta_phi=45*pi/180;   % phi step
        phi_oss=[0:delta_phi:2*pi-delta_phi] ;
        rho_oss=raggio0*ones(1,length(phi_oss))*1.0;
% grid where we want to reconstruct the  internal field
        delta_phi_reconstr=pi/90;
        delta_rho_reconstr=0.0005*4;
        [phi_oss_reconstr,rho_oss_reconstr]= meshgrid(0:delta_phi_reconstr:2*pi, 0:delta_rho_reconstr:rho_oss);
        NP_rho=size(phi_oss_reconstr,1)
        NP_phi=size(phi_oss_reconstr,2)
        % free-space
```

```
        u0=4*pi*10^(-7);
        e0=1/(36*pi)*10^-9;
        Z0=120*pi;
        c0=300000000;
% frequency
        f_min=1.8*10^9
        f_max=2.5*10^9
        df_new=7*10^5;  % frequency step
        new_ff=[f_min:df_new:f_max]';
        NF=length(new_ff);
        BB=df_new*NF;
        phi_note_MULTISOURCE=[0:45:359]./180*pi  % phi coordinate of line source
        [X_reconstr,Y_reconstr] = pol2cart(phi_oss_reconstr,rho_oss_reconstr);
        simulated_reconstr_HuygensG_diff_OLD=zeros(NP_rho,NP_phi,length(new_ff)*5);  % NOTE *5 derives from the use of 5 sections
        simulated_reconstr_HuygensG_diff_NEW=zeros(NP_rho,NP_phi,length(new_ff)*5);  % NOTE *5 derives from the use of 5 sections
        newindex=1
        COEFF_NORM=1/(2*pi*raggio0)*df_new/(df_new*NF)*1/length(phi_note_MULTISOURCE);
%-------------------------------------------------------------------------------------------------------------------------------
mmm=mean(matrixComplex,1).*1;
```

```
for multisource_index=1:8  % modify to 8 and accordingly for 8rx array
        phi_note=phi_note_MULTISOURCE(multisource_index)
        phi_oss=-[phi_note:delta_phi:2*pi+phi_note]
        for i=1:5:1001
                f=new_ff(i);
                e1=er1*e0*(1-j*sigma1/(2*pi*f*er1*e0));
                u1=ur1*u0;
                k1=sqrt((2*pi*f)^2*u1*e1);
                Z1=sqrt(u1/e1);
                lambda1=2*pi./real(k1);
                pen_depth=-1./imag(k1)
                for np=1:7  %np=1:80 %np=[1:20,60:80]
                 %(k1)
                        simulated_reconstr_HuygensG_diff_OLD(:,:,newindex)=simulated_reconstr_HuygensG_diff_OLD(:,:,newindex)+COEFF_NORM*delta_p
                        hi*raggio0*(k1)/(2*pi*f*e1)*(matrixComplex(np+(multisource_index-1)*7,i)-                    mmm(1,i))*exp(-
                        1i*(k1)*sqrt(rho_oss_reconstr.^2+rho_oss(np).^2-2*rho_oss_reconstr.*rho_oss(np).*cos(phi_oss_reconstr-phi_oss(np)))).*exp(-
                        imag(k1)*sqrt(rho_oss(np).^2-rho_oss_reconstr.^2));


                 %real(k1)
```

```
                simulated_reconstr_HuygensG_diff_NEW(:,:,newindex)=simulated_reconstr_HuygensG_diff_NEW(:,:,newindex)+COEFF_NORM*delta_
                phi*raggio0*real(k1)/(2*pi*f*real(e1))*(matrixComplex(np+(multisource_index-1)*7,i)-                mmm(1,i))*exp(-
                1i*real(k1)*sqrt(rho_oss_reconstr.^2+rho_oss(np).^2-2*rho_oss_reconstr.*rho_oss(np).*cos(phi_oss_reconstr-phi_oss(np)))).*exp(-
                imag(k1)*sqrt(rho_oss(np).^2-rho_oss_reconstr.^2));
            end
            newindex=newindex+1;
            i
        end
end
MAG_uwb_scatt_incoh_reconstr_diff_OLD=zeros(NP_rho,NP_phi);
MAG_uwb_scatt_incoh_reconstr_diff_NEW=zeros(NP_rho,NP_phi);
new_ff
MAG_uwb_scatt_incoh_reconstr_diff=zeros(NP_rho,NP_phi);
new_ff
for i=1:length(new_ff)*5
    MAG_uwb_scatt_incoh_reconstr_diff_OLD(:,:)=MAG_uwb_scatt_incoh_reconstr_diff_OLD(:,:)+abs(simulated_reconstr_HuygensG_diff_OLD(:,:,i)).^1;
    MAG_uwb_scatt_incoh_reconstr_diff_NEW(:,:)=MAG_uwb_scatt_incoh_reconstr_diff_NEW(:,:)+abs(simulated_reconstr_HuygensG_diff_NEW(:,:,i)).^1;
end
totalIntesita_MAG=0;
for m=1:size(rho_oss_reconstr,1)
```

```
        for n=1:size(phi_oss_reconstr,2)
            totalIntesita_MAG=totalIntesita_MAG+MAG_uwb_scatt_incoh_reconstr_diff_OLD(m,n)*delta_phi_reconstr*delta_rho_reconstr*rho_oss_reconstr
            (m,n);
        end
end
mediaIntesita_MAG=totalIntesita_MAG/(pi*raggio0^2);
%-------------------------------------------------------------------------------------------------------------------------
figure
contourf(X_reconstr,Y_reconstr,(MAG_uwb_scatt_incoh_reconstr_diff_OLD).^1,50), colormap(jet), caxis([____])
xlabel('x')
ylabel('y')
title('Fixed System - 8 Position Practical', 'Bistatic - Position 1 Lesion')
axis square
colorbar
grid
```